



저작자표시-비영리-변경금지 2.0 대한민국

이용자는 아래의 조건을 따르는 경우에 한하여 자유롭게

- 이 저작물을 복제, 배포, 전송, 전시, 공연 및 방송할 수 있습니다.

다음과 같은 조건을 따라야 합니다:



저작자표시. 귀하는 원저작자를 표시하여야 합니다.



비영리. 귀하는 이 저작물을 영리 목적으로 이용할 수 없습니다.



변경금지. 귀하는 이 저작물을 개작, 변형 또는 가공할 수 없습니다.

- 귀하는, 이 저작물의 재이용이나 배포의 경우, 이 저작물에 적용된 이용허락조건을 명확하게 나타내어야 합니다.
- 저작권자로부터 별도의 허가를 받으면 이러한 조건들은 적용되지 않습니다.

저작권법에 따른 이용자의 권리는 위의 내용에 의하여 영향을 받지 않습니다.

이것은 [이용허락규약\(Legal Code\)](#)을 이해하기 쉽게 요약한 것입니다.

[Disclaimer](#)

A THESIS FOR THE DEGREE OF DOCTOR OF PHILOSOPHY

**Synthesis, Characterizations and Implementation of
Functional Nanostructured Materials and Composites for
Point-of-Care Testing Devices**

Muhsin Ali

Department of Mechatronics Engineering

GRADUATE SCHOOL

JEJU NATIONAL UNIVERSITY

2021. 02

Synthesis, Characterizations and Implementation of Functional Nanostructured Materials and Composites for Point-of-Care Testing Devices

Muhsin Ali

(Supervised by Professor Kyung Hyun Choi)

A thesis submitted in partial fulfillment of the requirement for the degree of Doctor of Philosophy

2021. 02

The thesis has been examined and approved

Thesis director, Joung Hwan Lim, Department of Mechatronics Engineering

Kyung Hyun Choi, department of Mechatronics Engineering

Chul Ung Kang, Department of Mechatronics Engineering

Chang Nam Kang, Departments of Mechanical Engineering

Myung Taek Hyun, Departments of Mechanical Engineering

Date:

Department of Mechatronics Engineering

GRADUATE SCHOOL

JEJU NATIONAL UNIVERSITY

REPUBLIC OF KOREA

**DEDICATED TO MY BELOVED PARENTS AND SIBLINGS,
ESPECIALLY TO MY MOTHER WHOM SUPPORT MADE ME ABLE
TO ACCOMPLISH THIS GOAL, AND TO MY DEAR HOMELAND
“PAKISTAN”.**



Acknowledgment

Alhamdulillah, and off course all praises to the divine power (ALLAH) who has been blessing me with this honor. I would like to mention my all-time favorite quote “Thanks for everything ALLAH even the trails that has made me closer to you”. Indeed, life is the name of rise and fall and the true belief in ALLAH reflects when you are feeling low. I pray and seeks ALLAH’s guidance to put me on the right path and help me in making my future life easy and achieve my future accomplishments.

I will be always thankful to my supervisor Prof. Dr. Kyung Hyung Choi for his management, skilled supervision; support and confidence that has been made me able to achieve this goal. I have learned a lot throughout my stay at AMM (Advanced Micro Mechatronics) lab that have increased my knowledge up to the date. I also wish him good health and happiness for the rest of his life.

I would like to express my heartfelt gratitude to my affectionate parents as they have been supporting me through this long journey. I would specially appreciate the assistance of my mother as she stood beside when I was in dire need. I found her as the best supporter, mentor, helper, devoted, role model and a friend of mine. I have been learning a lot from her and practicing that how to overcome when you are in bad circumstances. It was her encouragement and have faith in me that kept me going on this far and achieve my goal. I am indebted to my beloved siblings, and grandmother who have been participating through their prayers that has made me able to overcome the hard time in this journey and off course, my lovely nieces and nephews who always made me smile. I am especially thankful to my younger brother Ahmad Ali who has been fulfilling all the responsibilities on my behalf back in Pakistan. I’m furthermore thankful to my cousins, such a beautiful soul Ali Askar (Late) for his support, may Allah give him highest rank in Jannah and Dr. Adnan Ali Gohar for his constant support and motivation that he has been doing and still looking forward for his honest suggestions and guidance. I would like to thanks one of my best friends Arif Mir, who has been remaining in constant touch and encouraged me through this long four years journey.

I would like to pay my gratitude to all AMM colleagues including Asad, Abdul, Arun Asif, Faiza Jabbar, Afaque Manzoor Soomro, and Umer Farooqi, Kyung Hwan, Jae wook, Kinam, Sung Hyuk, Yung Su, Dr. Soo Hwan Kim, who have been made my stay easy and always being honored. I am always thankful to my seniors including Dr. Ghayas Uddin Siddiqui, Dr. Memoon Sajid, Dr. Shahid Aziz and Dr. Imran Shah, Dr. Israr, Dr. Muqheet, Dr. Fayyaz for their support and guidance. I am pleased to my friends including Asif, Umair, Zeeshan, Uzair, Raza Waseem, Shaenawar, Saqib, Adeel, Imran and Dr. Irshad, Dr. Shabir, Dr. Sehrish, Dr. Wafa, Sana Ullah, Faisal during my stay at Jeju. All these wonderful individuals have impact of worthy memories in my life that will be cherished me throughout my life. I have certainly missed many names who have tiny contributions in this accomplishment; I am truly indebted to all of them.

I would take this occasion to thank the wonderful people of Korea and above all Jeju folks who have always been nice to me and other foreign person. I would say Jeju is awesome and has given me a lot of unforgettable memories.

I am very much thankful to ALLAH for the continuous blessings he has been showering.

Muhsin Ali

Contents

List of figures.....	vi
List of tables.....	ix
1. Introduction.....	1
1.1. Biomarkers.....	1
1.2. Nanostructured materials.....	1
1.2.1. Quantum dots.....	2
1.2.2. Nanowires.....	2
1.2.3. Nanocomposites.....	2
1.2.4. Nanocubes.....	3
1.3. Biosensors.....	3
1.3.1. Electrochemical biosensors.....	4
1.3.2. Optical biosensors.....	4
1.3.3. Mass based biosensors.....	5
1.4. POCT (Point-of-care) devices.....	5
2. Chapter 2. Electrochemical biosensors.....	6
2.1. Electrochemical based detection of Uric Acid through ZnO QDs guiding layer.....	6
2.1.1. Background and overview.....	6
2.1.2. ZnO quantum Dots synthesis.....	8
2.1.3. Screen printed biosensor fabrication.....	8
2.1.4. Characterizations of ZnO QDs.....	10
2.1.5. Results.....	12
2.1.6. Application: detection of UA.....	16
2.2. Electrochemical based detection of lactate through novel composite (MWCNTs/PEDOT:PSS).....	17
2.2.1. Background.....	17
2.2.2. Nanocomposite synthesis and electrode functionalization.....	19
2.2.3. Composite characterizations.....	21
2.2.4. Optimization of analytical parameters.....	25
2.2.5. Analytical performance of the sensor.....	26

2.2.6.	Application: lactate detection in cancer cells media	29
3.	Chapter 3. Fluorescent based biosensor.....	32
3.1.	Upconverting nanoparticles based vaspin biosensors strip overview.....	32
3.1.1.	Nanoparticles (NayF ₄ : Yb, Er) size reduction.....	33
3.1.2.	Functional group exchange Mal-PEG-COOH.....	34
3.1.3.	Bioconjugation of aptamers.....	34
3.1.4.	Lateral flow strip	36
3.1.5.	Sample assay	37
3.1.6.	Characterizations of conjugated nanoparticles	39
3.1.7.	Vaspin detection using LFSA strip in buffer samples	43
3.1.8.	Application: Vaspin detection in serum samples.....	45
3.2.	Fluorescent dye based detection of Reactive oxygen Species (ROS) in microfluidic chip	46
3.2.1.	Background	47
3.2.2.	Optimization of concentration and mechanism of dye interaction with cells	50
3.2.3.	Microfluidic chip	51
3.2.4.	Cell culture on a microfluidic chip.....	51
3.2.5.	In-house built fluorescence microscope	53
3.2.6.	Image processing	54
3.2.7.	Results and Discussion	54
3.2.8.	Application: Real time monitoring and evaluation of ROS in breast cancer cells line (MCF-7) 63	
4.	Chapter 4. Colorimetric based biosensor	67
4.1.	Colorimetric based Uric acid detection (non-enzymatic)	67
4.2.	Citrate capped Pt nanoparticles (PtNPs) synthesis.....	69
4.3.	Non-enzymatic based UA detection	70
4.4.	Design of POCT device	71
4.5.	Characterizations of PtNPs.....	73
4.6.	Colorimetric sensing mechanism	75
4.7.	Theoretical calculations	78
4.8.	Detection of Uric Acid on cellulose strip.....	79

4.9. Application: Detection of UA in urine samples.....	82
5. Conclusion and future work.....	85
References	89

List of figures

Figure 2-1: This figure illustrates the printing process (Flow diagram) with (a) cross-sectional representation of the three electrodes printed on PI substrate through screen-printing along with (b) selective pattern and functionalization of the working electrode with ZnO QDs and uricase respectively	9
Figure 2-2: Characterizations (a) UV–vis spectra of the ZnO QDs and (b) Raman shift of working electrode after the pattern of ZnO QDs.....	11
Figure 2-3: FESEM images of biosensor (a) 5 μm magnification of counter electrode (b) 5 μm magnification of working electrode, carbon electrode with ZnO QDs (c) 1 μm magnification of reference electrode (Ag/AgCl). (d) TEM images of ZnO QDs.....	12
Figure 2-4: (a) Reaction mechanism of UA in the presence of the uricase and (b) initial voltammogram of the sensor in the presence and absence of analyte (UA).....	13
Figure 2-5: Cyclic Voltammograms and typical response of Chronoamperometry of the printed sensor for UA (a) UA acid in NaOH solution from 1 mM up to 10 mM concentrations and (b) a calibration curve for the response of current vs UA concentration of the printed sensor at 0.6 V (c) chronoamperometric response of the sensor with a subsequent increase in the concentration of UA keeping the potential at 0.6 V (d) calibration curve for the response of printed sensor with successive addition of 1 mM of UA concentration	15
Figure 2-6: (a) Chemical structure of PEDOT:PSS, (b) Schematic structure of PSS doped PEDOT, and (c) Schematic representation of MWCNT/PEDOT:PSS composite.....	19
Figure 2-7: Depiction of an electrochemical sensor for lactate detection, modification of WE by drop-casting MWCNTs, and PEDOT: PSS composite, followed by lactate oxidase and BSA along with the mechanism of the reaction	21
Figure 2-8: Raman spectra of (a) the composite MWCNTs and PEDOT: PSS, (b) PEDOT: PSS, (c) and MWCNTs	22
Figure 2-9: Typical FESEM images. (a) MWCNTs and PEDOT: PSS ink, (b) Observed for MWCNTs under the resolution of 500 nm, (c) PEDOT: PSS under the resolution of 200 nm, (d) composite synthesized under the magnification of 1 μm	23
Figure 2-10: Energy-dispersive X-ray spectroscopy (EDX) and elemental mapping of (a) MWCNTs, (b) PEDOT:PSS, and (c) composite of MWCNTs and PEDOT: PSS.....	24
Figure 2-11: AFM images of the surface of unmodified carbon electrode and PEDOT:PSS/MWCNTs composite modified surface along with the contact angle images	25
Figure 2-12 Optimization of different sensing parameters (a) Temperature, (b) pH, (c) Applied potential, and (d) BSA concentration with 1 mM lactate. Mean ± standard deviation (SD), n = 3	26
Figure 2-13: (a) Modification of WE (b) CV response of the sensor comprising blank, unmodified, and modified WE with PEDOT:PSS/MWCNTs in 10 mM K ₄ [Fe(CN) ₆] (c) stability test of the sensor, after 5 cycles in the presence of 1 mM lactate (scan rate = 250 mV/sec) (d) conversion of lactate into pyruvate	

on the surface of WE along with the inset image of the three electrodes electrochemical setup used..... 26

Figure 2-14: (a) Cyclic Voltammograms of the sensor for the detection of lactate ranges from 0.6 mM to 1.0 mM **(b)** calibration curve of the sensor for different lactate concentrations in the linear range (0.6-1.0 mM) **(c)** Chronoamperometric response of the sensor in various concentration of lactate, ranges from 0.1 to 10 mM along with **(d)** Calibration curve under the same experimental conditions, mean \pm standard deviation (SD), n = 3..... 28

Figure 2-15: Pre seeding inverted microscopic images of MCF-7 cells at the resolution of 4, 10 and 20X 30

Figure 2-16: (a) Reproducibility measurements (n = 3), PEDOT: PSS and MWCNTs of four modified screen-printed electrodes prepared under the same protocol for the detection of 1 mM lactate (pH 7.0), **(b)** selectivity of the biosensor, data presented as mean \pm SD, (n = 3) 31

Figure 3-1: Ligand Exchange and bioconjugation: Schematic of the phase of oleic acid-capped upconverting nanoparticle, Functionalization of the surface of UCNP with maleimide group by ligand exchange method and subsequently conjugation with thiol aptamer.... **Error! Bookmark not defined.**

Figure 3-2: Schematic illustration of the configuration of the UCNP based lateral flow vaspin sensor and principle of qualitative detection of vaspin on the fluorescent upconverting nanoparticles based lateral flow biosensor. 37

Figure 3-3: Steps of strip fabrication and evaluation: Typical diagram for calculating RGB of test line when excited in NIR (980 nm) for recording the concentration of Vaspin using high resolution camera 38

Figure 3-4: (a) Photoluminescence spectroscopy of the colloidal solution of the UCNP under excitation wavelength of 980 nm **(b)** Fluorescence of nanoparticles colloidal solution (5 mg ml⁻¹) **(c)** TEM images of NaYF₄ (Yb: Er) nanoparticles **(d)** Dynamic light scattering of the colloidal UCNP with an average hydrodynamic diameter of around 100 nm 40

Figure 3-5: X ray photoelectron spectroscopy (XPS) **(a)** Survey, **(b)** Na 1s, **(c)** Y 3d, **(d)** F 1s, **(e)** Yb 4d and **(f)** Er 4d. 40

Figure 3-6: Raman spectra of UCNP **(a)** Spectra of 100 nm unmodified upconverting nanoparticles NaYF₄ (Yb: Er) **(b)** UCNP@Mal-PEG-COOH modified particles showing the characteristics stretching of ether group (R-O-R) between 800 and 920 cm⁻¹ **(c)** Complete Raman spectrum of the functionalized particles..... 42

Figure 3-7 FTIR spectrum of the aptamer-UCNP conjugate: different peak positions confirming the presence of upconverting nanoparticles (NaYF₄: Yb, Er) and oligomers (Aptamer)..... 43

Figure 3-8: Analysis of LFSA **(a)** Images of the sensor with different concentrations of target Vaspin under the optimal experimental conditions and **(b)** Calibration curve of test line intensity versus Vaspin concentration. Error bars represent standard deviation, n = 3. 45

Figure 3-9: Detection of Vaspin spiked in human serum (pH = 7.0) using UC based LFSA, different concentration of vaspin were diluted in serum samples and observed under excitation of 980 nm laser. 46

Figure 3-10: Schematic illustration of the generally accepted mechanism of interaction of DCFDA with ROS in cells 51

Figure 3-11: Microfluidic chip. **(a)** Top and bottom glass **(b)** Full chip configuration; cell culture on bottom glass, schematic view of cross-section **(c)** assembled chip with microscope **(d)** 3D printed microscope and assembled microfluidic chip in a 3D printed chip holder (original images). 51

Figure 3-12: MCF-7 cells on-chip for the real-time detection of intracellular reactive oxygen species, a complete setup of the platform including microfluidic chip, media reservoir, peristaltic pump, bubble remover, and fluorescence microscope 53

Figure 3-13: Fluorescence microscopy of MCF-7 cells (1.5×10^5). Cells that were cultured and exposed to 700 μ l of 0, 5, 15, 25 and 50 μ M 2',7'- dichlorofluorescein diacetate (DCFDA) along with background DCFDA fluorescence, also without DCFDA (data presented as mean \pm standard deviation (SD), $n = 3$). Scale bar is 200 μ m. 56

Figure 3-14 Evaluation of DCFDA and H₂O₂ on cells viability. Cells were loaded with 0, 5, 15, 25 and 50 μ M DCFDA and then washed and later on exposed to H₂O₂ (0, 5, 7.5 and 10 μ M) for 24 h. Fluorescence microscopy was used to observe the cells viability and compared with the standard cell number obtained from luna cell counter. Means \pm SD of 3 independent experiment have been shown. Calibration curve of H₂O₂ concentration vs. fluorescence under the same experimental conditions, mean \pm standard deviation (SD), $n = 3$ 57

Figure 3-15: Pre seeding inverted microscopic images at different resolution of MCF-7 cells and after seeding them on-chip at the resolution of 4, 10 and 20X 58

Figure 3-16: Microfluidic chip evaluation **(a)** microfluidic chip showing the cell-cultured area through the custom-built seeding kit, image was taken by inverted microscope **(b)** showing the cell culture area on ECM coated bottom glass through inverted microscope, scale bar is 100 μ m mold **(c, d)** under the fluorescence microscope incubated with and without DCFDA, Scale bar is 100 μ m **(e)** Velocity profile and **(f)** Pressure contour of the fluid passing through the microfluidic channel under the flow rate of 60 μ l/min..... 59

Figure 3-17: MCF-7 Cells viability assay. Cells were exposed to 50 μ M DCFDA and then remove it after 45 min and followed by the circulation of RPMI for 24 h. Live/Dead assay was performed on the same MCF-7 cells and compared with the control obtained from the Luna cell counter as shown above. Data were subjected to ImageJ software showing the viability of the cells up to 75% after completion of the experiment on a microfluidic chip. Scale bar is 200 μ m 60

Figure 3-18: Fluorescence microscope **(a)** Basic Fluorescence Microscopy working Setup employed in commercial microscopes **(b)** 3D CAD design model of our portable digital fluorescence type microscope **(c)** exploded view has been shown **(d)** schematic of the 3D printed microscope mold... 61

Figure 3-19: Actual platform image of the experimental setup for the online monitoring of ROS in breast cancer cell line MCF-7 63

Figure 3-20: Platform images and Multi-head 3D printing specifications..... 63

Figure 3-21: Real-time fluorescence images of the MCF-7 cells treated with 2',7'-dichlorofluorescein diacetate (DCFDA) taken through the fluorescence microscope using Toup view software according to the following schedule: control, 3, 6, 9, 12, 15, 18, and 21 h. Scale bar is 100 μ m..... 64

Figure 3-22 (a) A user-interactive Graphical User Interface based application **(b)** Histogram of green content present in the stills along with the waveform graph and green intensity of each image **(c)** time vs. green fluorescence obtained from the green wave through LABVIEW (data presented as mean \pm standard deviation (SD), $n=3$) 65

Figure 3-23: AA transfection in MCF-7 cells. **(a)** ROS level in terms of DCF fluorescent intensity (control, 10 μ M H₂O₂ introduction and 100 μ M Ascorbic acid introduction) after 24 hr **(b)** Intracellular DCFDA fluorescent intensity was visualized by confocal microscopy **(c, d)** Intracellular DCFDA fluorescent intensity after cells treated with 100 μ M and 50 μ M ascorbic acid over time (0, 12, 24) hr and were visualized by confocal microscopy..... 66

Figure 4-1: Illustration of the detection of UA using Pt NPs (a) Cellulose strip treatment protocol and mechanism of the response to UA introduction. (b) Color variation upon the introduction of different UA concentration.....	71
Figure 4-2: (a) Schematics of the portable POCT unit (b) Android based application for POCT test and POCT device images (front, side and top view)	72
Figure 4-3: (a) UV-vis spectra of PtNPs colloid solution (b) TEM images of as prepared citrate capped PtNPs with the inset image of histogram of synthesized PtNPs (c) FESEM image of cellulose substrate (d) EDS elemental image of PtNPs dispersed on the substrate.....	74
Figure 4-4: XRD pattern of as synthesized Pt nanoparticles by the reduction method	75
Figure 4-5: UV-Vis absorption of (a) TMB + PtNPs + H ₂ O ₂ (b) TMB + PtNPs + H ₂ O ₂ + UA (c) TMB + H ₂ O ₂ + UA (d) TMB + H ₂ O ₂ and (e) TMB + UA, and (f) TMB + PtNPs + H ₂ O ₂ + UA along with the corresponding photographs.....	76
Figure 4-6: Optimization of different parameters for reaction conditions (a) effect of Pt NPs concentration (b) TMB concentration (c) H ₂ O ₂ concentration (d) pH.....	78
Figure 4-7: (a) Velocity contour along with the arrow surface (b) Strip color range under the observation of various concentration of uric acid solution ranging from 1 to 8 mM.	79
Figure 4-8: (a) Response curve for UA detection (cellulose strips) vs intensity difference in the range from 0 to 8 mM (n = 4) (b) Images of varying concentration of UA on paper from 0 mM to 8 mM, respectively.	81
Figure 4-9: (a) Reproducibility measurement (n=4) sensor response to uric acid and detection by the developed colorimetric setup (b) Selectivity response of the developed assay to various interferences and UA.....	84

List of tables

Table 1. Comparison of the proposed three electrodes based uric acid biosensor with the other reported different structures of ZnO electrode for uric acid.	15
Table 2. Determination of UA levels in urine samples using the ZnO QDs based SPE sensor.....	17
Table 3. Analytical properties of lactate biosensors found in the literature. Error! Bookmark not defined.	
Table 4. Displays the results obtained from the proposed lactate biosensor and the colorimetric assay kit	31
Table 5. DNA oligonucleotides (aptamers) used in this study are provided	35
Table 6. Recovery results of Vaspin detection in serum (n = 3).	46
Table 7. Microscope specifications.....	53
Table 8. Comparison of the developed PtNPs based detection (colorimetric stimulated) with the other reported uric acid analysis.....	82
Table 9. Determination of uric acid in urine samples using the PtNPs based colorimetric sensor (n=3).....	84

Abstract

The emerging field of nanotechnology owes the capability to develop highly functional and novel nanostructured materials (NSMs), which have been addressing challenging applications due to its abundant strategic properties. NSMs have gained notability in diverse fields from the last two decades due to their tunable and unique physical, chemical, and biological properties. In the field of biosensors, NSMs have been providing the desirable properties by virtue of their significance in detection and analysis methods. This research work focuses on the synthesis, bioconjugation, functionalization, and characterization of NSMs and the development of high-performance biosensor devices targeting point-of-care-devices for the detection of analytes (Uric acid, Lactate, Vaspin, and Reactive oxygen species). In this thesis, we are focusing on the synthesis of Zero dimensional (0D) nanoparticles such as ZnO Quantum dots (ZnO QDs), Platinum nanoparticles (PtNPs) and upconverting nanoparticles (UCNPs) conjugation, one-dimensional (1D), nanotubes (multiwalled carbon-based) and two-dimensional (2D), multiwalled carbon nanotubes/poly (3,4-ethylene-dioxythiophene) poly(styrene sulfonate) (MWCNTs/PEDOT:PSS) composite. Moreover, biofunctionalization of UCNPs and bioconjugation with aptamers has been carried out. The characterization of the developed nanomaterials has been carried out using HR-TEM, FE-SEM, AFM, XRD, Raman, FTIR, EDX, and UV/VIS spectroscopy. These tailored nanostructured materials are implemented in the fabrication of electrochemical and optical-based biosensor devices for the detection of the requisite metabolites/biomarkers. These nanostructured materials have provided a steady platform for the immobilization of bioreceptors with biocompatibility, electrocatalytic properties along with high sensitivity, an improved range of detection (ROD), and detection limit (LOD). In brief, the implementation of NSMs has shown excellent performance in biosensing.

Introduction

1.1. Biomarkers

According to Hulka¹, biomarkers (biological markers) are “cellular, biochemical or molecular variations that are calculable in biological fluids such as CSF, blood, urine”. Detection of biomarkers in biological fluids, support in understanding the cause, prediction, diagnosis, curing, progression, regression, or disease treatment resultant². Scientists, medical doctors, and physicians have been considered a wide range of biomarkers, to diagnose, predict, and study human diseases. The application of biomarkers in a variety of diseases such as cancer, infections, genetic disorders, and immune are well known^{2,3}, and the detection of biomarkers is a prevailing health tool for premature diagnosis and dealing of diseases⁴. In this thesis, we have been detected Uric acid, Lactate, reactive oxygen species, and Vaspin.

1.2. Nanostructured materials

A nanometer (nm) is an International System of Unit (SI), which equals to 10^{-9} m in length. Principally, Nanostructured materials (NSMs) are having no less than one dimension that lies between 1-100 nm⁵. Nanoparticles (NPs) and nanostructured materials are showing expansions in the biosensors application domain due to their tunable physicochemical characteristics such as catalytic activity, electrical properties, high conductivity, biocompatibility, and enhanced performance over their bulk-sized equivalents⁶. NSMs provides a stimulating tool in the linking of biomolecules with integrated circuit technology. NSMs are classified under the following four main broad headings: Carbon-based nanomaterial, Inorganic, Organic, and composite based nanomaterials. Furthermore, based on their dimensions, NSMs were classified by Pokropivny and Skorokhod in 2007 including zero-dimensional (0D), one-dimensional (1D), two dimensional (2D), and three dimensional (3D)⁷. In the recent past, NSMs have been playing a significant role in the field of diagnostic devices in terms of sensitivity,

analysis methods, signal intensities, and highly adaptive surface chemistries⁸, and a variety of nanoparticles have been shown drastic improvement in the diagnostic tools⁹.

1.2.1. Quantum dots

Quantum dots (QDs) and nanoparticles are identified as 0D nanoparticles due to their confined electrons movement. QDs are semiconductor nanoparticles ranging from 2-10 nm size in scale and owing distinctive optical and electronic properties leading to those of larger nanoparticles because of their quantum level effects^{10, 11}. QDs are also known as artificial atoms and their properties are determined by size, shape, and composition. QDS has been explored in the development of biosensors for the highly sensitive detection of biomarkers^{12, 13}, furthermore, implemented in solar cells, photodetectors, lasers, and light-emitting diodes (LEDs). In our study, we have synthesized and used ZnO QDs in the development of electrochemical sensors and PtNPs in the colorimetric sensor.

1.2.2. Nanowires

Nanowires are 1D materials in which the electrons are allowed to move only in one direction. 1D materials correspond to fibers, whiskers, nanorods, nanotubes. They have been found from several metallic materials, semiconductors, and oxides, etc. They have attracted remarkable consideration and are believed to play a vital role in the field of nanoscience, chemical, biological sensors, and in electronic devices due to their major consequences¹⁴⁻¹⁶. Yet, the most studied 1D material is carbon nanotubes (CNTs) since the 1990s¹⁷. In our study, we have been used multiwalled carbon nanotubes (MWCNTs) in electrochemical sensor development.

1.2.3. Nanocomposites

Nanocomposite are 2D multiphase nanostructured materials, which are having at least one facet in the nanometer scale. The other main types of 2D materials include films, plates, multilayers, or networks. Nanocomposites are either a combination of NPs with other nanoparticles, polymers and nanofibers, not limited to a combination of any kind of nanostructured materials. Polymer-based

nanocomposites materials are highly favorable interfacing channel between the biorecognition elements and transducer surface ¹⁸. Nanomaterials (Carbon nanotubes, CNTs) and Polymer-based nanocomposites have gained extensive recognition due to their remarkable up-gradation in properties such as; surface area to volume ratio, mechanical stability, avoiding of surface fouling, conductivity, and flexibility of the biosensors devices ^{19,20}. In-order to boost up the sensitivity of biosensors devices, the use of nanocomposites is highly a favorable approach. In this work, we have synthesized MWCNT/PEDOT: PSS composite as a guiding layer for the electrochemical detection of lactate.

1.2.4. Nanocubes

Nanocubes are the example of the three-dimensional (3D) nanostructured materials, which size is not confined to any nanometer range dimension, but all dimensions are in macroscale. Additionally, bulk powders, nanoparticles dispersion, a bunch of nanowires, and nanotubes clusters, as well as multi-nanolayers, are examples of 3D nanostructured materials. The integral excellent properties of nanomaterials including 1D, 2D, and 3D nanostructures have been considerably implemented for the fabrication of biosensors.

1.3. Biosensors

To detect biomarkers instead of their minute concentrations present in the sample; biosensors devices which are having the immense potential for the detection of analytes due to their inherent simplicity, cost-effective, rapid analysis, miniaturization, and easy to use. Biosensors are analytical devices, incorporating biorecognition elements (Enzymes, Antigens, cells, tissue, DNA, and aptamers) with a physiochemical detector ²¹⁻²³. The concentration of the target analyte is directly proportional to the signal generated by the biosensor device. According to the International Union of Pure and Applied Chemistry description, “a biosensor is a self-contained integrated device that is capable of providing specific quantitative or semi-quantitative analytical information using a biological recognition element (receptor) which is in direct spatial contact with a transducer element” ²⁴. The first-ever biosensor was

developed by Leland C. Clark in 1956 for oxygen detection and later on, in 1962, Clark and Champ Lyons invented the glucose biosensor based on the metal-oxide-semiconductor field-effect transistor (MOSFET) ²⁵. Biosensors are a great alternative to counterfeited the difficulties of miniaturizations, sensitivity, quantification, and selectivity associated with the conventional methods ^{26, 27}. Enzyme-based sensors propagated significant consideration for the detection and quantification of biomarkers (redox-based) owing to repeatability, reliable performance, and miniaturizations ^{28, 29}. The inherent properties of the NSMs boost up the response of biosensors, which improves the linearity, sensitivity, selectivity, stability, the limit of detection. Based on the method of transduction, biosensors can be categorized into the following: electrochemical, optical, and mass-based.

1.3.1. Electrochemical biosensors

In electrochemical biosensors, the biochemical events are being transformed through the transducer to electrical signals. In this category of biosensors, the bioreceptors are fixed to the electrode that plays solid support for immobilization and electrons transduction. The credit goes to the nanomaterials that possess a high surface area to volume ratio and synergic effects are enabled which improves the loading capacity and mass transport of reactants for attaining the best performance in terms of analytical sensitivity. Amperometric sensors have emerged as a compelling platform for chemical sensors and biosensors owing to their numerous advantages. Electrochemical biosensors are on the top list for POC testing due to onsite sample readings and quick analysis. In this thesis, we have developed two electrochemical-based biosensors for the detection of Uric acid and lactate based on nanomaterials modified electrodes.

1.3.2. Optical biosensors

In optical biosensors, the bioreceptors sensing elements are fixed with an optical transducer system. Optical sensors can be exploited for light absorption, reflectance, fluorescence, Raman scattering (RS), and refractive index (RI) changes on an optical transducer surface that is recognized to take place

owing to specific bimolecular events. In this thesis, we focused on developing colorimetric and fluorescence-based detection of biomolecules (uric acid and reactive oxygen species).

1.3.3. Mass-based biosensors

Mass-based biosensors come under the categories of surface acoustic wave (SAW) biosensors, microcantilever based biosensor (MCL), and quartz crystal microbalances (QCM). The substrates used in these biosensors are piezoelectric with an interdigitated transducer, which transformed the mechanical waves into an electrical signal.

1.4. POCT (Point-of-care) devices

To achieve the best performance, narrowed response time, unobtrusive use, user friendly, for a variety of biomarkers concentration detection and analyses; electrochemical (amperometric based) biosensors are in the topmost list headed for POC testing. Point-of-care (POC) testing devices are crucial in the health welfare programs attributable to detecting the disease biomarkers at the patient place ^{30, 31}. Depending on the POCT device, it fulfills the acronym “ASSURED” (affordable, sensitive, specific, user-friendly, robust, equipment-free, and deliverable to end) ³². POCT devices are the innovative technology and pave a strong route to recognize speedy results and onsite sample analysis instead of taking samples into laboratories³³⁻³⁵.

Chapter 2. Electrochemical biosensors

2.1. Electrochemical based detection of Uric Acid through ZnO QDs guiding layer

2.1.1. Background and overview

Electrochemical biosensors have the advantages of exhibiting good sensitivity, portable size, quick response, unobtrusive use, and having the feasibility to be used directly over a wide range of concentration³⁶. Amperometric sensors have emerged as a compelling platform for chemical sensors and biosensors owing to their numerous advantages. The two typically successful applications of electrochemical sensors are glucose sensor³⁷ and uric acid (UA) sensor. In recent years, the introduction of nanotechnology enhanced the field of biosensors by the virtue of its significance in detection, analysis methods, and clinical diagnostics^{8, 38}. Due to the unique physicochemical properties of nanomaterials, they provide desirable and incomparable characteristics for chemical and biological detection such as the high surface area to volume ratio, significant signal intensities, and high adaptive surface chemistries³⁹. Different types of nanomaterials such as carbon nanotubes, silica nanowires, magnetic nanoparticles, AuNPs, and most importantly quantum dots have been introduced providing high sensitivity in-vitro diagnostic (VID) systems for a variety of different biomarkers⁴⁰. Quantum dots are semiconductor particles ranging in a very small size range of only several nanometers, and their optical and electronic properties differ from those of larger particles of the same material due to quantum level effects. These properties play a vital role in nanoscience and nanotechnology. Quantum dots are also sometimes referred to as artificial atoms. Moreover, they show properties that are intermediate between those of bulk semiconductors and discrete molecules. The function of both shape and size affects the optoelectronic properties of QDs. Zinc oxide (ZnO) semiconducting nanomaterials are the most functional metal oxide semiconductors because of their exclusive

band gap (~ 3.37 eV), large excitation energy (~ 60 eV), and high electron mobility⁴¹. Based on their high electron mobility, ZnO nanostructures have been examined for multiple applications such as in the field of photonics and sensing. Numerous studies have been carried out using ZnO nanostructures for different types of sensors, like gas sensors⁴², biosensors⁴³, uric acid⁴⁴, and chemical sensors⁴⁵. Most importantly, ZnO nanostructured layers have been used in the biosensor. It facilitates the immobilization of various enzymes such as uricase, glucose oxidase for the detection of uric acid, and glucose. The reason for the ease of immobilization of various enzymes on the surface of ZnO QDs is partially due to the high isoelectric point (IEP) which is nearby 9.5⁴⁶. At a normal pH value of around 7.5 (physiologically), this high IEP provides positively charged surfaces. Enzymes having negatively charged surfaces such as acidic enzymes (Uricase) can be immobilized electrostatically. Uricase has low IEP so it can be electrostatically immobilized on the surface of the ZnO QDs layer, which provides good thermal stability (85°C) and high selectivity to uric acid. A thin film of ZnO and ZnO nanowires or nano-rods can also be used but QD's (2–4 nm) are known to provide very high effective surface area and excellent surface activity thereby enhance the charge transfer across the transducers and electrolyte interface⁴⁷. In this work, for the first time a simple and innovative technique for the fabrication of ZnO QDs modified SPE biosensor. Currently, it is recognized as a convenient and economical approach for the mass production of biosensors, and thus making them commercially available. An electrochemical sensor was fabricated through screen printing to selectively pattern the substrate with the three electrodes (i.e. working, counter and reference electrode) using carbon and silver inks. Afterwards, ZnO QDs were drop casted onto the carbon working electrode. As ZnO QDs have positive surface charge, electrostatic attraction occurs upon simple functionalization of uricase (low IEP) and QDs to assist specific binding. Thus, this electrochemical sensor provides an easy immobilization of uricase, demonstrated for the sensitive detection of UA. Normal concentration of UA (1.5–4.4 mmol/day, 250–750 mg/day) in the urine samples falls in the detection range of this sensor, which could be easily determined through ZnO QDs, based SPE sensor. It can be

detected with this sensor if the concentration of UA is increased due to an occurrence of a disease. Uric acid was used here as the biomarker analyte while other biomarkers could also be analyzed by using corresponding surface functionalization on the ZnO QDs guiding layer.

2.1.2. ZnO quantum Dots synthesis

To synthesize zinc oxide quantum dots (ZnO QDs) the precursor solution was prepared accordingly: ZAD ($\text{ZnAc}_2 \cdot 2\text{H}_2\text{O}$) (10 mmol) was mixed with 100 ml of anhydrous ethanol and process for being refluxed at 70°C for 4 h. Simultaneously, $\text{LiOH} \cdot \text{H}_2\text{O}$ concentration of 3 mM blended with 10 ml anhydrous ethanol and completely dissolved. In the last, this solution was strongly mixed with the precursor solution and allowed to react the solution became turbid, indicating ZnO QDs were formed. To acquire ZnO QDs precipitate the solution by adding 20 ml n-hexane and centrifuged for 10 min to get the precipitant. Subsequently, it was dissolved in ethanol and centrifuged to get the supernatant and dried to get powder of ZnO QDs. The obtained ZnO QDs were first rinsed with undiluted ethanol to expel the unreacted precursors. The powder was then dispersed in N-methyl-pyrrolidone (NMP) by using a bath sonicator and stored till use ⁴⁸.

2.1.3. Screen printed biosensor fabrication

Polyimide (PI) was used as a flexible substrate while the electrodes were printed on it using the screen-printing process as shown in Fig. 2-1. The sensor design consisted of three electrodes: an Ag/AgCl pseudo-reference electrode and two carbon electrodes acting as working and counter electrodes. Each electrode size was set as shown in Figure 2-1. The first step was the preparation of the mask for the electrode patterns that were cut into a mesh structure and was subsequently attached to the PI film. Carbon ink was then used to print the working electrode and counter electrode onto the surface. After-wards, Ag/AgCl reference electrode was separately printed. After printing carbon and Ag/AgCl electrodes, the sample was heated in the oven for 10 min at 50°C to allow the initial sintering of inks. Subsequently, the screen was detached and the patterns

were reheated for 60 min at 120°C for complete sintering. ZnO QDs selectively patterned the working electrode through drop-casting and uricase was immobilized on its surface. Electrical wires were attached and the photoresist was applied to the connection tracks leaving only the sensing area exposed to the test sample and confining the conductive connection paths. As a result, a window of 9 mm x 6 mm was left exposed for the test sample.

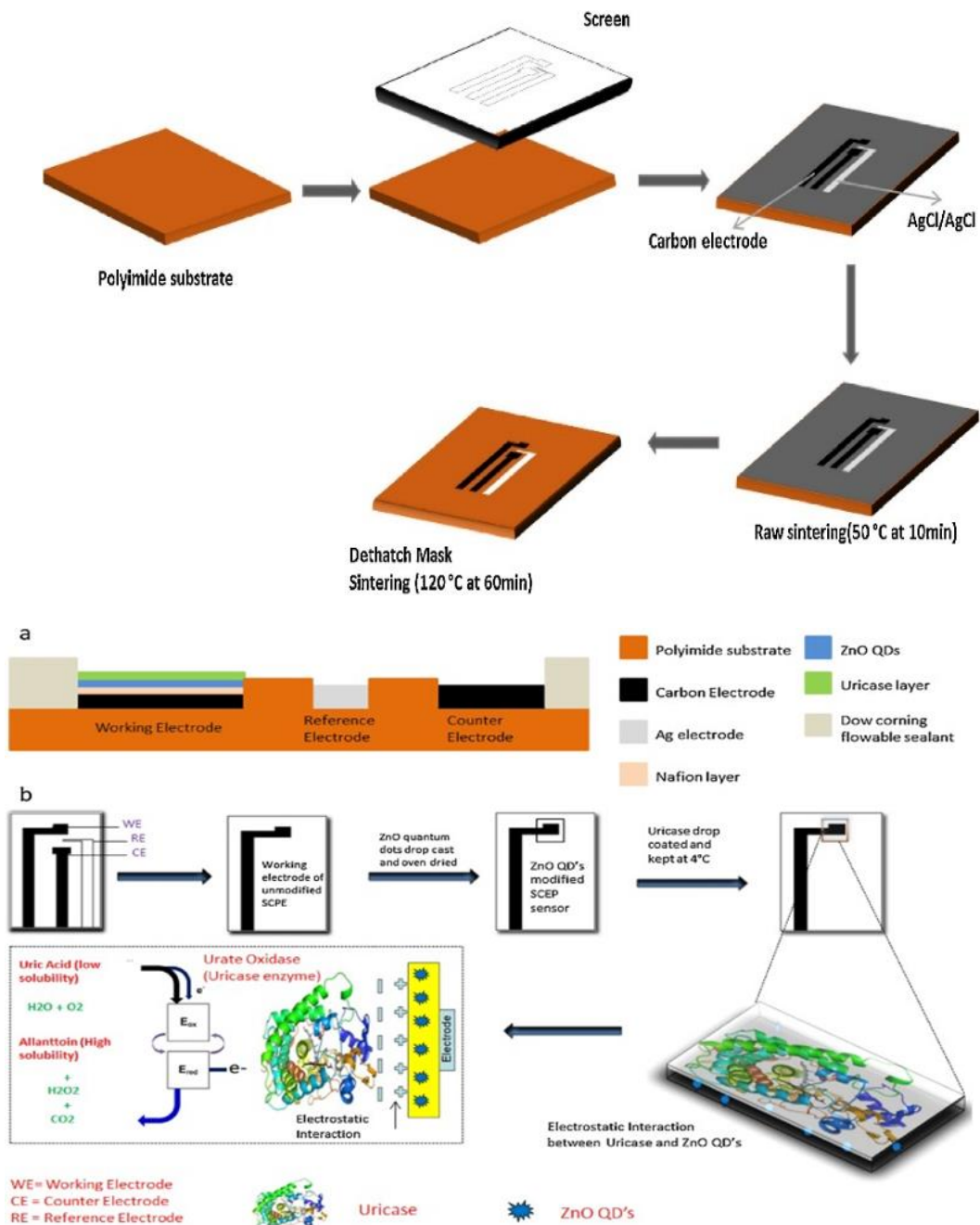


Figure 2-1: This figure illustrates the printing process (Flow diagram) with (a) cross-sectional representation of the three electrodes printed on PI substrate through screen-printing along with (b) selective pattern and functionalization of the working electrode with ZnO QDs and uricase respectively

2.1.4. Characterizations of ZnO QDs

The Ultraviolet-visible (UV-vis) spectroscopy was used to measure the specific wavelength of light absorbed by ZnO QDs. The specific wavelength (nm) of light indicates the range of QDs size [33]. Absorption peak was observed at 360 nm, which corresponds to 5–8 nm dot size and when exposed to UV radiation (365 nm) it manifested blue luminescence as shown in the inset image of Fig. 2-2(a). From the UV-vis data, the bandgap values for a direct bandgap semiconductor such as ZnO can be calculated by the Tauc plot, $(\text{abs} \times h\nu)^2$ vs $h\nu$ ⁴⁹ which is 3.48 eV for ZnO QDs. Raman scattering spectroscopy after dispensing of ZnO QDs to define the structural characteristics characterized by the working electrode of the screen-printed sensor. Fig. 2-2(b) shows the Raman spectrum of ZnO QDs on the screen-printed carbon electrode. A sharp peak at 445 cm^{-1} was obtained in the bulk of standard ZnO shown in the inset spectrum individually. It can be allocated as the frequency branch of the E_2 mode of ZnO crystal. The other peaks in the region $300\text{-}500 \text{ cm}^{-1}$ are emanated from $3E_2H - E_2L$ to the second-order spectrum emerging from zone-boundary phonon. Additionally, all the eminent peaks related to ZnO QDs were also found in the combined spectrum of the working electrode. The Raman shifts at 1340 cm^{-1} and 1585 cm^{-1} are actively described D and G band respectively, which corresponds to C–C stretching in graphitic materials and is common to all sp^2 carbon atoms. Sp^2 carbon materials manifest a strong peak in the range $2500\text{-}2800 \text{ cm}^{-1}$ in the Raman spectra and are called 2D (G^*)-band. Here is 2719 cm^{-1} which is a signature of GO. Thus, the presence of all these specified peaks indicates the uniform distribution of ZnO along with C- sp^2 atoms.

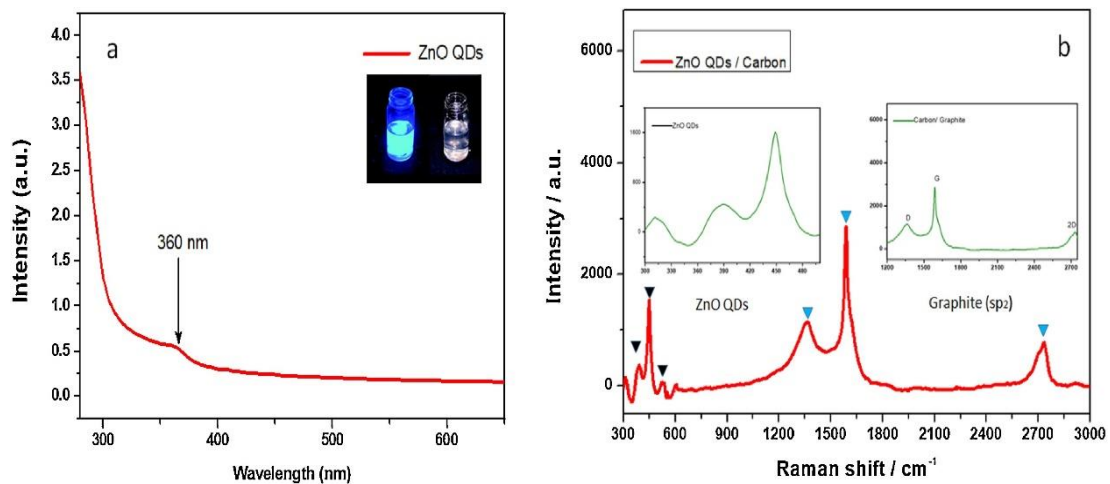


Figure 2-2: Characterizations **(a)** UV-vis spectra of the ZnO QDs and **(b)** Raman shift of working electrode after the pattern of ZnO QDs.

The morphologies of the three electrodes of the uric acid sensor have been characterized by FESEM as shown in Fig. 2-3. It can be seen from Fig. 3a that the surface of the counter electrode showed the porous structures representing graphene (Confirmed by Raman analysis as shown in the above figure having D, G, and 2D bands) which has an immense porous structure under the resolution of 5 μm . Fig. 2-3(b) is showing surface morphology after the decoration of GO by ZnO QDs and followed by uricase immobilization which is acting as a working electrode. The working electrode is also examined under the same resolution which is a bit hazy due to the presence of QDs and enzyme embedded in the porous structure of GO. As QDs are tiny sized particles, which cannot be located under this resolution, so ZnO QDs were analyzed by high-resolution Transmission electron microscopy as shown in Fig. 2-3(d), which reveals the average diameter of QDs 4–6 nm with well-resolved lattice fringes. Fig. 2-3(c) shows the surface of the bare reference electrode, which is, composed of almost homogeneous silver (Ag) nanoparticles under the resolution of 1 μm . Ag/AgCl is beneficial for the production of SPEs as a reference electrode with a reproducible response.

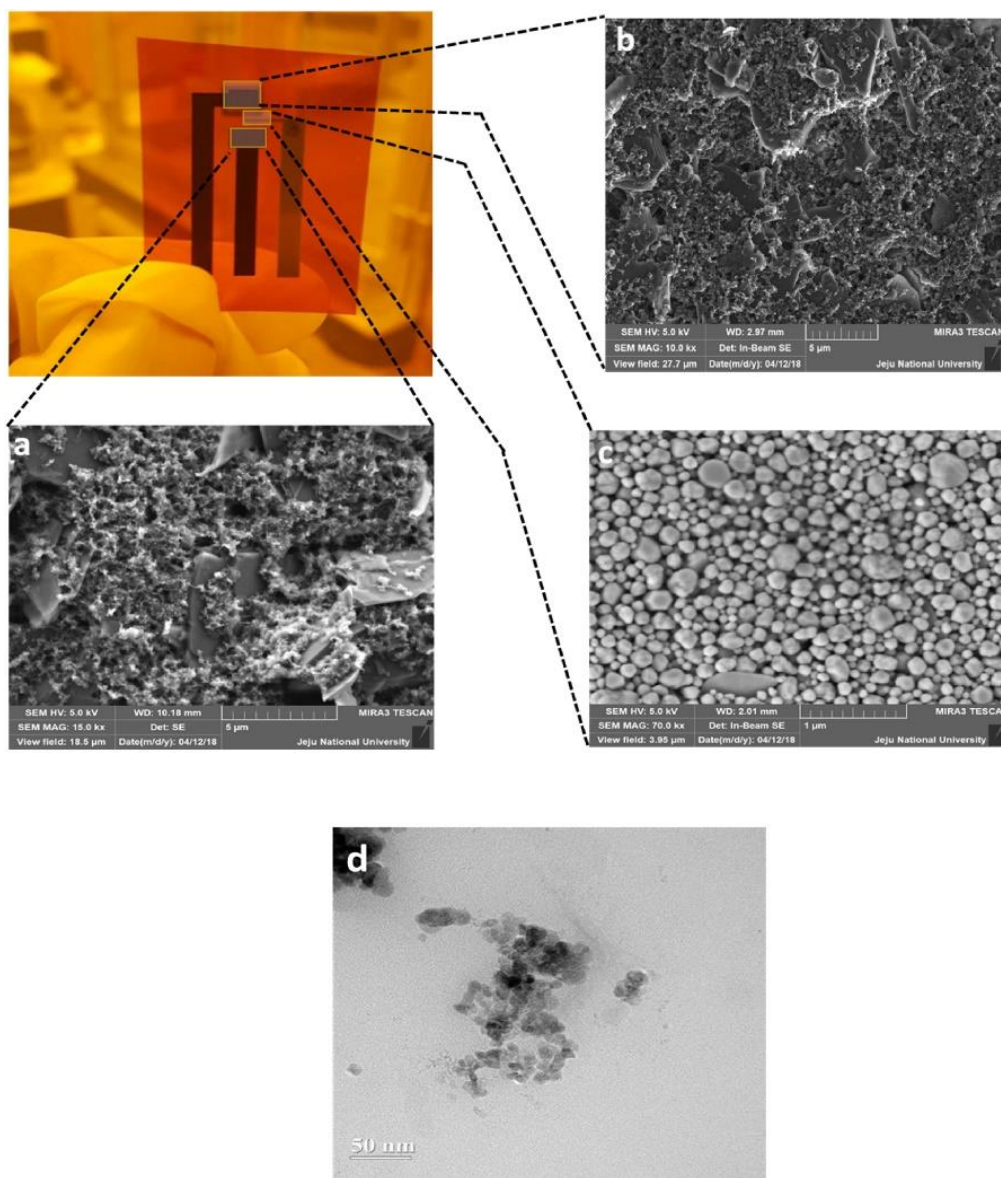


Figure 2-3: FESEM images of biosensor **(a)** 5 μm magnification of counter electrode **(b)** 5 μm magnification of working electrode, carbon electrode with ZnO QDs **(c)** 1 μm magnification of reference electrode (Ag/AgCl). **(d)** TEM images of ZnO QDs.

2.1.5. Results

The sensing response of the screen-printed sensor was analyzed by measuring the voltammogram using cyclic voltammetry (CV) system. UA is insoluble in phosphate-buffered saline (PBS), but soluble in NaOH. The solubility of UA in NaOH is 50 mg/ml @ 20 °C A stock solution was prepared and then further diluted in DI water to make different aliquots. Uric acid (low solubility) in the

presence of uricase produces allantoin (high solubility) along with carbon dioxide and hydrogen peroxide. The byproducts produced in turn react with H-OH to gives allantoate (an anion responsible for the detection of UA) as shown in Fig. 2-4(a), interact with ZnO QDs and produce potential shift at the electrode [36]. Fig.2-4(b) is showing the voltammogram of SPE biosensor in which the modified carbon electrode by ZnO QDs is utilized as a working electrode, unmodified one as a counter and Ag/AgCl as a reference electrode.

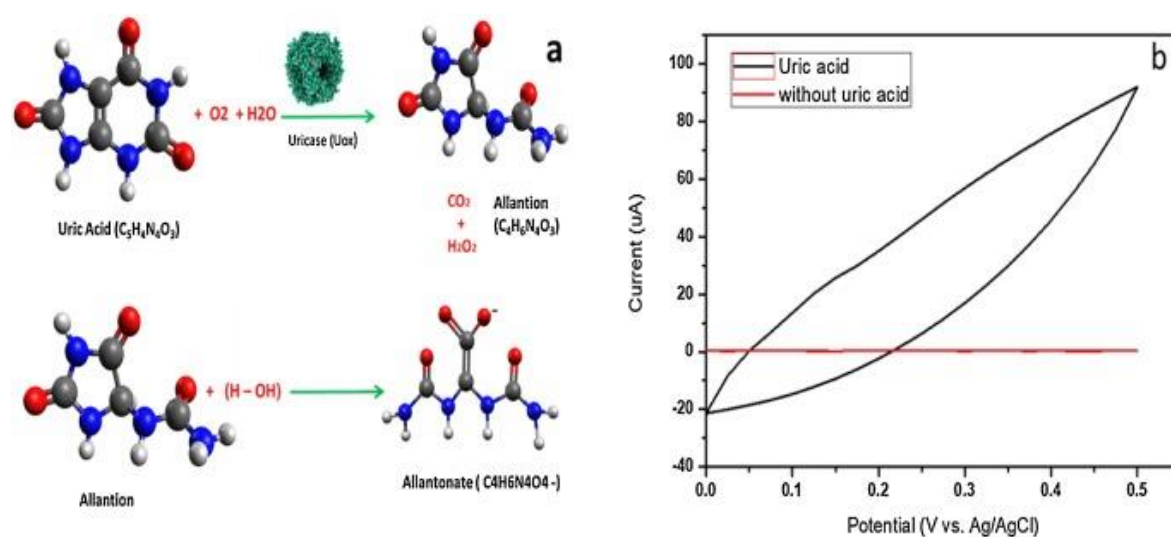


Figure 2-4: (a) Reaction mechanism of UA in the presence of the uricase and (b) initial voltammogram of the sensor in the presence and absence of analyte (UA).

Eventually, the QDs modified area of the working electrode was functionalized with uricase for detection of uric acid. To examine the optimum potential for the UA detection, the potential was swept from 0 V to 0.6 V with a scan rate of 250 mVs^{-1} . The CV curves can reflect the oxidation and reduction reaction that occurs on the surface of the electrodes by introducing 10 mM of UA while remained absent to response in the absence of the analyte (red line). The pattern of cyclic voltammogram denoting that the current increases in the presence of UA, this rise in current density is attributed to the allantoate generating by the enzymatic reactions. Fig. 2-5(a) shows the cyclic voltammogram, which was performed in an unstirred solution of UA with the concentration ranges from 1 mM to 10 mM. The oxidation and reduction reactions were observed from the

reaction that occurs on the surface of the working electrode. ZnO QDs increased the surface area for enzyme immobilization and uphold the bioactivity of the enzyme as well. The current vs concentration curve laid out in Fig. 2-5(b) illustrates the QDs sensor exhibited a straight response to uric acid concentration with a correlation coefficient of 0.996 under cyclic voltammetry. The Chronoamperometry behavior of the sensor was tested in uric acid solution at an applied potential of 0.6 V under constant stirring. An exemplary Chronoamperometry plot is shown in Fig. 2-5(c), which incorporates the time vs current graph. It was collected by adding a different concentrated solution of uric acid at regular intervals. The UA sensor could be seen to respond faster to the addition of increasing the concentration of target analyte from 1 mM to 10 mM. The sensor showed a stable response between the additions. The same data was plotted to get a calibration curve by providing the steady-state current values to the corresponding concentrations. A linear curve was obtained for a typical QDs based UA sensor showing a linear response as shown in Fig. 2-5(d). The sensitivity of the sensor was obtained from the slope of the line, which equals a value of $4.0 \mu\text{A}/\text{mM}\cdot\text{cm}^{-2}$ with a correlation factor of 0.996. These results showed that this sensor responded productively to UA addition with a calculated LOD of $22.97 \pm 10 \mu\text{M}$. These results yield high sensitivity, longer linear detection range, and low limit of detection in comparison with the previously reported uric acid sensors as shown in Table 1. The most significant is the detection range, which covers the physiological range of uric acid present in the urine samples (1.5–4.4 mmol/day).

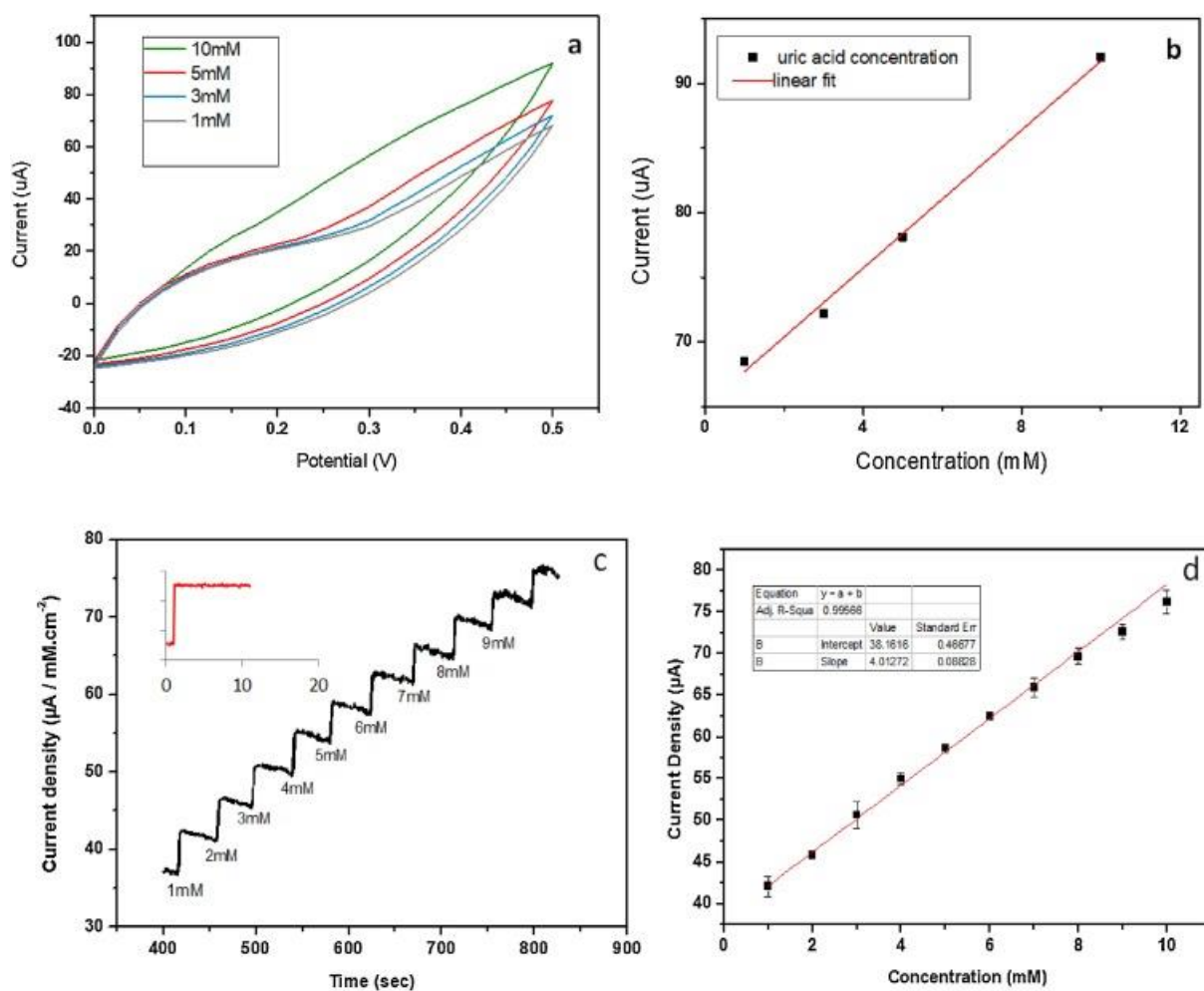


Figure 2-5: Cyclic Voltammograms and typical response of Chronoamperometry of the printed sensor for UA (a) UA acid in NaOH solution from 1 mM up to 10 mM concentrations and (b) a calibration curve for the response of current vs UA concentration of the printed sensor at 0.6 V (c) chronoamperometric response of the sensor with a subsequent increase in the concentration of UA keeping the potential at 0.6 V (d) calibration curve for the response of printed sensor with successive addition of 1 mM of UA concentration

Table 1. Comparison of the proposed three electrodes based uric acid biosensor with the other reported different structures of ZnO electrode for uric acid.

Biosensor composition	Sensor type	Sensitivity (μAcm ⁻² mM ⁻¹)	Linear Range	LOD	Ref.
Uricase immobilized on ZnO nanowires	Enzymatic	32 mV/decade	1-1000 μM	-	49
GOx-ZnO film/glass	Enzymatic	-	0.2-40 μM	200 μM	50

Uricase on ZnO nanorods	Enzymatic	0.1054 $\mu\text{A}/\text{mM}$	5 μM -3 Potential mM	-	51
Uricase/Chi-CNTs NF/AgNPs/Au biosensor	Enzymatic	20.5 $\mu\text{A}/\text{mM}$	1.0-400 μM	1.0 μM	52
Uricase/ZnO NWS	Enzymatic	-	1 μM to 1 mM	-	53
Nafion/Uricase/ZnO micro/NWS/Au	Enzymatic	-	0.1-0.59 μM	25.6 μM	54
Nitrogen-doped zinc oxide thin films 40		-	50-1000 μM	40 μM	55
Pt nanoparticles supported on reduced graphene oxide	Non-Enzymatic	-	10.0-130.0 μM	0.45 μM	56
Hierarchical nanoporous PtTi alloy	Non- enzymatic	-	0.1-1 mM	5.3 μM	57
Nitrogen-doped zinc oxide thin films	Non-Enzymatic	-	0.01-100 μM	0.0032 μM	58
Nafion/ZnO QDs/Uricase	Enzymatic	4.0 $\mu\text{A}/\text{mM}\cdot\text{cm}^{-2}$	1mM-10mM	22.97 μM	This work

2.1.6. Application: detection of UA

For real time analysis, the ZnO QDs based biosensor was applied for uric acid determinations in urine samples using standard addition method. In this method, a known amount of analyte added to the sample solution. The urine samples were diluted with PBS (0.1 M, pH = 7.0). After the appropriate dilution and spiked with a certain amount of UA, was analyzed by the proposed sensor. The recovery for the determination of UA is in the ranged between 96% and 104% presented in Table 2.

Table 2. Determination of UA levels in urine samples using the ZnO QDs based SPE sensor.

Samples	Content (mM)	Added (mM)	Found (mM)	Recovery %
Urine 1	1.1	2.1	3.25	104
Urine 2	1.5	2.5	3.95	96
Urine 3	3.5	1.5	4.95	98

2.2. Electrochemical based detection of lactate through novel composite (MWCNTs/PEDOT:PSS)

2.2.1. Background

Interfacing biorecognition elements on transducers surfaces is a challenging area in the fabrication of biosensors. Nanomaterials exhibit as a stimulating tool in the realization of coupling biomolecules with electronic circuitry. Highly efficient immobilization of enzyme is the key factor by suitable physical and biochemical approaches and is the crucial phase for electrochemical biosensors. A variety of biocompatible nanomaterials and polymers such as chitosan, dopamine (PDA), and poly (l-PDA) have been utilized for enzyme immobilization and metabolites detection. Polymers based immobilization is providing high-loaded and high activity hold of enzymes, which is a stimulating subject to develop biosensors devices^{18, 59-61}. Among the library of conductive nanomaterials, carbon nanotubes (MWCNTs) have received extensive recognition in biosensing usage due to high conductivity, gross specific surface area, mechanical stability, minimization of surface fouling, and flexibility^{19, 20, 62}. The large surface area of CNTs enables the immobilization of the large number of bioreceptors and making them an excellent candidate in biosensing applications. CNTs have also been accepted as an outstanding material in electrochemical biosensors due to their excessive electron transfer rate^{63, 64}. Due to the admirable nature of

MWCNTs, have also been adopted in a variety of desirable applications including batteries, supercapacitors, electrochemiluminescent, and transistors⁶⁵. CNTs can serve as support for the immobilization of bioreceptors such as DNA, peptides, and proteins^{66, 67} which makes them the best-studied materials for transduction. Up to date, the conjugated polymer PEDOT: PSS has been identified as one of the highest efficient conductive polymers, due to its well-founded conductivity, ease of processability, and excellent stability under ambient settings⁶⁸. Furthermore, PEDOT:PSS owes its reversible charge/discharge capability to doping/de-doping of the polymer chain⁶⁹. PEDOT: PSS is highly sensitive to ionic species in aqueous solutions, which makes it more attractive to be used in organic electronics applications. Additionally, PEDOT:PSS has shown affordable stability for a variety of in-vitro electrophysiology applications⁷⁰. Among conducting polymers, PEDOT:PSS has shown several advantages like biocompatibility, flexible molecular backbone, high conductivity (with low oxidation potential and low bandgap), highly remarkable stability, cost-effective, and enzyme immobilization⁷¹⁻⁷³. The combination of MWCNTs with a number of polymers such as polyaniline, polydopamine, and polypyrrole have also been evaluated and is adapted as a capable route to advance highly soluble CNT-based nanocomposite for the electrochemical detection^{74, 75}. The aforementioned properties of PEDOT:PSS has been showing numerous advantages and could be modified by mixing with MWCNTs to meet better application requirements. MWCNTs dope them an excellent candidate to be effectively form a continuous and even conductive network structure. “ π - π interaction” sandwiched between the thiophene ring and carbon nanotubes assisting the ease in electrons flow through the polymer matrix. This network drives the conductivity up to the mark in polymer matrix. Incorporation of biopolymer for the immobilization of the LOX can be favorable, thereby enhancing the enzyme performance. In this study, we have avail PEDOT:PSS/MWCNTs as a nanocomposite for the electrochemical detection of lactate for the first time.

2.2.2. Nanocomposite synthesis and electrode functionalization

A range of (0.10 to 0.2) wt% dispersion of MWCNTs were prepared and analyze the composite film conductivity in PEDOT:PSS. Finally, a dispersed solution of multi-walled carbon nanotubes was prepared in Dimethylformamide (DMF) solvent by putting 50 mg in 25 ml (0.2 wt%) and ultra-sonicated for 25 min to ensure that MWCNTs have been fully dispersed. A completely dispersed solution was obtained. PEDOT:PSS (3.0–4.0 wt.%) ink (Sigma Aldrich) was subsequently added to MWCNTs dispersion in a 2:1 and again probe sonicated for 2 h. The PEDOT:PSS/MWCNTs composite preparation in graphical representation is shown in Fig. 2-6.

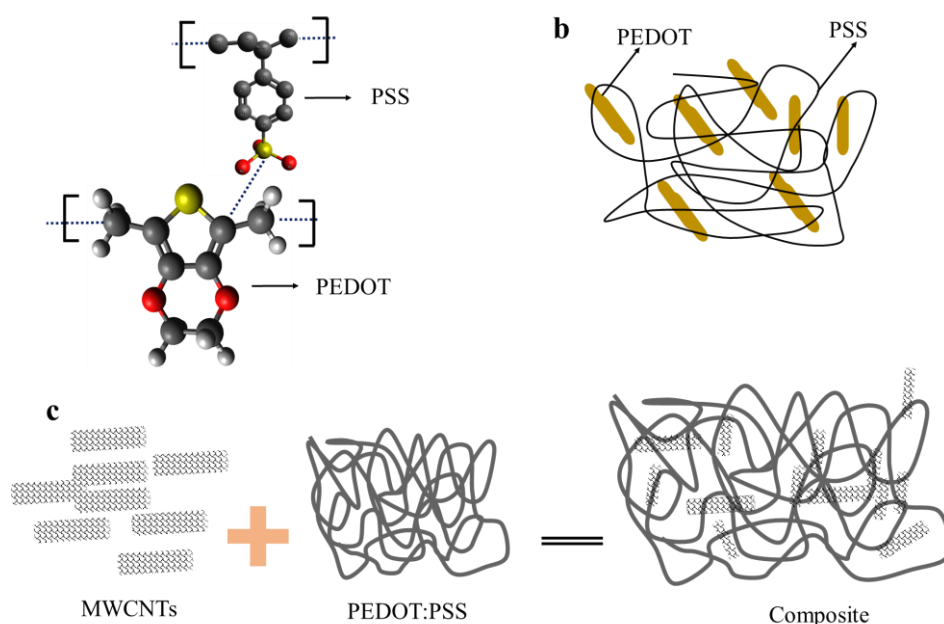


Figure 2-6: (a) Chemical structure of PEDOT:PSS, (b) Schematic structure of PSS doped PEDOT, and (c) Schematic representation of MWCNT/PEDOT:PSS composite

The mixture of MWCNTs and PEDOT:PSS was centrifuged at 1300 rpm for 5 min to take out the big bundles formed in the solution. It was repeated 3 times and the supernatant solution was collected and obtained a well clear solution of PEDOT:PSS/MWCNTs composite. The composite was then bath sonicated for 4 hr. The viscosity of the synthesized composite was measured by SEKONIC VISCOMATE, which equals 3.2 cp. A carbon screen-printed electrode was used (obtained from Dropsens) consisting of a carbon working electrode (WE) (4 mm), a counter

electrode (CE), and a silver patterned reference electrode (RE). Before the modification of the WE, the electrodes were rinsed with ethanol and eventually with deionized (DI) water to remove the organic residues. To modify the WE, an amount of 20 μl (MWCNTs and PEDOT: PSS) was drop cast using a micropipette and it was ensured that the composite had covered the whole surface (4 mm) of the WE. The film was dried at room temperature (25°C) and was further sintered at 60°C for 30 min before any further characterization. Followed by the surface modification, LOX (20 mgml^{-1} /GA~2%) mixed with EDC:NHS (1:1) was hand-cast on the WE for immobilization. Due to the highly porous and hydrophilic nature (CA \sim 59.4°) of the MWCNTs and PEDOT: PSS, enzyme droplets were easily absorbed into the matrix. Eventually, tailed by the BSA (50 μgml^{-1}) thereby to decrease the background reading and enlarge the signal-to-noise (S/N) ratio through blocking. A base layer of MWCNTs/PEDOT:PSS was molded on the WE exposed area, which facilitates carboxyl (COOH) functional groups and proved to be covalently attached to the enzyme having amine functional groups (-NH₂). The graphical representation is shown in Fig. 2-7. The functionality of the -OH groups used for the covalent attachment of the enzyme provides high electronic density to the biosensor surface and also acts as an antifouling layer for the anionic interferences in the biological media. Before dispensing the composite, the WE was treated with Nafion (4 μl , Perfluorinated resin solution) and left to dry for 2 h. The sensor was stored at 4°C overnight.

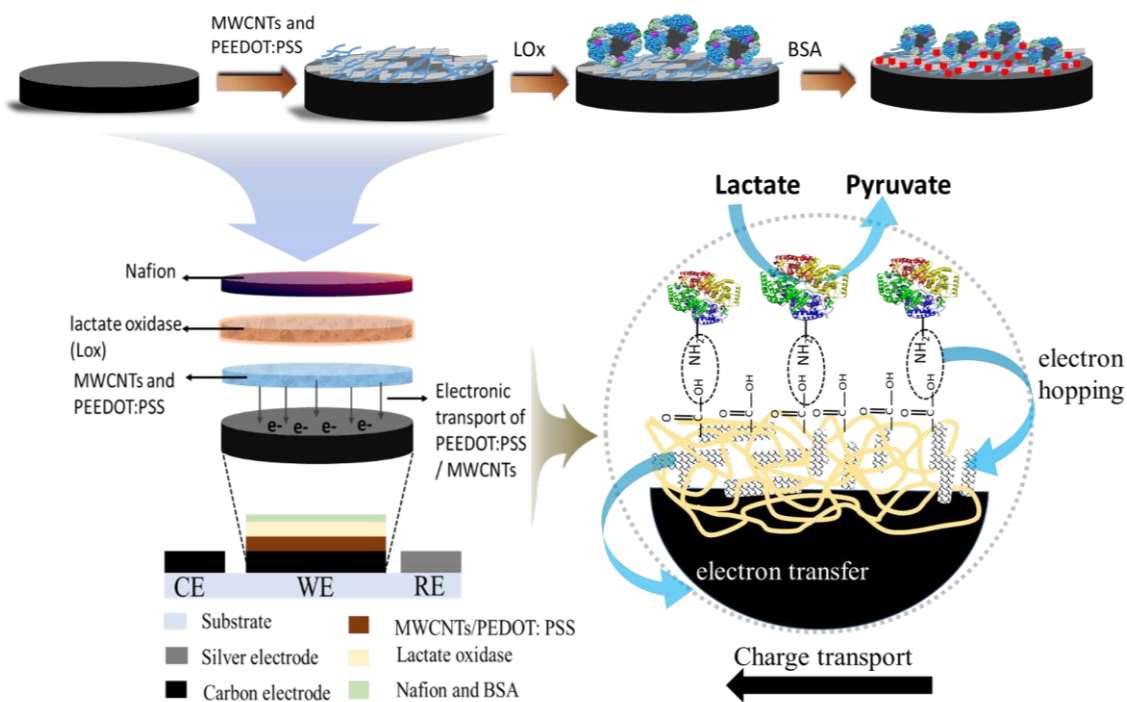


Figure 2-7: Depiction of an electrochemical sensor for lactate detection, modification of WE by drop-casting MWCNTs, and PEDOT: PSS composite, followed by lactate oxidase and BSA along with the mechanism of the reaction.

2.2.3. Composite characterizations

To investigate the structural characteristics of the composite were examined by Raman spectroscopy at $\lambda_{exc} = 514 \text{ nm}$. Fig. 2-8 shows the spectra of PEDOT:PSS, MWCNTs, and their composite. Pure MWCNTs have shown sharp peaks lie around 1342 cm^{-1} and 1580 cm^{-1} , which accord to graphite E2g mode and MWCNTs disordered A1g mode, respectively. These two peaks are due to the optical phonon modes in the first-order of the Raman spectrum of the MWCNTs. These shifts in the spectra are closely defined D and G band correspondingly, which are associated with C–C stretching in graphitic materials and is known to all sp^2 carbon atom ⁷⁶. The same individual pure PEDOT: PSS was characterized and the main Raman peaks lie in the range of 1000 to 1800 cm^{-1} such as 1129 cm^{-1} , 1256 cm^{-1} , 1365 cm^{-1} , 1450 cm^{-1} , and 1571 cm^{-1} , subsequently. These peaks indicate the C–C in-plane bending, in-plane systematic stretches, stretching deformations, $\alpha=\beta$ symmetric, and asymmetric vibrations respectively ⁷⁷. At the

same time, the Raman spectrum of the PEDOT:PSS/MWCNTs composite was obtained and has shown all the relevant peaks. As one can notice, there is one peak generated at 1285 cm^{-1} , this shift shows that there is physio-chemical interaction between PEDOT: PSS and MWCNTs, and this peak is absent in the pure spectrum of PEDOT: PSS.

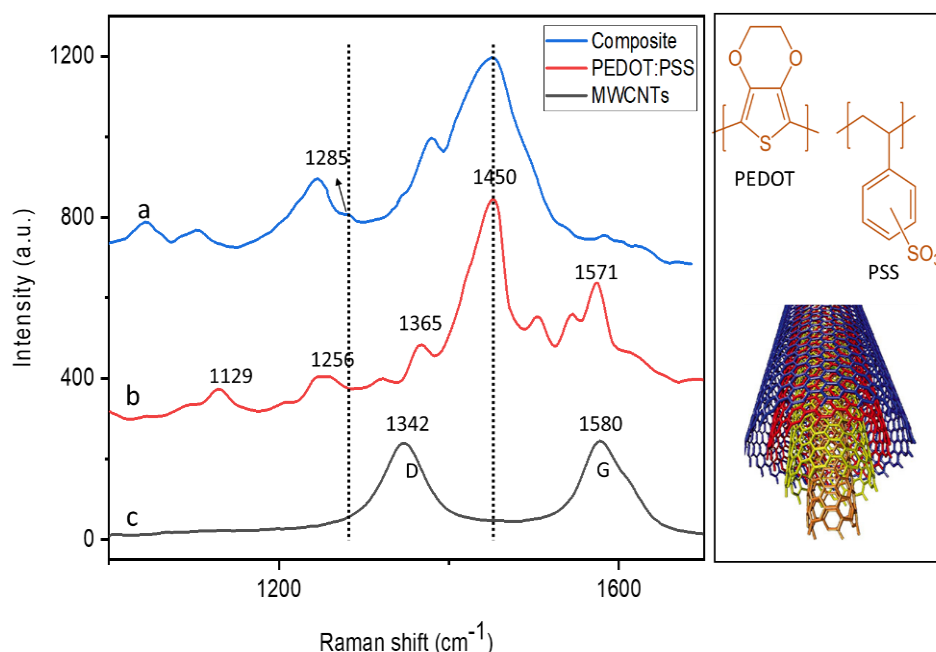


Figure 2-8: Raman spectra of (a) the composite MWCNTs and PEDOT: PSS, (b) PEDOT: PSS, (c) and MWCNTs

FESEM was used to show the morphologies of the MWCNTs, PEDOT:PSS, and MWCNTs/PEDOT: PSS composite. Fig. 2-9(a) shows an image of the dispersed MWCNTs /PEDOT: PSS composite. Fig. 2-9(b) is showing MWCNTs dispersion in DMF solvent (supported by Raman analysis as depicted in Fig. 8) observed under 500 nm resolution. Fig. 2-9(c) is showing an individual SEM image of the conductive polymer (PEDOT: PSS). Fig. 9d is presenting a composite of MWCNTs and PEDOT: PSS confirms a completed dispersion of MWCNTs and conductive polymer. The covered PEDOT:PSS on MWCNTs retains the mesoporous mesh of nanotubes which is highly desirable to maximize the surface area, supports the immobilization of LOX on the surface of the WE. EDX analysis was carried out to obtain the elemental analysis of the individual components and the composite. As shown in Fig. 2-10(a) the elemental mapping image of MWCNTs, which endorse

the presence of C and O and the intensities of peaks are indicating their atomic percentages. In the same manner, the elemental mapping image of PEDOT: PSS is shown in Fig. 2-10(b), which shows the presence of C, O, and S in the sample, and their atomic percentages, which are as follows: 83.5, 15.3, and 1.2 percent, respectively. The EDS images of the MWCNTs/PEDOT: PSS composite has been shown in Fig. 2-10(c), which confirm the elemental percentages along with their peaks. The percentages of C, N, and S in the composite are 80.8, 15.3, and 3.9 percent, respectively.

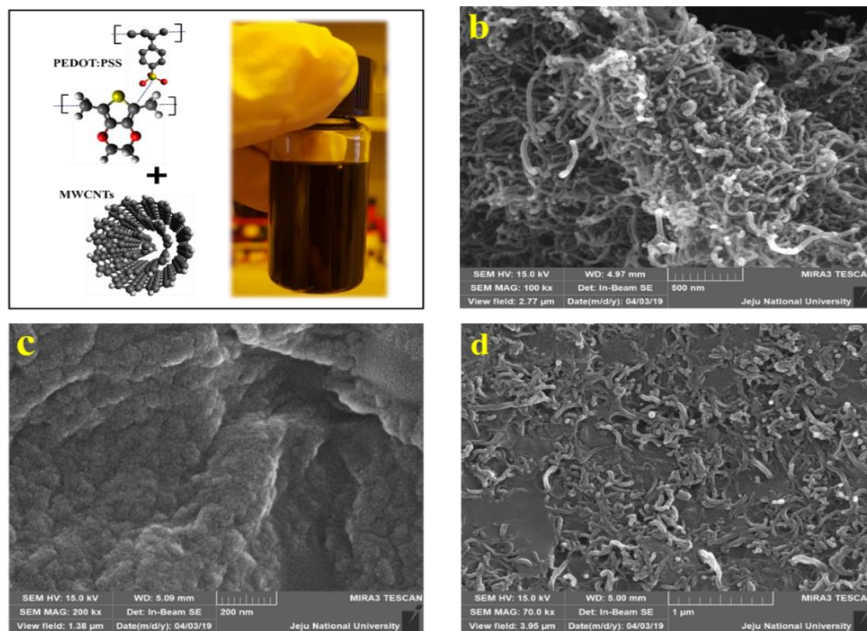


Figure 2-9: Typical FESEM images. **(a)** MWCNTs and PEDOT: PSS ink, **(b)** Observed for MWCNTs under the resolution of 500 nm, **(c)** PEDOT: PSS under the resolution of 200 nm, **(d)** composite synthesized under the magnification of 1 μm

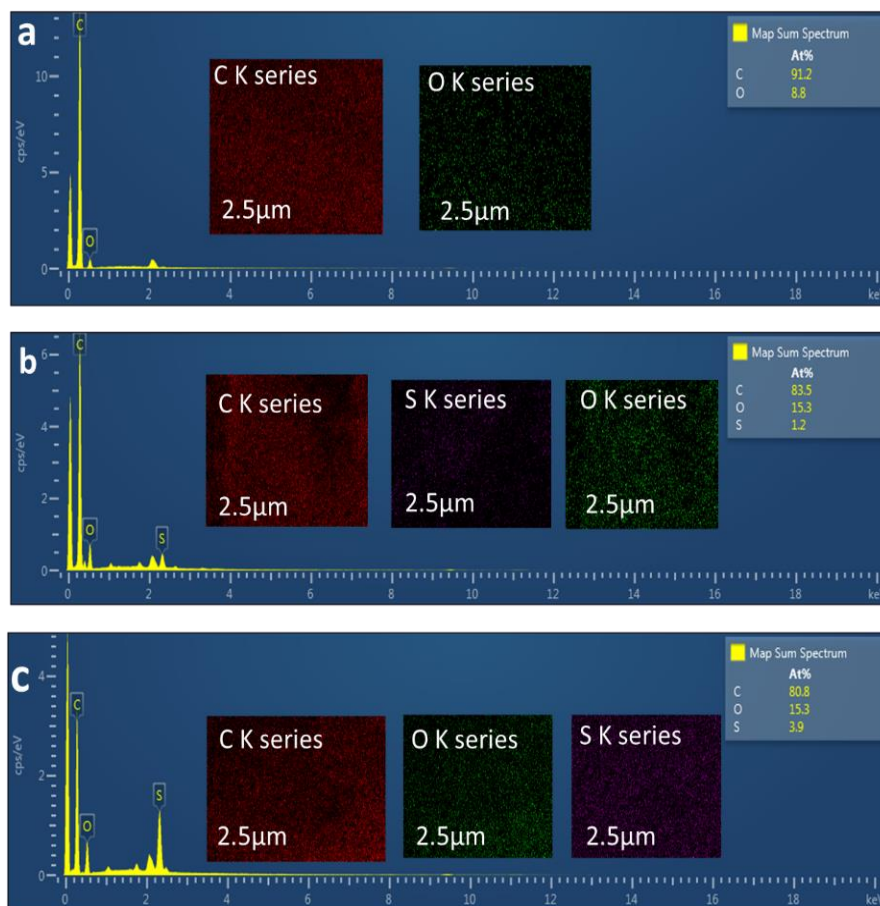


Figure 2-10: Energy-dispersive X-ray spectroscopy (EDX) and elemental mapping of (a) MWCNTs, (b) PEDOT:PSS, and (c) composite of MWCNTs and PEDOT: PSS

The surface characteristics of the screen-printed carbon electrode and modified MWCNT/PEDOT: PSS composite film on the WE was studied thoroughly to evaluate its surface roughness. The increase in surface area of the WE after the modification was confirmed by topographical AFM images as shown in Fig. 2-11. To evaluate the wettability of the modified surface for the immobilization of the enzyme, the WE was examined by studying the contact angles of water droplets. In this study, the contact angle for the unmodified electrode for water droplet is 95.1° showed a hydrophobic surface. In contrast, the modified surface with the composite has shown the hydrophilic surface (45.6°) as shown.

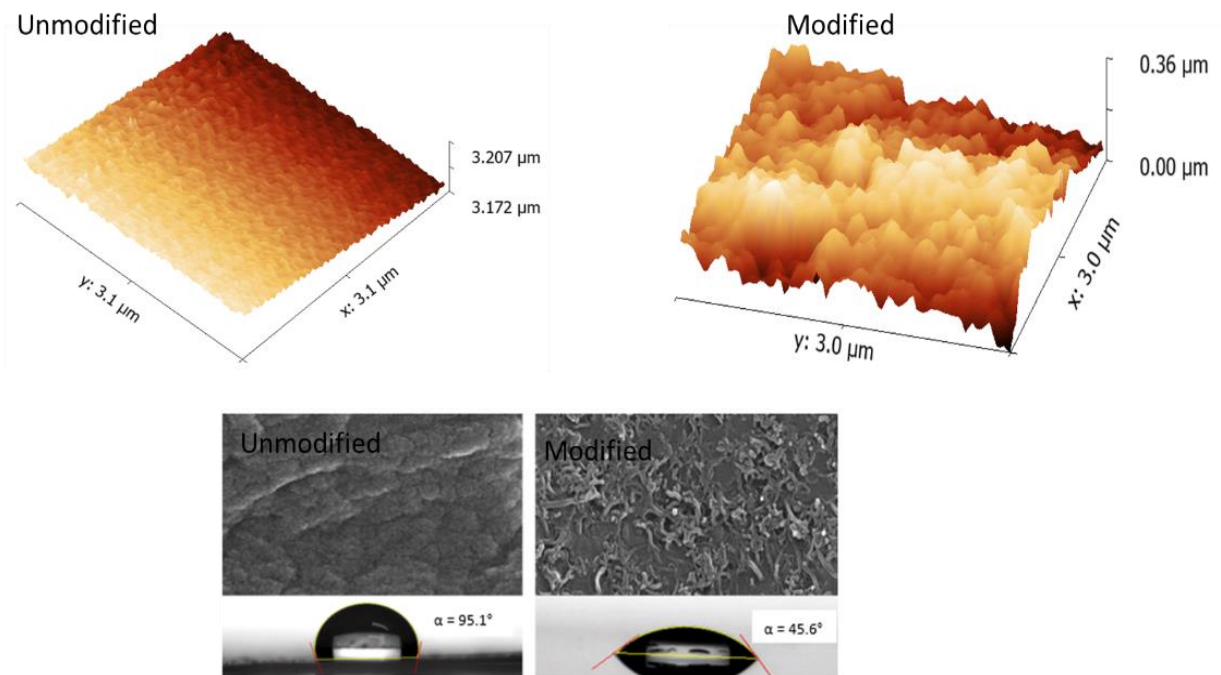


Figure 2-11: AFM images of the surface of an unmodified carbon electrode and PEDOT:PSS/MWCNTs composite modified surface along with the contact angle images

2.2.4. Optimization of analytical parameters

The performance of the lactate sensor was effectively dependent on the related experimental parameters. Various parameters including temperature, pH, applied potential, and BSA concentration were optimized. The details are given in Fig.2-12.

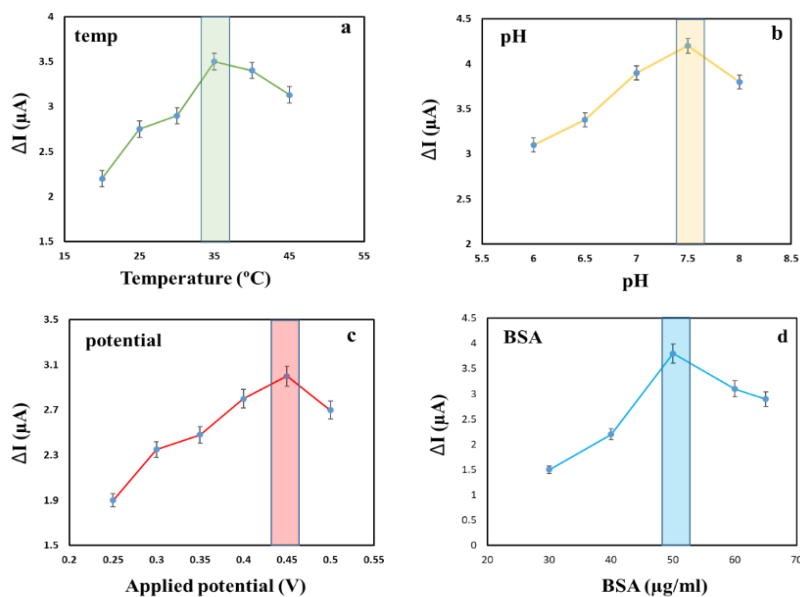


Figure 2-12 Optimization of different sensing parameters **(a)** Temperature, **(b)** pH, **(c)** Applied potential, and **(d)** BSA concentration with 1 mM lactate. Mean \pm standard deviation (SD), n = 3

2.2.5. Analytical performance of the sensor

The sensing mode of the modified SPCE has been evaluated by measuring the voltammogram. PalmSens potentiostat was connected to the SPCE, controlled by PStrace 5.3 software. The Voltammograms of blank and modified WE as shown in Fig. 2-13(b). The blank SPCE did not show any redox peaks, the modified sensor has been showing high redox peaks in comparison to the unmodified one. The redox peaks (oxi-red) indicate the reversibility of the reaction on the surface electrode. Lactate oxidase converts L-lactic acid into pyruvate and hydrogen peroxide (H_2O_2), which is electrochemically dynamic and can be either oxidized or reduced on the surface of WE, resulting in the current directly proportional to the lactate concentration. The sensor repeatability has been shown in Fig. 2-13(c) by repeating 5 cycles, which is endorsing the stability of the SPCE to the 1 mM lactate concentration.

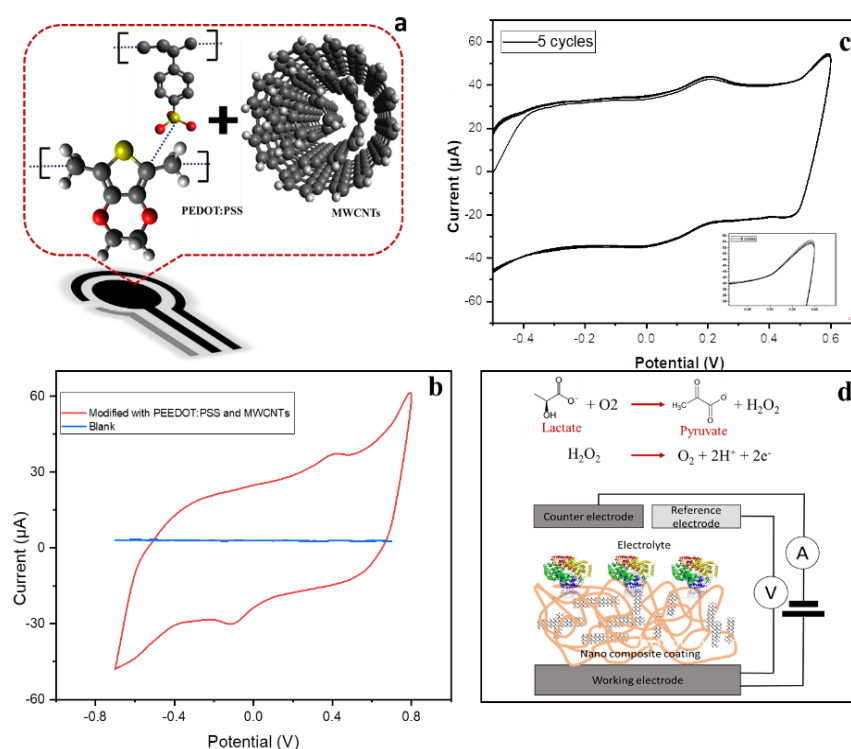


Figure 2-13: **(a)** Modification of WE **(b)** CV response of the sensor comprising blank, unmodified, and modified WE with PEDOT:PSS/MWCNTs in 10 mM K₄ [Fe(CN)₆] **(c)** stability test of the sensor,

after 5 cycles in the presence of 1 mM lactate (scan rate = 250 mV/sec) **(d)** conversion of lactate into pyruvate on the surface of WE along with the inset image of the three electrodes electrochemical setup used

Fig. 2-14(a) shows the CV curves of the introduction of various concentrations of lactate on the sensor surface, which was performed, in the range from 0.6 to 1.0 mM. LOX is an enzyme, adapted for its ability to catalyze the oxidation of lactate into pyruvate in the presence of oxygen. While the electrons taking part in the chemical reaction are abruptly transferring to the composite, regenerating the enzyme activity. PEDOT: PSS/MWCNTs composite was used as a sensing interface to catalyze the electrochemical oxidation of H₂O₂. The by-product H₂O₂ produced from the enzymatic reaction indicates the selective sensing of lactate. Additionally, the biocatalytic activity of the composite PEDOT:PSS/MWCNTs increases the surface to volume ratio for enzyme confinement and upholds the bio-stability of the bioreceptors (LOX) used for the detection of lactate. This CV response of the sensor is showing a linear range for the detection of lactate as shown in Fig. 2-14(b) with a correlation coefficient of 0.98. The analytical response of the SPCE modified electrode towards lactate has been evaluated using Chronoamperometry and an exemplary plot is shown in Fig. 2-14(c). The chronoamperometric response of the sensor has been evaluated in lactate solutions at a constant potential of 0.45V which incorporates the time vs. current graph for lactate concentrations by adding at regular intervals. As one can see from the figure, it has shown a stable response between different samples. The calibration curve is shown in Fig. 2-14(d) for a range of lactate concentrations that varies from 1mM to 10 mM. It indicates a wide linear range in comparison to the previously reported sensor for lactate with a limit of detection of $4.0 \pm 5 \mu\text{M}$ based on $S/N = 3$. The sensitivity of the sensor is $35 \mu\text{A}/\text{mM}$ along with a correlation coefficient of 0.98 ($n = 3$). These outcomes yield a very good response of the developed sensor based on the composite of PEDOT:PSS/MWCNTs due to the higher shuttling of the electrons between the redox center of the enzyme and the transducer. A comparison is

shown in table 3 regarding the recently reported literature of lactate biosensor with our approach.

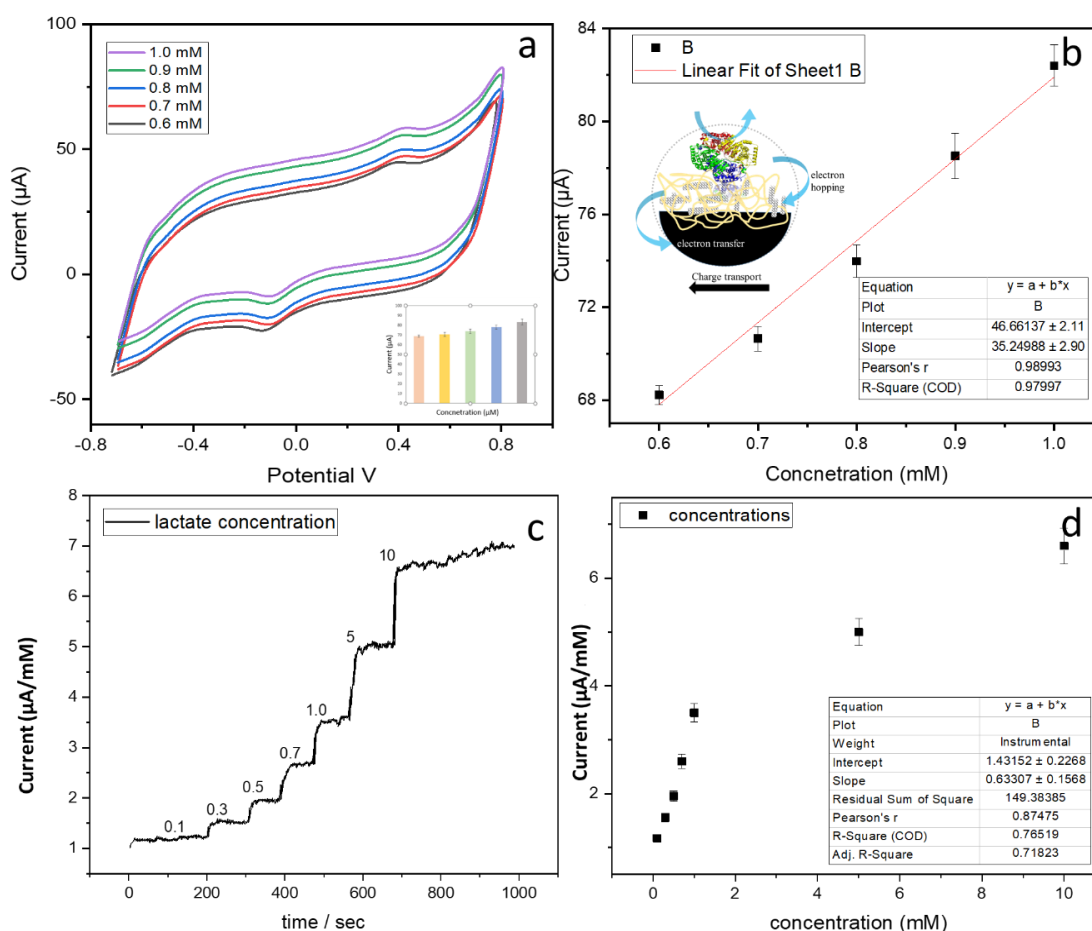


Figure 2-14: (a) Cyclic Voltammograms of the sensor for the detection of lactate ranges from 0.6 mM to 1.0 mM (b) calibration curve of the sensor for different lactate concentrations in the linear range (0.6-1.0 mM) (c) Chronoamperometric response of the sensor in various concentration of lactate, ranges from 0.1 to 10 mM along with (d) Calibration curve under the same experimental conditions, mean \pm standard deviation (SD), $n = 3$

Table 3. Analytical properties of lactate biosensors found in the literature.

Biosensor composition	Sensor type	Sensitivity ($\mu\text{Acm}^{-2} \text{mM}^{-1}$)	Linear Range μM	LOD μM	Ref.
Lox-Cu-MOF/CS/Pt/SPC	Enzymatic	14.650	0.00075 – 1.0	0.75	78
PS/MWCNT/Fc/LOx/HRP/SPCE	Bienzymatic	1168.8 $\mu\text{A M}^{-1} \text{mm}^{-2}$	0.0011–0.056	0.56	79
LO _x /PPD/PB/SPCE	Enzymatic	0.553	0.1–1.0	50.00	80
GCE, modified by nanoparticles ZnO and SWCNT	Enzymatic	NA	0.01–200	4.0	81
GCE, covered with Prussian blue	Enzymatic	NA	1 – 800	1.0	82
Printed graphite electrode	Enzymatic	NA	100 – 1000	84.8	83
GCE, modified by MoS ₂ nanosheets	Enzymatic	2.1	56 – 770	17	84
Polycarbonate disk	Enzymatic	NA	0.9 –1500	0.9	85
LOx/PtNp-CNF-PDDA/SPCEs	Enzymatic	36.8	25–1500 μM	11 μM	86
MWCNTs-PEDOT:PSS-Lox-SPE	Enzymatic	35.24	0.6-1.0 μM 1-10 mM	4.0 \pm 2 μM	This work

2.2.6. Application: lactate detection in cancer cells media

For real-time data samples, the developed sensor was tested under the evaluation of cell culture media to demonstrate the ability of the biosensor using the standard addition method. In this approach, a known amount of analyte solution was added to all three samples and was evaluated. Lactate concentration in cancerous cells is very high, MCF-7 breast cancer cells were cultured and loaded with RPMI media for two days and the media was then collected to detect

lactate concentration through SpectraMax i3 Multi-Mode Platform. Inverted microscopic images of the MCF-7 cells are shown in Fig. 2-15. A protocol of the commercial lactate colorimetric/Fluorometric Assay kit was also simultaneously used for the accuracy of the proposed sensor. The cell culture media had the following concentrations of 1.5, 2.6, and 4 mM of lactate detected through the colorimetric method. Table 1 displays the results obtained from the proposed lactate biosensor and the colorimetric assay kit and the recovery of the samples are summarized in Table 4. The biosensor developed has the capability to precisely detect lactate in cell culture media, which expands the potential applications in drug screening toxicology in organ-on-a-chip applications. Fig. 8b illustrates the selectivity of the biosensor to determine the 1 mM lactate with reference to the interference (PBS, AA, Glucose, UA). The sensor response is not that much significant to interference molecules, exhibiting excellent selectivity for lactate.

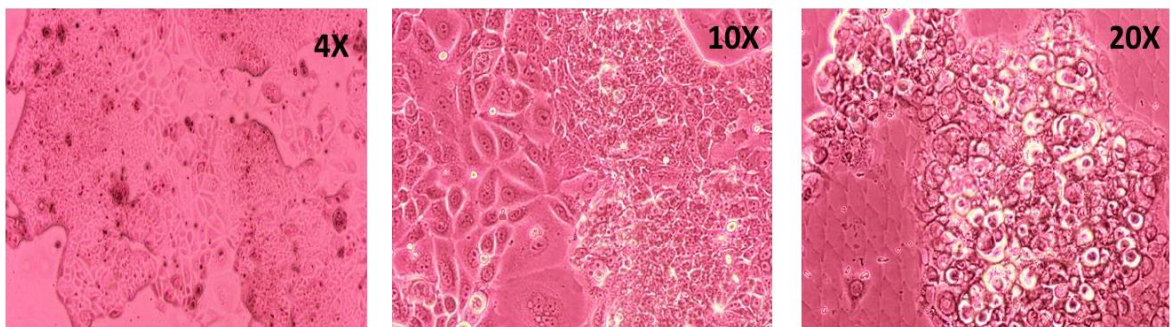


Figure 2-15: Pre seeding inverted microscopic images of MCF-7 cells at the resolution of 4, 10 and 20X

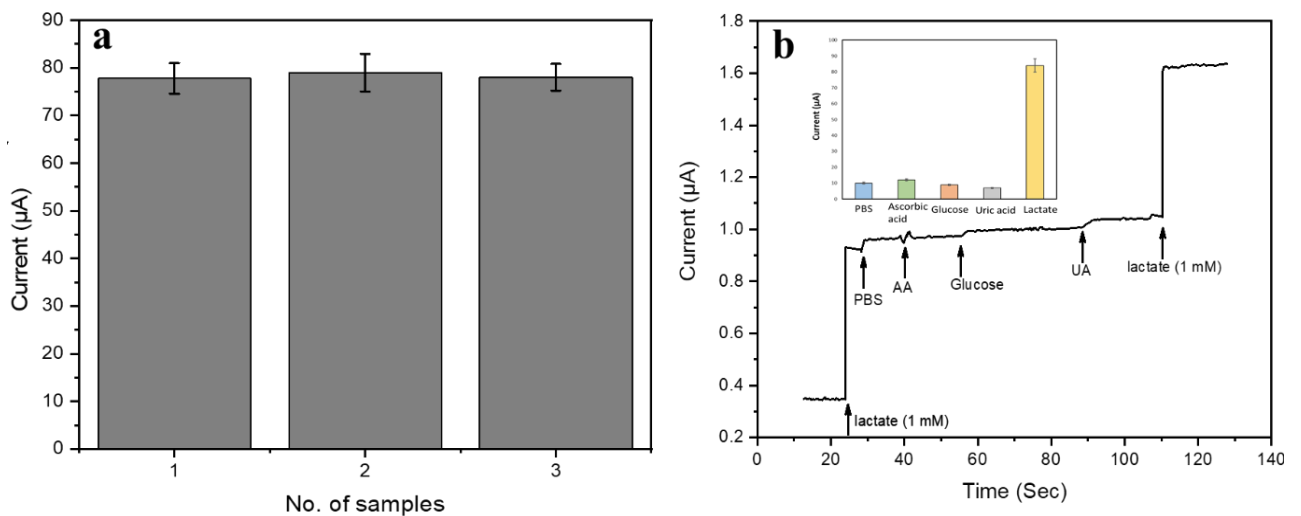


Figure 2-16: (a) Reproducibility measurements ($n = 3$), PEDOT: PSS and MWCNTs of four modified screen-printed electrodes prepared under the same protocol for the detection of 1 mM lactate (pH 7.0), **(b)** selectivity of the biosensor, data presented as mean \pm SD, ($n = 3$)

Table 4. Displays the results obtained from the proposed lactate biosensor and the colorimetric assay kit

Samples	Known conc. (mM) (Colorimetric Kit)	Inject (mM)	Avg. value Detected (mM)	Recovery %
1	1.5	1	2.6	104
2	2.6	2	4.55	98
3	4.0	3	7.1	101

Chapter 3. Fluorescent based biosensor

3.1. Upconverting nanoparticles based vaspin biosensors strip overview

Visceral adipose tissue-derived serpin (Vaspin) is considered one of the newest adipocytokine, incorporated with insulin-sensitizing effect ⁸⁷, it has been potentially associated with obesity, insulin resistance, metabolic syndrome, and type-2 diabetes ⁸⁸. Type-2 diabetes mellitus (T2DM) is a nexus metabolic disorder that has influenced more than 150 million people globally and is guessed to become 439 million worldwide in 2030 ⁸⁹. Its prevalence is expected to increase exponentially around the world particularly in developing countries ⁸⁹. The level of Vaspin is considerably increased in type-2 diabetes patients as related to normal individuals and further increased in patients with both T2DM and coronary artery disease (CAD). Moreover, Vaspin correlates positively with body mass index, fasting plasma glucose, insulin, and Homeostatic model assessment, and Insulin resistant (HOMA-IR) in all patients with T2DM ($P < 0.05$) ^{90, 91}. Point-of-care (POC) diagnostic devices are essential in the health safety programs because of identifying the disease biomarkers at the patient site ^{30, 31}. To date, major advances have been accomplished in the development of miniaturized and portable devices in the field of the healthcare system for immune chromatographic strip (ICS)/lateral flow strip assay (LFSA) which became an imperative technology for speedy analysis due to its low cost, simple handling, and less conclusion time ⁹²⁻⁹⁴. On the other hand, nanotechnologies have developed and created an exemplary shift in the field of biosensors which is one of the most well-known methods of diagnostics, clinical analysis, and environmental monitoring ⁹⁵. A great alternative to counterfeit the difficulties of sensitivity associated with colorimetric detection, fluorescent nanoparticles could be used. Fluorescent based various biosensors and chemosensors ⁹⁶⁻⁹⁸ using AIE active molecules and are promising for biomedical applications ^{99, 100}. A highly sensitive optical-based biosensor requires a fluorescent bio label, which can give quantitative

results such as DNA biosensor¹⁰¹ tetrodotoxin¹⁰² and Hg²⁺¹⁰³. Up-converting nanoparticles (UCNPs) based aptasensor can be developed for the detection of Vaspin¹⁰⁴. At present, UCNPs have been used to detect hepatitis B¹⁰⁵, Brucella¹⁰⁶, Schistosoma circulating anodic antigen¹⁰⁷, interferon- γ (IFN- γ), cTnI and PSA, and target-DNA resulting in higher sensitivities. UCNPs have the advantages of being biocompatible, stable results, low background light, high sensitivity, and most importantly low cost and no bleaching effects and blinking unlike many quantum dots¹⁰⁸. In light of all the above discussion, we have developed a fluorescent-based LFSA for vaspin. UCNPs conjugation with secondary aptamers has been established which has the potential for enhanced sensitivity, reproducibility, stable fluorescence, cost-effective nanoparticles, and quantitative results of Vaspin as contrary to its counterpart based on AuNPs. The quantity of Vaspin present in the serum can provide critical information about the mentioned diseases using a relatively simple and easy procedure. As per our knowledge, this is the first report of fluorescence-based LFSA for the quantitative detection of vaspin using covalently bounded conjugates. This LFSA is so far the most sensitive method reported for the rapid detection of Vaspin without the additional signal amplification and use of conventional fluorescence dyes. This LFSA can detect Vaspin in the human serum in the range of nanomolar concentrations. The promising properties of the UCNPs conjugate analyzed are reported below.

3.1.1. Nanoparticles (NayF₄: Yb, Er) size reduction

NayF₄: Yb, Er (20 mol%, 2 mol%) up-conversion particles were ordered from Sigma Aldrich which have been synthesized by hydrothermal/salvo process having a coating of oleic acid. The sizes of the particles were reduced in mortar and pestle by grinding them for 4 h. A colloidal solution was then made in ethanol to be further processed by ultrasonic probe sonication. Subsequently, the solution was centrifuged at 8000 rpm and the supernatant was separated to obtain reduce size particles

3.1.2. Functional group exchange Mal-PEG-COOH

For covalent linkages, the surface of UCNPs has to be functionalized with an appropriate (maleimide) functional group to bind with the biomolecule functional group (thiol)^{109, 110}. Ligand exchange of UCNPs was performed according to the previous report with customization. Approximately 5 mg of oleic acid-coated UCNPs were added to 50 mg of Mal-PEG-COOH (1000) dissolved in 500 μ l ethanol. The solution was kept in an Argon atmosphere and was shaken in a thermomixer (1000 rpm) for 48 h at 40 °C. To precipitate the UCNPs coated with Mal-PEG-COOH, hexane was added to the mixture. The nanoparticles were isolated through centrifugation and washed with ethanol. Finally, a dispersion of 1 mg ml⁻¹ of the nanoparticles in ethanol was stored at 4 °C under slow rotation. Before the coupling reaction with thiolated aptamer (secondary aptamer), ethanol was removed by centrifugation (4000 rpm) and was replaced by PBS. Functionalization can also be done by salinization but it aggregates after reacting with biomolecules.

3.1.3. Bioconjugation of aptamers

Aptamers are short oligonucleotides having the capability to bind to a specific target-oligonucleotide analyte (VASPIN). The details of the entire DNA oligonucleotides (aptamers) used in this study are provided in Table 5, which were selected by using the SELEX process and were acquired from Genotech company Korea. A new labeling strategy has been developed to conjugate the thiolated aptamer with the functionalized UCNPs as shown in Fig. 3-1. The thiol group of the secondary aptamer reacts with the double bond of maleimide to form a carbon-sulfur bond (thioether bond formation). The modified UCNPs were provided with long PEG chains which will be reducing the unspecific binding. So the 500 μ l maleimide-activated UCNPs and 26 μ l secondary aptamer-SH (10 nM) were mixed in PBS (pH = 7.4). After 24 h reaction at 4 °C, excess aptamers were removed by centrifugation, and the resultant UCNP-PEG-aptamers were re-suspended in PBS and stored at 4 °C for further experiments.

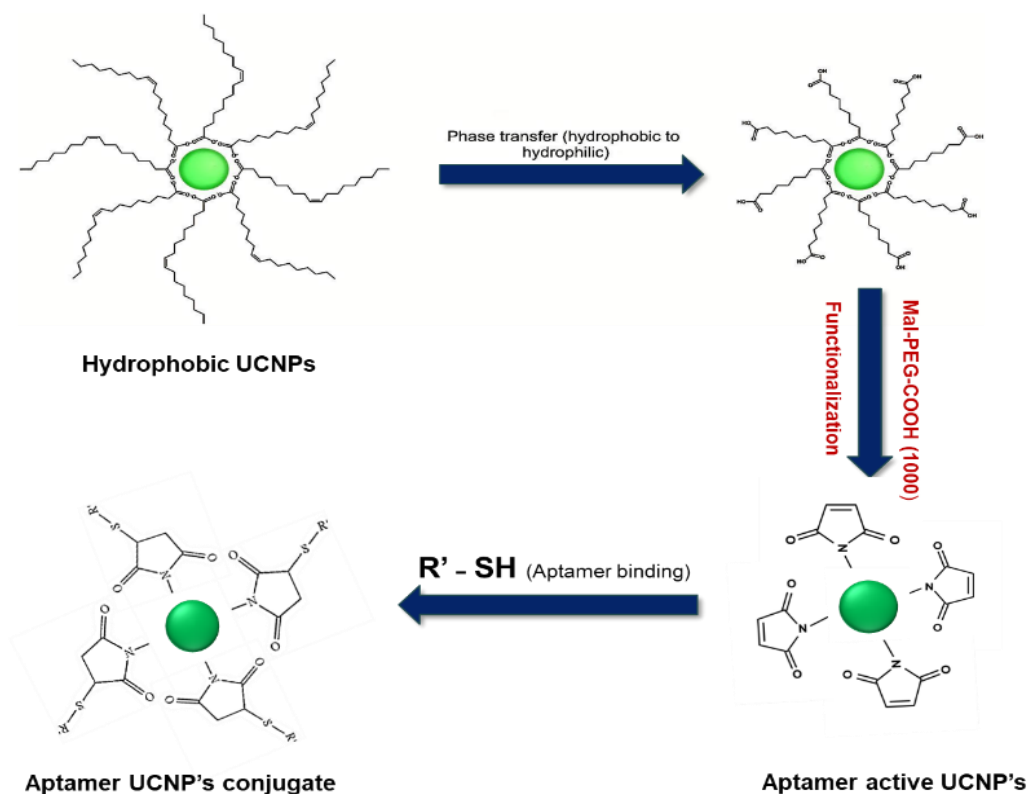


Figure 3-1: Ligand Exchange and bioconjugation: Schematic of the phase of oleic acid-capped upconverting nanoparticle, Functionalization of the surface of UCNP's with maleimide group by ligand exchange method and subsequently conjugation with thiol aptamer

Table 5. DNA oligonucleotides (aptamers) used in this study are provided

Aptamers	Sequence
Primary aptamer	5'-Biotin- CGTACGGAATTCGCTAGCTGATGGTGTG GCGGGGGCGGCCTGGGGCGGGCCGCCGATGGGATCCGAGC TCCACGTG-3'
Secondary aptamer	5'- Thiolated -CGTACGGAATTCGCTAGCGGTGGC TCTAGGGCCTATCGTTGCGCCGACGGATCCGAGCTCCACGT G-3'
Complementary sequence of secondary aptamer	5'- Biotin - CAC GTG GAG CTC GGA TCC GTC GGC GCA ACG ATA GGC CCT AGA GCC ACC GCT AGC GAA TTC CGT ACG -3'.

3.1.4. Lateral flow strip

A lateral flow strip consists of three main overlapping pads assembled on a laminating/baking card as support. The sample application pad was made of cellulose fiber (CFSP203000, 20 × 300 mm). The UCNPs-aptamer (detection probe) conjugate solution was dispensed on the glass fiber conjugate pad through microliter pipette. To aid the immobilization of biotin-capture primary aptamer and biotin-capture control aptamer probes, streptavidin (0.5 mg ml^{-1} , 30 μl) was dispensed on a test line and control line before dispensing the aptamers solutions, to react with and form stable conjugates, incubated for 1 h at 4 °C. Aptamer solutions were dispensed on NC membrane to form the test and control line. After dispensing, the conjugate and cellulose membranes were dried at 37 °C for 2 h before assembly. 0.5–1% trehalose was added to the striping solution to increase the stability of the protein binding on the membrane. Test and control lines are 1 mm wide and 5 mm apart as shown in Fig. 3-2. The minimum overlapping distance between the sample and conjugate pad was kept to avoid developing dead space, which then serves as a reservoir for slower conjugate release. Subsequently, PBS buffer containing BSA ($50 \text{ }\mu\text{gml}^{-1}$) was run through the membrane to reduce the matrix interpretation and increase the signal-to-noise (S/N) ratio through blocking. To assemble on the laminate baking card (ordered from DCN), the nitrocellulose was applied first, followed by the conjugate pad, wicking pad, and then sample pad. The control line exhibited successfully captured Vaspin free aptamer conjugate, showing that the reaction conditions and assay worked fine.

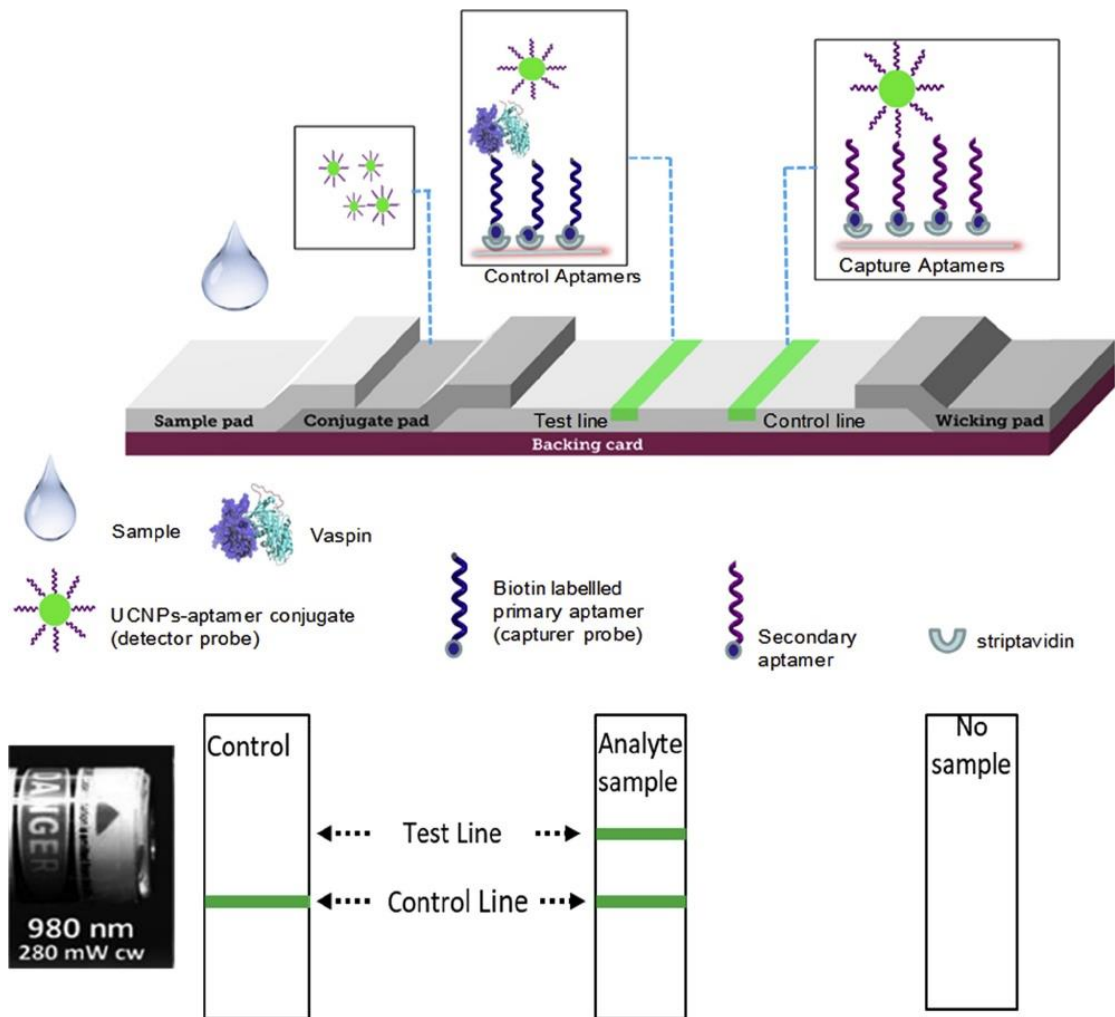


Figure 3-2: Schematic illustration of the configuration of the UCNPs based lateral flow vaspin sensor and principle of qualitative detection of vaspin on the fluorescent upconverting nanoparticles based lateral flow biosensor.

3.1.5. Sample assay

Under the optimized experimental conditions, the performance of the UCNPs LFSA was evaluated with different concentrations of target Vaspin in the running buffer, PBS (pH~7.0) + 0.5% BSA. In a typical assay, 50 μ l of the sample solution was introduced to the sample pad as shown in Fig. 3-18; the solution then migrated towards the absorption pad by the capillary force. The fluorescence images of the test zone and control zone were evaluated visually under near-infrared CW (continuous wave) laser diode (980 nm) which gives fluorescence in the visible range. The smartphone was located on a self-made detector holder and images were collected

in a dark box to avoid the effect from surrounding light for quantitative analysis. The fluorescent intensities of the test line and control line were recorded by using the mobile phone camera to calculate RGB values through a colorimetric app as shown in Fig. 3-3. Only the change in intensity of the green coordinate was considered on the test line to translate the amount of analyte into a detectable changing entity. The ability of the sensor was tested for the target Vaspin in buffer samples. A variety of known concentrated samples were prepared and tested. A linear calibration curve was obtained for the intensity of green color coordinate vs the quantity of known analyte present in the sample. The system was then tested to calculate three known concentrations of Vaspin in independent samples within the clinical range, solely using the calibration curve and the fluorescence intensity.

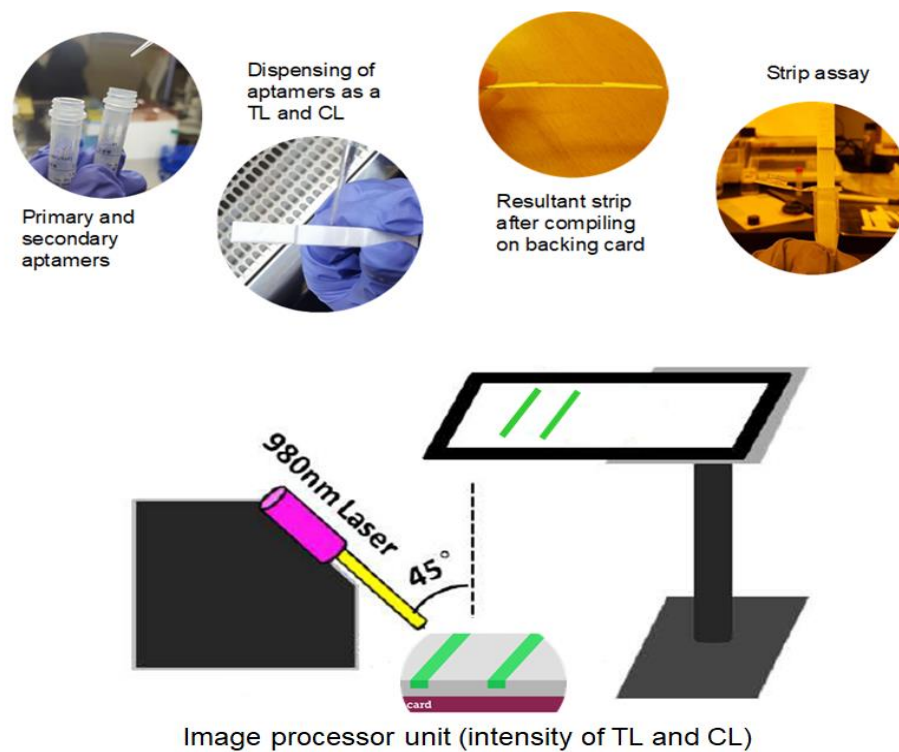


Figure 3-3: Steps of strip fabrication and evaluation: Typical diagram for calculating RGB of test line when excited in NIR (980 nm) for recording the concentration of Vaspin using high-resolution camera

3.1.6. Characterizations of conjugated nanoparticles

The fluorescent properties were tested using photoluminescence spectroscopy to approve that the excitation/emission wavelength remains unaffected. Fig. 3-4(a) shows the Gaussian fitting and photoluminescence (PL) emission spectra of UCNPs. It shows the deconvoluted peaks at different wavelengths, at 550 nm (green line) indicating the emission of green fluorescence when excited under a CW laser of 980 nm. The other related peaks were also observed which might be associated with the change in lattice strain after reduction of particle size. The overall color output appears green which dominates the red emission. The results were further cemented by exciting a liquid sample of the nanoparticles under a near-infrared (NIR) 980 nm laser excitation source of power 30 mW. Fig. 3-4(b) shows the image of the visible green emission. 1 μm size particles were grounded to get nanometer-size particles; they were characterized using TEM to confirm the particle size reduction. Fig. 3-4(c) shows the reduced particles of oleic acid capped NaYF₄: 20 mol% Yb, 2 mol% Er. They have an average size under 100 nm and a quantum yield of 3%. DLS (Dynamic light scattering) measurement has also shown in Fig. 3-4(d). XPS (x-ray photoelectron spectroscopy) measurement of UCNPs has shown in Fig. 3-5.

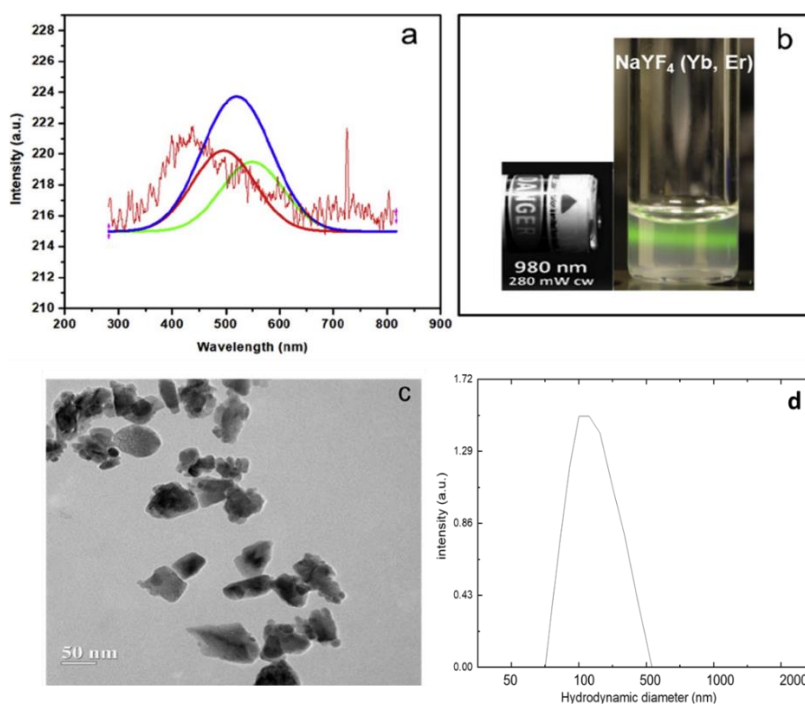


Figure 3-4: (a) Photoluminescence spectroscopy of the colloidal solution of the UCNPs under excitation wavelength of 980 nm (b) Fluorescence of nanoparticles colloidal solution (5 mg ml^{-1}) (c) TEM images of NaYF_4 (Yb: Er) nanoparticles (d) Dynamic light scattering of the colloidal UCNPs with an average hydrodynamic diameter of around 100 nm

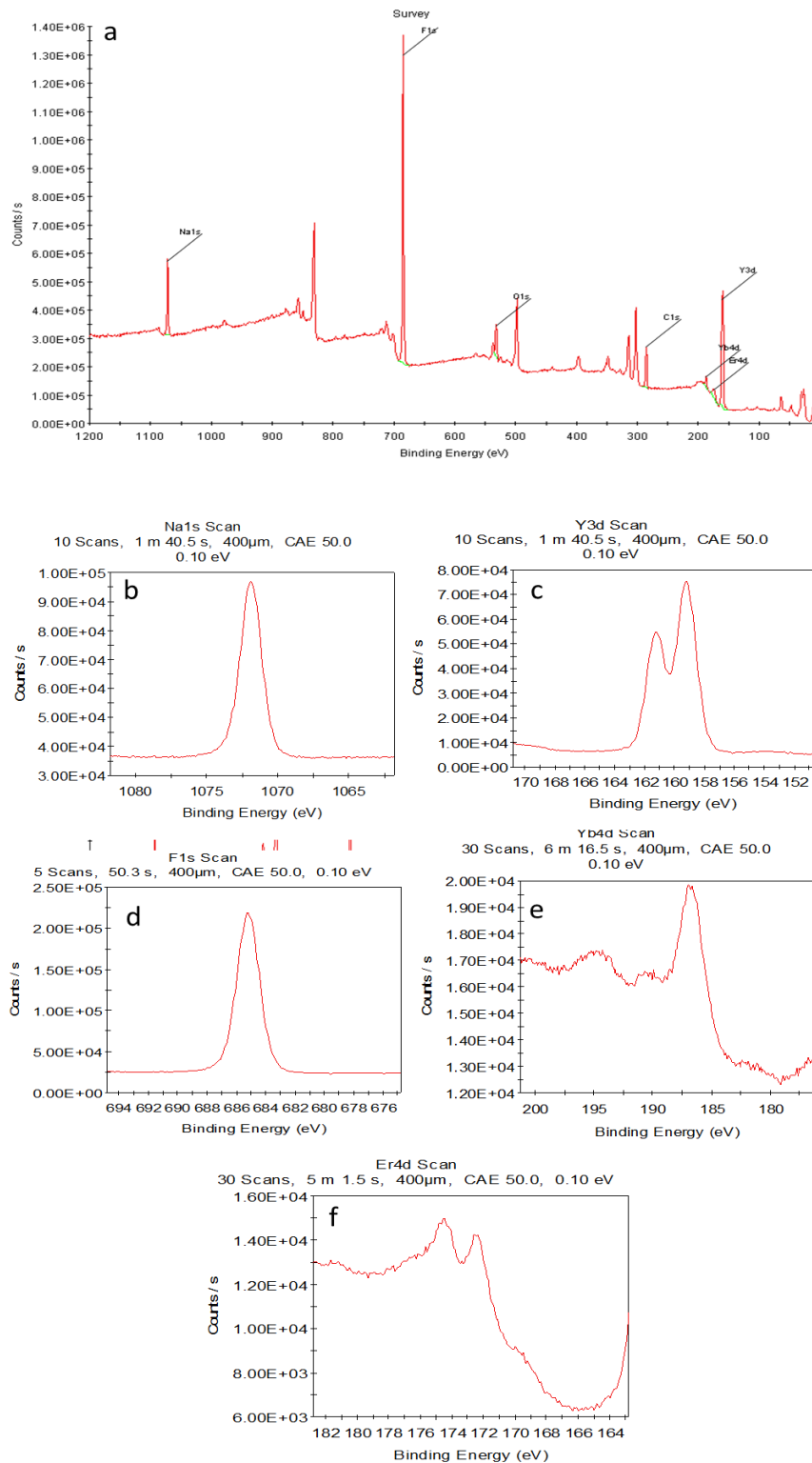


Figure 3-5: X ray photoelectron spectroscopy (XPS) (a) Survey, (b) Na 1s, (c) Y 3d, (d) F 1s, (e) Yb 4d and (f) Er 4d.

Raman spectroscopy was used to detect the maleimide group indirectly because the peak for maleimide was indistinct in the whole spectrum. The surface of nanoparticles was modified by ligand exchange process using PEG; the ether group (R-O-R) is responsible for it which has asymmetric stretching vibration in the range of 800–920 cm^{-1} that can be confirmed from Fig. 3-6(b) having peaked at 793, 880 and 926 cm^{-1} respectively ¹¹⁰. These peaks are usually absent for the UC control and modified nanoparticles using the salinization method. Therefore, usually, the Raman spectra of UCNPs@SiO₂-PEG-Mal, and UCNP@SiO₂ contains no PEG and hence serves as a control in the region between 700 and 1000 cm^{-1} . UCNPs@Mal-PEG show specific Raman bands with a maximum of 850 cm^{-1} or 855 cm^{-1} subsequently, which can be accredited to the symmetric stretching vibrations of the PEG ether group (R-O-R) on the UCNPs surface. This Raman band is absent in UCNP@SiO₂ without PEG-modification ¹¹¹. It concludes that oleic acid capped nanoparticles were successfully converted to the maleimide functional group by PEG. The complete Raman spectrum from 100 to 1000 cm^{-1} is presented in Fig. 3-6(c) which confirms that the surface of oleic acid capped nanoparticles has been exchanged by the maleimide group through the ligand exchange process as there are no stretching vibrations between 200 and 400 cm^{-1} . For control of characterized unmodified UCNPs spectrum band has been shown in Fig. 3-6(a).

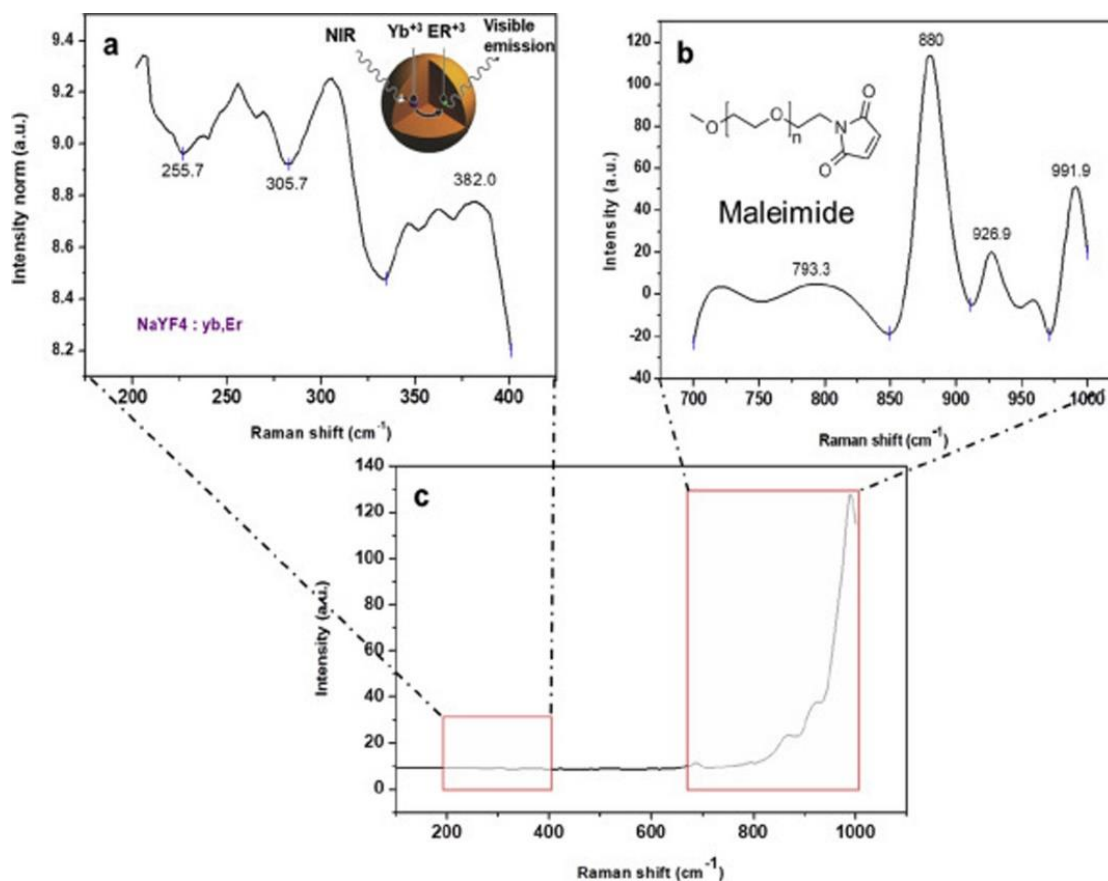


Figure 3-6: Raman spectra of UCNPs **(a)** Spectra of 100 nm unmodified upconverting nanoparticles NaYF₄ (Yb: Er) **(b)** UCNPs@Mal-PEG-COOH modified particles showing the characteristics stretching of ether group (R-O-R) between 800 and 920 cm⁻¹ **(c)** Complete Raman spectrum of the functionalized particles.

Bioconjugation (Coating of thiol functional secondary aptamer onto the surface of maleimide functionalized UCNPs) was further verified by FT-IR analysis. Binding of the thiol group of the aptamer with maleimide functionalized UCNPs was made sure as shown in Fig. 3-7 that could also be used to analyze the stability. In the case of OA capped UCNPs the bands at 1454 and 1546 cm⁻¹ accredited to the asymmetric (uas) and symmetric (us) stretching vibrations of the –COOH- group of oleic acid. The transmission bands at around 2848 and 2924 cm⁻¹ are attributed to the asymmetric and symmetric stretching vibrations of C–H in the alkyl chain from an oleic acid molecule, and the band at around 3426 cm⁻¹ attributed to = C–H– stretching vibration in the prepared sample. In the same manner, after the conjugation of OA capped nanoparticles can be confirmed either by the appearance of new absorption bands in the IR spectra. Here the main

concerned band is 1646 cm^{-1} . The main bond of concern here is the thioether bond, which owes to the covalent bond between the maleimide functional group of nanoparticles and thiol group of the aptamer and the typical signal arises at 1646 cm^{-1} made sure the bioconjugation. These observations show an indication of the successful fabrication of bioconjugation.

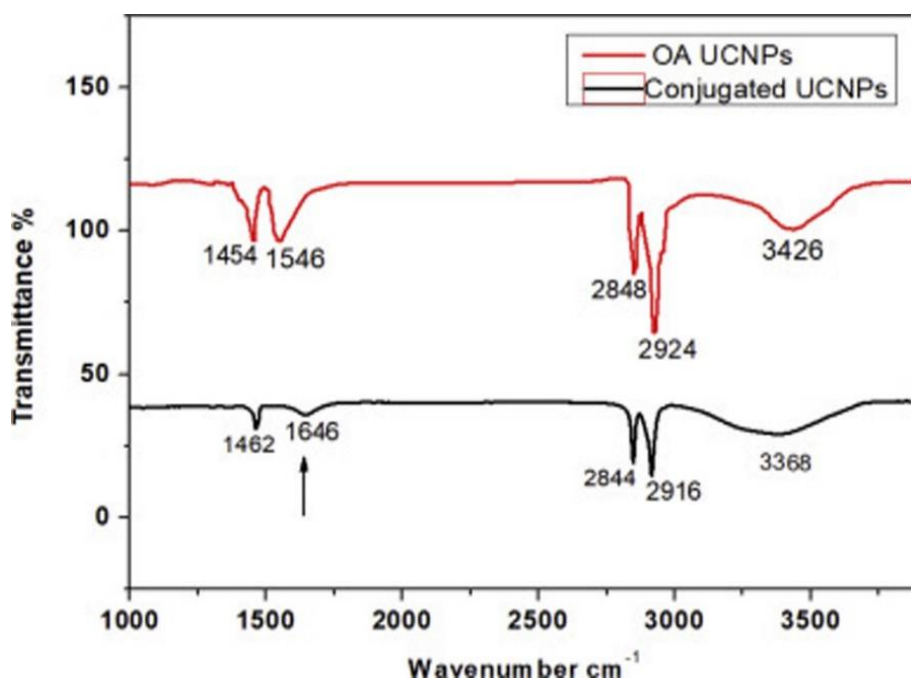


Figure 3-7 FTIR spectrum of the aptamer-UCNPs conjugate: different peak positions confirming the presence of upconverting nanoparticles ($\text{NaYF}_4: \text{Yb, Er}$) and oligomers (Aptamers)

3.1.7. Vaspin detection using LFSA strip in buffer samples

Under the optimized experimental conditions, the performance of LFSA was tested in the presence of different target vaspin concentrations. The captured vaspin on the test line was observed visually under NIR and the fluorescence intensity of the test line was measured to quantify the target concentration. A series of the increased intensity test zones were observed with increasing target Vaspin concentrations indicating the good reliability of the strip within suitable concentration ranges. The resulting curve of the target Vaspin versus the fluorescence intensity was almost linear over a range of $0.1\text{--}55\text{ ng ml}^{-1}$ with a detection limit of 39 pg ml^{-1} and $R^2 = 0.9886$ as shown in Fig.3-8. The assay time is around 2–3 min. The detection limit of UCNPs

conjugate in this report is 16 times greater than that of AuNPs based detection of Vaspin (LOD = 0.137 nM) without signal amplification. The benefits of the proposed method in this report include: lower cost than the AuNPs, low limit of detection, highly repeatable results, high stability due to covalent linkages, and reproducibility along with quantitative results. The sample glided from the sample pad through the cellulose membrane towards the wicking pad (to absorb the matrix in the sample). As shown in Fig. 3-2, the signal could be observed only in the presence of Vaspin. The amount of aptamer-UCNPs conjugate must be higher enough than the amount of aptamers on the test line and control line. In this study, the amount of conjugate was calculated to be greater than the highest concentration of Vaspin (55 ngml^{-1}) which is much higher than the normal concentration in the human blood ($0.1\text{--}7 \text{ ngml}^{-1}$). Therefore, it should be shared with both the test and control line. The saturation of the test line occurred after 55 ngml^{-1} and the linear range leads to constant observation.

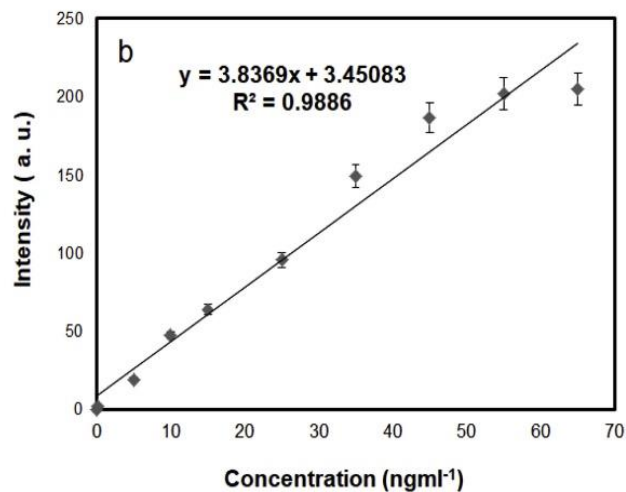
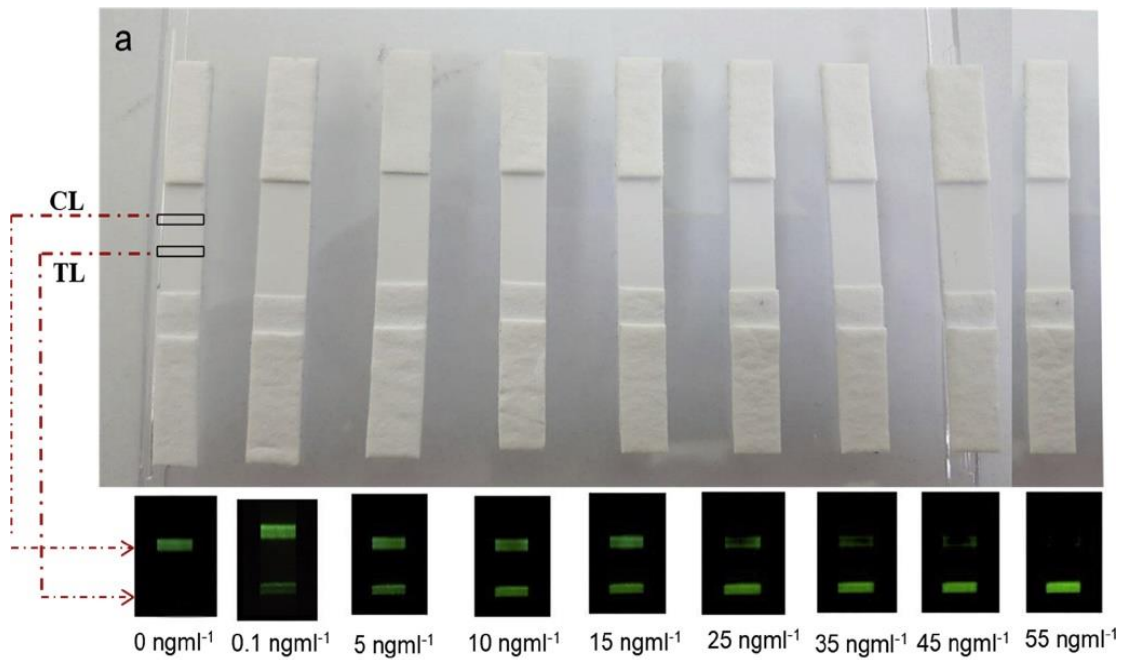


Figure 3-8: Analysis of LFSA **(a)** Images of the sensor with different concentrations of target Vaspin under the optimal experimental conditions and **(b)** Calibration curve of test line intensity versus Vaspin concentration. Error bars represent standard deviation, $n = 3$.

3.1.8. Application: Vaspin detection in serum samples

To examine the practicality of the proposed assay in real samples, the applicability and anti-interference ability of target Vaspin in spiked human serum samples which are a complex biological fluid containing a variety of matrices present, using the proposed method was studied.

In this study, three known concentrations of target Vaspin (0.2 , 5 , and 7 ng ml^{-1}) were spiked in

human serum samples and evaluated 3 times each concentration for the reproducibility of the biosensor. The serum samples were diluted to 3.5% PBS. The same concentrations and the fluorescence intensities of test line were measured. The system returns values within ranges of 98%, 101%, and 96% of the known amounts for 0.2, 5, and 7 ng ml⁻¹ targets respectively as shown in Fig. 3-9. This indicates a very good reproducibility as shown in Table 6 and a high potential to develop an assay for future clinical applications.

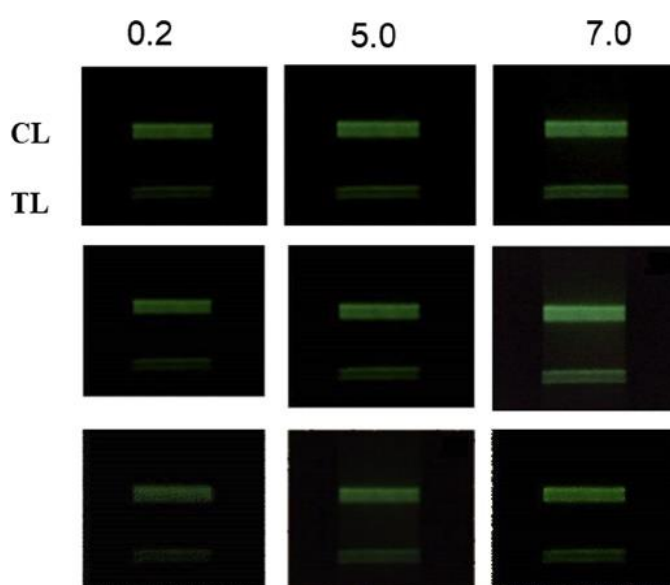


Figure 3-9: Detection of Vaspin spiked in human serum (pH = 7.0) using UC based LFSA, different concentration of vaspin were diluted in serum samples and observed under excitation of 980 nm laser.

Table 6. Recovery results of Vaspin detection in serum (n = 3).

Added concentration (ng ml ⁻¹)	Fluorescence Intensity (a.u.)	Detected concentration (ng ml ⁻¹)	Recovery Ratio (%)
0.2	1.5	0.19 ± 0.21	98.1
5.0	17.8	4.89 ± 0.13	101
7.0	23.1	7.12 ± 0.09	96.9

3.2. Fluorescent dye-based detection of Reactive Oxygen Species (ROS) in a microfluidic chip

3.2.1. Background

Reactive oxygen species (ROS) are referred to as chemical species with a single unpaired electron in an outer orbital, which is extremely unstable; when generated in cells, they spontaneously attack nucleic acids as well as a variety of cellular proteins and lipids^{112, 113}. Free radicals also initiate reactions in which molecules that react with free radicals are themselves converted into other types of free radicals, thereby creating the chain of damage^{114, 115}. ROS are normally produced in a little amount in all cells during the reduction-oxidation (redox) reactions that take place during mitochondrial respiration and energy generation¹¹⁶. Common ROS consist of superoxide (O_2^-), hydrogen peroxide (H_2O_2), peroxynitrite ($ONOO^-$), reactive aldehydes, nitric oxide (NO), and other hydroxyl radicals^{117, 118}. In this process, molecular oxygen is sequentially reduced in mitochondria by the addition of four electrons to synthesize water. This reaction is imperfect; however, small amounts of highly reactive but short-lived toxic intermediate metabolites are generated when oxygen is only partially reduced. These intermediates are consist of superoxide (O_2^-), which is converted to hydrogen peroxide (H_2O_2), spontaneously and by the action of the enzyme superoxide dismutase. H_2O_2 is more stable than O_2^- and can readily pass through biological membranes. In the presence of metals, such as Fe^{2+} , H_2O_2 is converted to the highly reactive hydroxyl radical $\bullet OH$ by the Fenton reaction^{119, 120}. The damage caused by ROS is determined by their rates of production and removal. ROS production leading to a condition called oxidative stress, which induces cell death by apoptosis and necrosis^{121, 122}. Reactive oxygen species cause cell injury by three primary reactions: (1) Lipid peroxidation of membranes, (2) Cross-linking and other changes in proteins, and (3) DNA damage. Such DNA damage has been implicated in cell death, aging, and malignant cancerous transformation of cells¹²³. In addition to the role of ROS in cellular injury and microbial killing, low concentrations of ROS are involved in many signaling pathways in cells and thus in many physiological reactions¹²⁴. Therefore, these molecules are produced normally but, their intracellular concentrations are

tightly regulated in normal cells ^{125, 126}. On the other hand, ROS high at concentration can damage lipids, a cellular protein, and nucleic acid that may stimulate various diseases, while in cancer cells it can be utilized as a proapoptotic agent ¹²⁷. ROS detection is important to examine in the assessment of different drugs and compounds and has been considered as a marker for cell cycle progression ^{128, 129}. Thus, the level of ROS conveys about the cell state, while the overproduction can envisage the outcome of the cell ¹³⁰. A variety of techniques have been used to detect ROS, including electron spin resonance, electrochemical and fluorescent signaling ¹¹⁴. The colorimetric substrate can also be used to detect ROS or specifically H₂O₂ but it is less sensitive than the fluorescent-based detection ¹³¹. Fluorescent based detection is based on using the fluorescence probe, here 2'-7' dichlorofluorescein (H2DCF) to 2'-7' dichlorofluorescein (DCF) has been used as a fluorescent probe for the detection of H₂O₂ because it does not affect cell metabolism/viability along with high sensitivity, simplicity, and reproducibility ¹³². Thus far, common ROS-detecting techniques identify oxidative stress events but are endpoint and qualitative [25,26]. Similarly, another study has been reported the monitoring of ROS using M-H2DCFDA and HyPer probe as described to detect the fluorescence in fibroblast for 30 min ^{133, 134}. In another approach, ROS production and monitoring have been carried out using phosphorus and nitrogen-doped carbon dots (PN-CDs) as a fluorescent probe in mouse macrophages (RAW264) through confocal imaging for 50 min ¹³⁵. The majority of the studies reported the detection of ROS is the endpoint ¹³⁶. In order to perform continuous detection with precise concentrations measurement, microfluidic chips integrated with fluorescent systems provide an elegant solution ^{137, 138}. In addition to the precise control of the experimental conditions, the advent of 3D printing in microfluidics is providing miniaturization, rapid analysis, and high throughput - deeply significant for biological studies ¹³⁹⁻¹⁴¹. Microfluidic platforms are being efficiently used for cell metabolism studies, drug screening, tissue engineering, organs-on-a-chip, and body-on-a-chip ^{142, 143}. In our previous work a pre-patterned ITO, 3D printed microfluidic chip was developed for TEER (Transpeithelial resistance) impedance measurement in lung cancer cells line [41]. Organ-on-a chip is an

appropriate replacement to improve the consistency of cell-based assay in-vitro preclinical studies, drug discovery and drug development ^{114, 143}.

Detection of ROS is normally used to examine the effect of different kinds of drugs and compounds and is used as a marker for cell cycle progression. In chemotherapeutic amplification in which ROS levels rise, the already increased cancer cells over a threshold lead to cell death and tumor regression. Detection of ROS during and after chemotherapy is crucial to observe. Moreover, ROS can control the response of many important cell-signaling molecules comprising mitogen-activated protein kinases, nuclear factor-kB, tumor suppressor protein p53, and other cell cycle checkpoint proteins. As per our knowledge, real-time monitoring and detection of ROS have not been reported yet for a prolonged period in a microfluidic chip along with an in-house built dedicated fluorescence microscope. This microscope led to continuously monitor ROS in MCF-7 cells, and beneficial for cells handling which avoids removing the chip from the incubator, contamination, and introduction of bubbles. On-chip imaging methods are highly required, particularly in the fields of automated chip systems for high-throughput biological applications. Using on-chip fluorescence microscopic imaging and a microfluidic chip platform offers a system with ease of handling and fully automated system control to detect cellular activity. Real-time monitoring of ROS production has been evaluated using a fluorescence probe (DCFDA) and examined under the in-house built fluorescence microscope. A glass-based microfluidic chip was used to develop a monolayer of MCF-7 at the bottom plate and maintained a developing layer in RPMI in a 37 °C incubator with 5% CO₂. Glass based chip allows optical examination of the cells [46] and avoid small molecular absorption unlike PDMS [47]. In this report for the first time, an automated system using microfluidic technology has been utilized for ROS detection, which aims to overcome the limitations of the conventional method used. The development of this real-time intracellular ROS detection would provide a platform for the assessment of cell cycle progression and evaluation of the variety of drugs.

3.2.2. Optimization of concentration and mechanism of dye interaction with cells

The concentration of DCFDA was optimized by loading different concentrations of dye in the chambered cell culture slide. MCF-7 cells (150,000) were added in each compartment and incubated at 37 °C in 5% CO₂ in the dark. Cells were incubated in the chamber for 24 h to allow adherence. Cells were washed with 1× warm phosphate-buffered saline (PBS) and then exposed to the 700 μl of 5, 10, 25, and 50 μM DCFDA concentrations and incubated again in the dark for 45 min at 37°C and 5% CO₂. DCFDA diffuses into the cells, the acetyl groups (C₂H₃O) on DCFDA are cleaved by intracellular esterase to produce the non-fluorescent compound (H₂DCF) which is promptly oxidized to highly fluorescent 2',7'-Dichlorodihydrofluorescein by ROS as depicted in Fig. 3-10. So the DCFDA was removed and the cells were exposed to phenol red-free RPMI supplemented with 10% (v/v) FBS. The fluorescence of the MCF-7 cells was examined under confocal microscopy (model #FV1200; Olympus, Japan) at 10× resolution and analyzed the fluorescence of different concentrations.

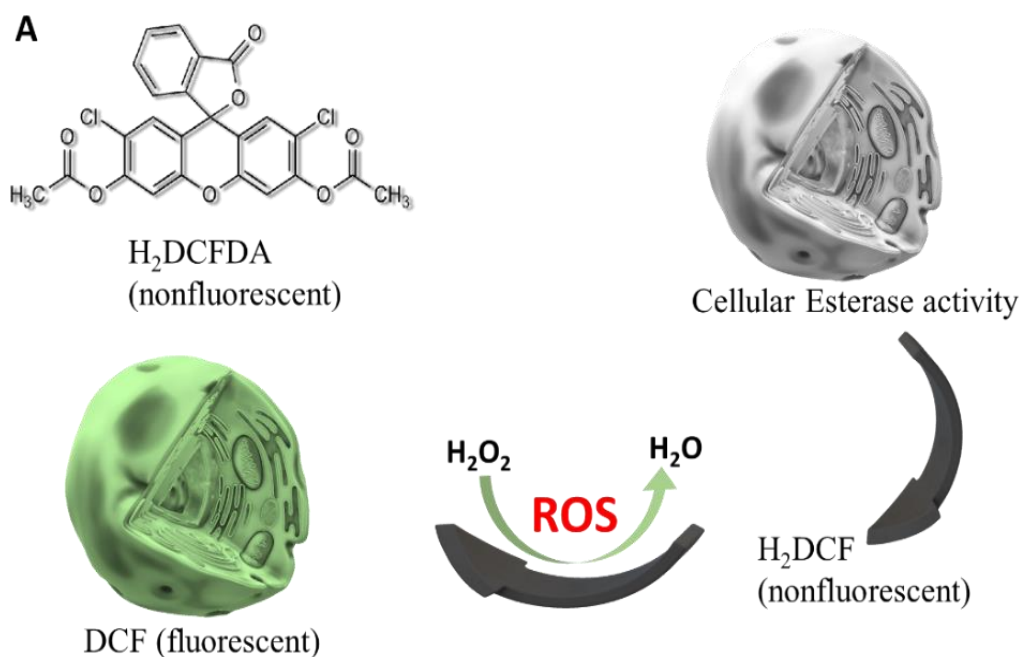


Figure 3-10: Schematic illustration of the generally accepted mechanism of interaction of DCFDA with ROS in cells

3.2.3. Microfluidic chip

The printed channel is 300 μm in height and 3.4 mm in width. The microfluidic channel was printed on the lower side of the top glass, while the microfluidic connectors were attached on the upper side of the top glass to provide fluidic connection as depicted in Fig. 3-11(a) and in Fig. 3-11(b) cross-sectional view of the chip is shown. A 3D-printed chip holder was designed to hold the top and bottom glasses together as shown in Fig. 3-11(d).

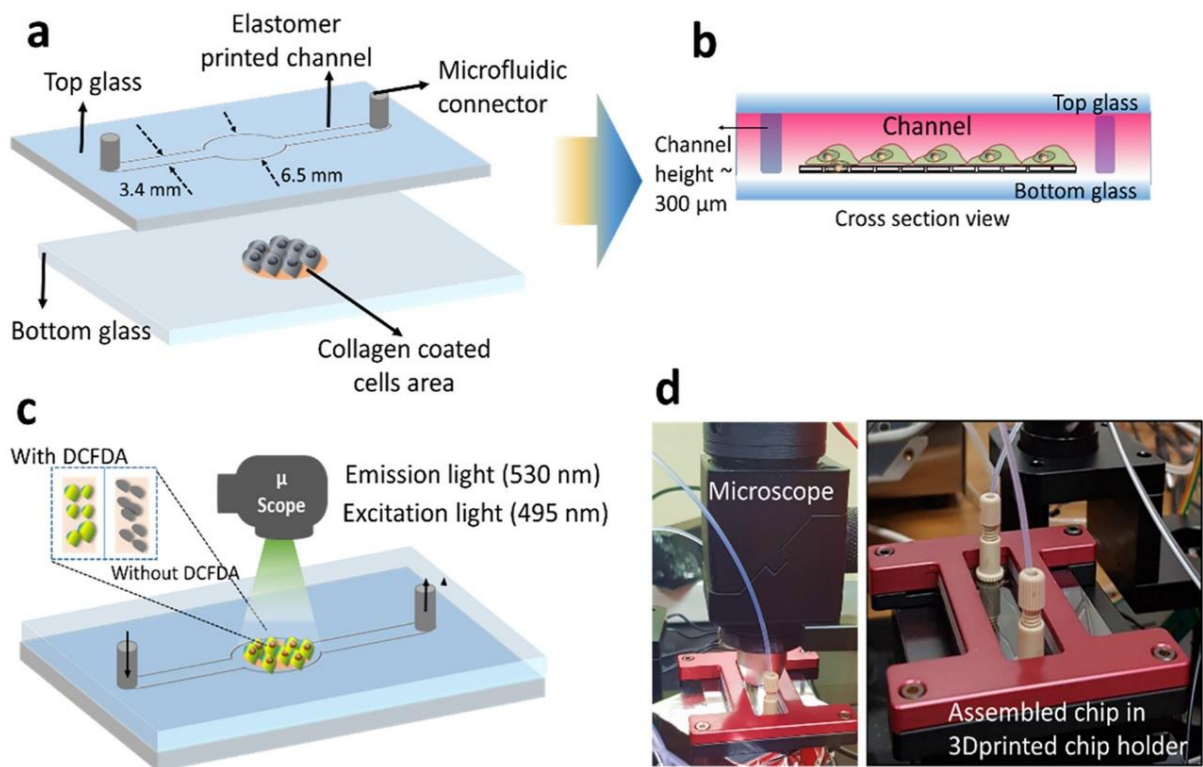


Figure 3-11: Microfluidic chip. (a) Top and bottom glass (b) Full chip configuration; cell culture on bottom glass, schematic view of cross-section (c) assembled chip with the microscope (d) 3D printed microscope and assembled microfluidic chip in a 3D printed chip holder (original images).

3.2.4. Cell culture on a microfluidic chip

The breast cancer cell line MCF-7 (Michigan Cancer Foundation-7) contains isolated epithelial cells from a pleural effusion from a 69 years old Caucasian female patient with metastatic mammary carcinoma. Cells were cultivated in cell culture flasks with Dulbecco's Modified Eagle Medium supplemented with 10% fetal bovine serum and 1% penicillin/streptomycin. Cultures were maintained at 37 °C in a humidified atmosphere of 5% CO₂. For the experiments, cells were collected by trypsinization, centrifugation and finally re-cultured, harvested with the density of 1.5×10^5 cells on an ECM coated bottom glass slide through cell seeding kit and maintained it at 37°C in a humidified atmosphere of 5% CO₂ incubator for further 24 h to allow adherence. Luna cells counting slide was used for cell counting. Cells on the bottom glass chip slide were washed with 1× warm phosphate-buffered saline (PBS) and 300 μl of DCFDA (50 mM) solution was added to the cells to induce it for 45 min at 37°C in a humidified 5% CO₂ incubator in the dark. The DCFDA solution was removed and again the cells were washed with PBS and the top glass was assembled with the bottom glass and held together in the chip holder. The microfluidic connection was made and the peristaltic pump was turned on to run the media at 60 μl/min to provide a continuous supply for the duration of the experiments as shown in Fig. 3-12.

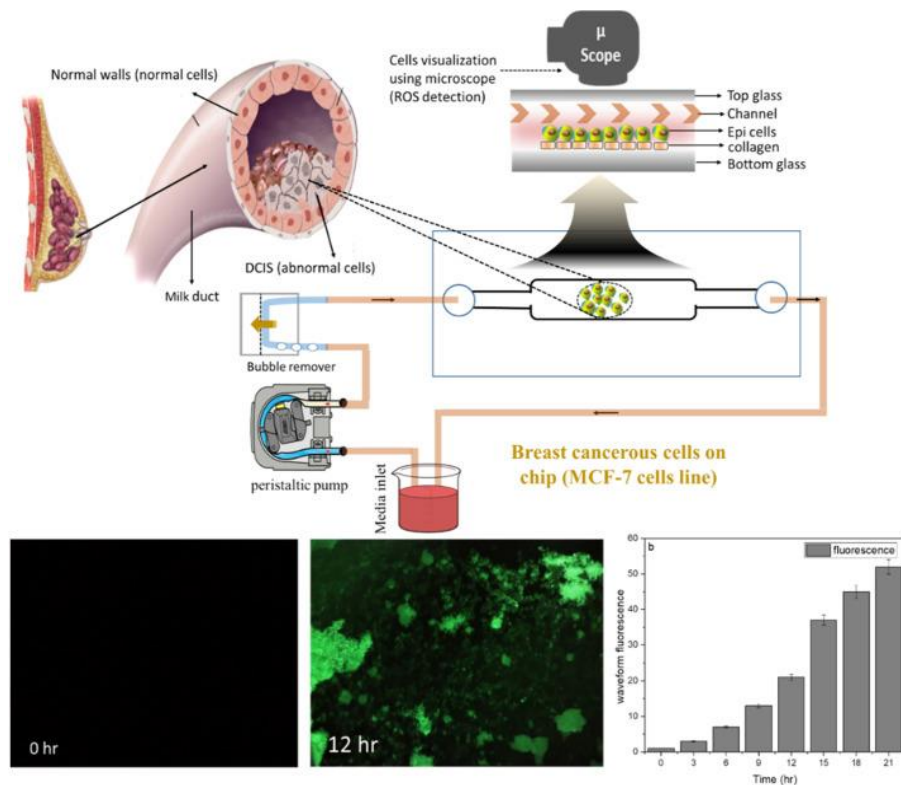


Figure 3-12: MCF-7 cells on-chip for the real-time detection of intracellular reactive oxygen species, a complete setup of the platform including microfluidic chip, media reservoir, peristaltic pump, bubble remover, and fluorescence microscope

3.2.5. In-house built fluorescence microscope

For on-chip fluorescence-based ROS detection, an in-house 3D printed built digital portable fluorescence type microscope was used. The microscope 3D assembly was designed in a typical fluorescence setup housing optical green fluorescence protein (GFP) filter set (Excitation: 479 ± 17.5 nm, Reflection/Transmission: 452–490 nm/505–800 nm, Emission: 525 ± 19.5 nm). A white LED light source was used and filtered by excitation filter into blue excitation wavelength for incidence with help of reflection property of the dichroic mirror. Once the blue light was incident on the sample culture the green wavelength fluorescence was emitted through an emission filter to a sCMOS digital microscope camera which was connected to the PC software via a USB cable. ToupView software was used to record images after repeated intervals of time. The infinity plan achromat 10× biological microscopic lens was used to obtain magnified images of the ROS tagged breast cancer cells set at a working distance of 5.82 mm from the sample. The microscope was made totally plug and play by attaching an LED light source directly to the camera USB cable. Toup view software was used to capture images of the cells. Printed mold images of the microscope have been shown along with microscope detail in Table 7.

Table 7. Microscope specifications

Microscope type	Fluorescence-based
Magnification power	10X
Light source	White LED
Camera	sCMOS series USB2.0 eyepiece camera
Software	ToupView camera control
Chip size (L×W)	56×41 mm

3.2.6. Image processing

To extract the required information from the captured images, LabVIEW 2019 was used along with its high-performance image analysis and IMAQ Vision tools.

3.2.7. Results and Discussion

MCF-7 cells response after exposure to DCFDA concentrations range

A range of DCFDA concentration (0–50 μM) was analyzed to check the fluorescence and cell viability. In the absence of DCFDA, the MCF-7 cells did not show fluorescence in RPMI media while fluorescence values after 45 min incubation with DCFDA were considerably higher in cells loaded with 50 μM DCFDA (45 ± 1.9 RFU per compartment) than in cells loaded with 5–25 μM DCFDA as shown in Fig. 3-13. The laser scanning microscopy (CLSM) was utilized to examine the effect of DCFDA in the cancer cells. In a microfluidic chip, 50 μM DCFDA (700 μl) was used with the same cell density (1.5×10^5) as described in the experimental section and incubated for 45 min and kept in the dark at the same conditions. In the same manner, the addition of 0–10 μM H_2O_2 had no consequential effect on the cell viability as shown in Fig. 3-14. However, exposing the cells to the combination of 10 μM H_2O_2 and 50 μM DCFDA is toxic after 24 hr as the cells number reduced ($109,000 \pm 3000$), confirmed through live/dead assay. Yet, the effect of DCFDA and H_2O_2 on cells viability is not that significant. To obtain the Detection limit/LOD, sensitivity, and detection range, a control experiment performed in chambered cell culture slide, added a range of concentration of H_2O_2 varies from 0 to 10 μM into MCF-7 cells and quantified the fluorescence. A calibration curve is drawn concentration vs. fluorescence as shown in Fig 3-14.

Limit of detection calculation:

$S/N=3$ (this is the rule)

From the plot equation $y = mx + b$ (is obtained by measuring the fluorescence of each image after H_2O_2 concentration)

From the plot

$$Y = 3.77x + 1.2$$

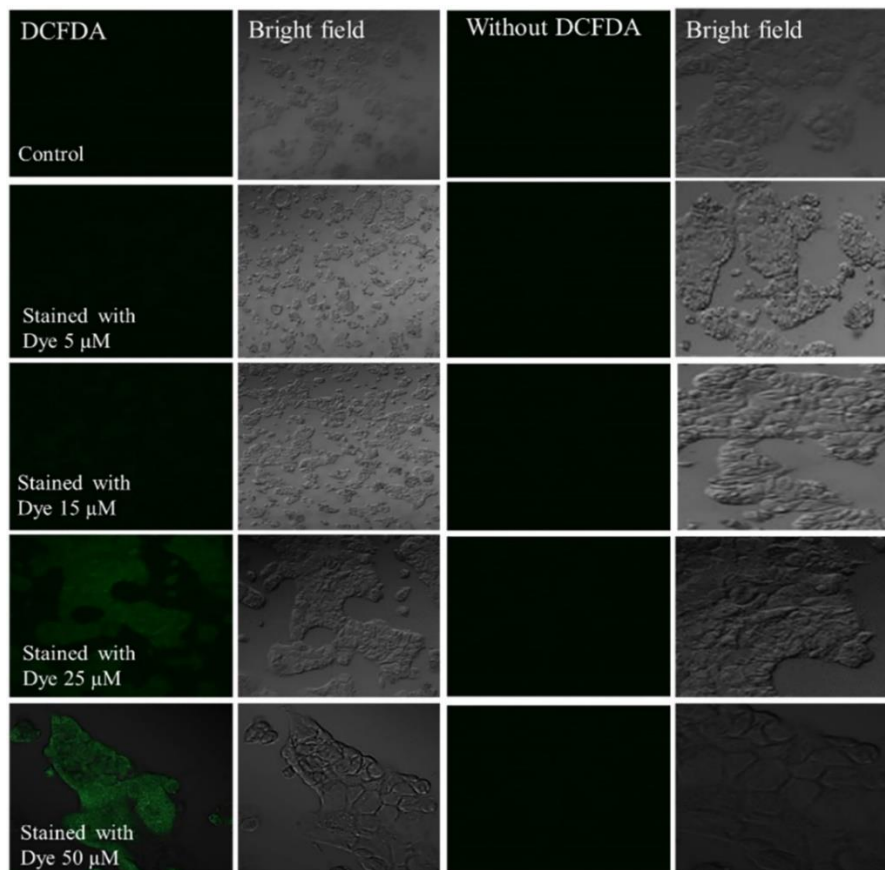
$$S/N=3$$

$$S/N = S/0.51 = 3 \times 0.51 = S = 1.53$$

$$1.53 = 3.77x + 1.2$$

$$0.33 = 3.77x$$

$X = 0.08 \mu\text{M}$ or 80 nM so, [LOD or detection limit is 80 nM]



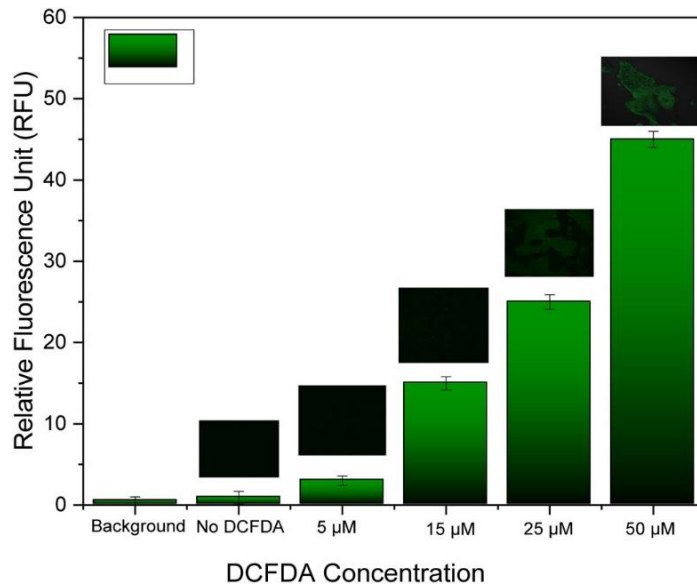
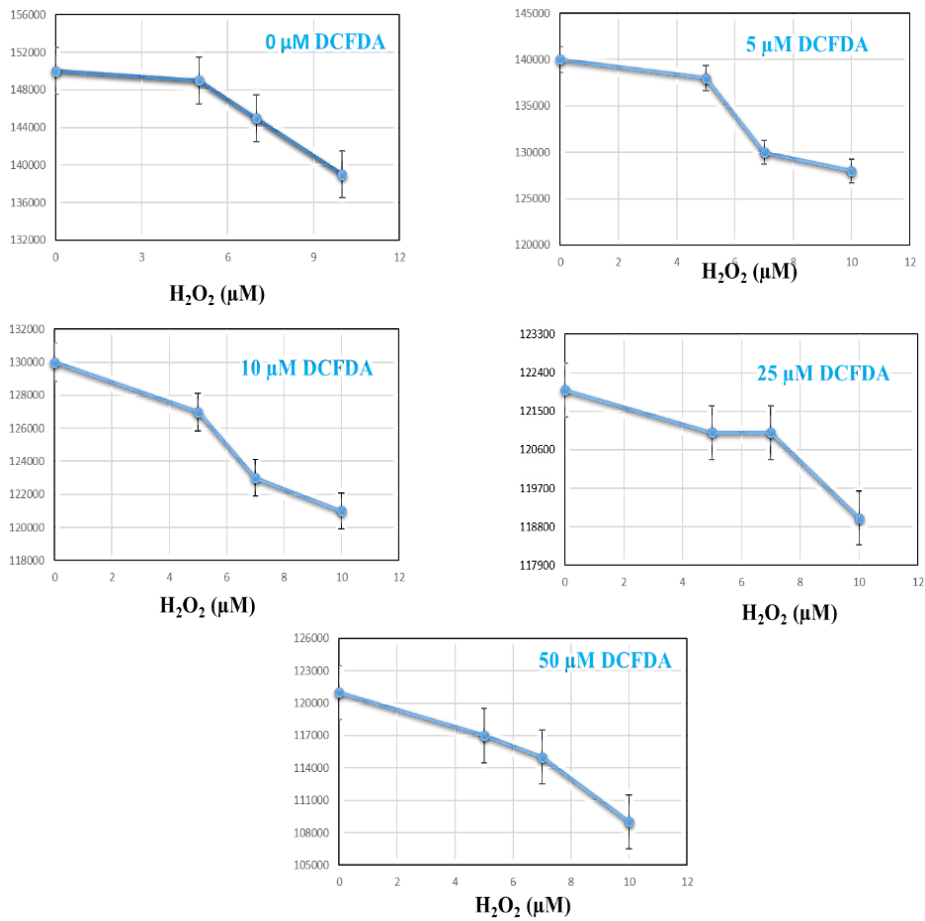


Figure 3-13: Fluorescence microscopy of MCF-7 cells (1.5×10^5). Cells that were cultured and exposed to 700 μl of 0, 5, 15, 25 and 50 μM 2',7'- dichlorofluorescein diacetate (DCFDA) along with background DCFDA fluorescence, also without DCFDA (data presented as mean \pm standard deviation (SD), $n = 3$). Scale bar is 200 μm .



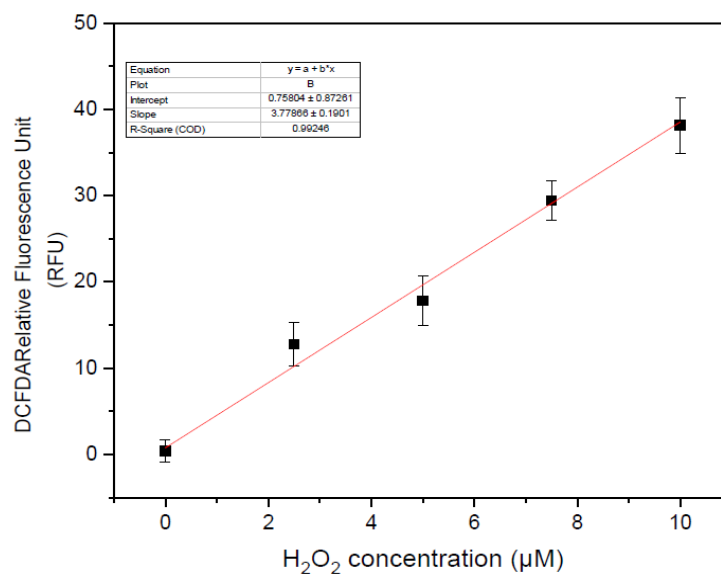


Figure 3-14 Evaluation of DCFDA and H₂O₂ on cells viability. Cells were loaded with 0, 5, 15, 25, and 50 μM DCFDA and then washed and later on exposed to H₂O₂ (0, 5, 7.5, and 10 μM) for 24 h. Fluorescence microscopy was used to observe the cells viability and compared with the standard cell number obtained from Luna cell counter. Means ± SD of 3 independent experiments have been shown. Calibration curve of H₂O₂ concentration vs. fluorescence under the same experimental conditions, mean ± standard deviation (SD), n = 3

MCF-7 cells culture on-chip and cells viability based on Live/Dead Assay

Cells were cultured through cell seeding kit onto the bottom chip to a specific area of pre-coated ECM (4×15 mm) in the chamber zone after passage 3 times. The inverted microscope images of the pre seeding cells and seeded on-chip images (4x, 10x, and 20x) have been shown in Fig. 3-15. After getting 90% confluency, cells were washed with pre-warmed DPBS for the removal of cellular metabolites and cell debris including dead cells. A monolayer has been developed into the ECM layer coated on the bottom glass as shown in Fig. 3-16(b). Followed by the incubation of DCFDA for 45 min. The dye was removed and cells were washed with PBS to remove any esterase enzyme and cell debris. Top and bottom glass were assembled and held in the chip holder, eventually, the chip was connected to the pre-warm RPMI through tubings and a constant flow rate of 60 μl/min was set to run the media. The incubator is connected to CO₂ gas and temperature controller which maintained the cell culture conditions at 5 % CO₂ and 37 °C temperature inside it. Images are shown in Fig.3-16 (c and d) under the observation of a

fluorescence microscope with and without DCFDA. To show the fluid velocity in the microfluidic chip upon the introduction of media, simulations were carried out at a flow rate of 60 $\mu\text{l}/\text{min}$ by COMSOL 5.3. The velocity and pressure profiles are shown in Fig. 3-16(e and f). Live/Dead assays were performed after the completion of the experiment to evaluate the effect of DCFDA which has shown 75% viability after 1 day. The confocal images (Merged, Calcein-AM expression for live cells, and Eth-D for dead cells) were taken on-chip at the end of the experiment after staining with Live/Dead assay reagents as shown in Fig.3-17. The images were analyzed for cell viability quantification using ImageJ software and compare with control (cells counted before seeding using Luna cell counter). For automatic nuclei counting in the separate live and dead images, the ITCN plugin was installed which was considered further for cell viability quantification.

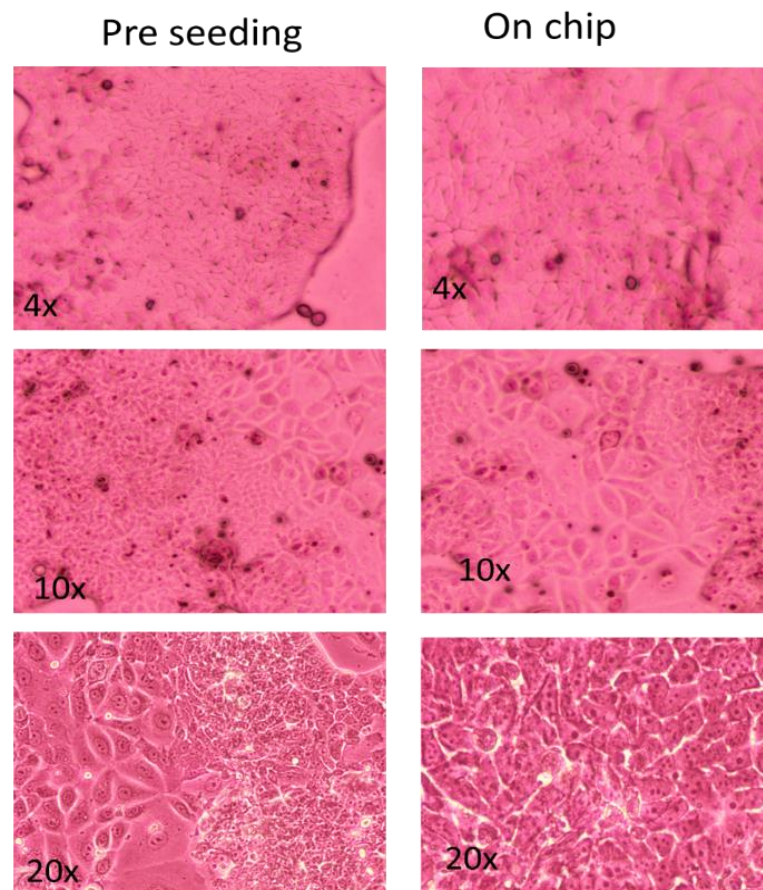


Figure 3-15: Pre seeding inverted microscopic images at different resolution of MCF-7 cells and after seeding them on-chip at the resolution of 4, 10 and 20X

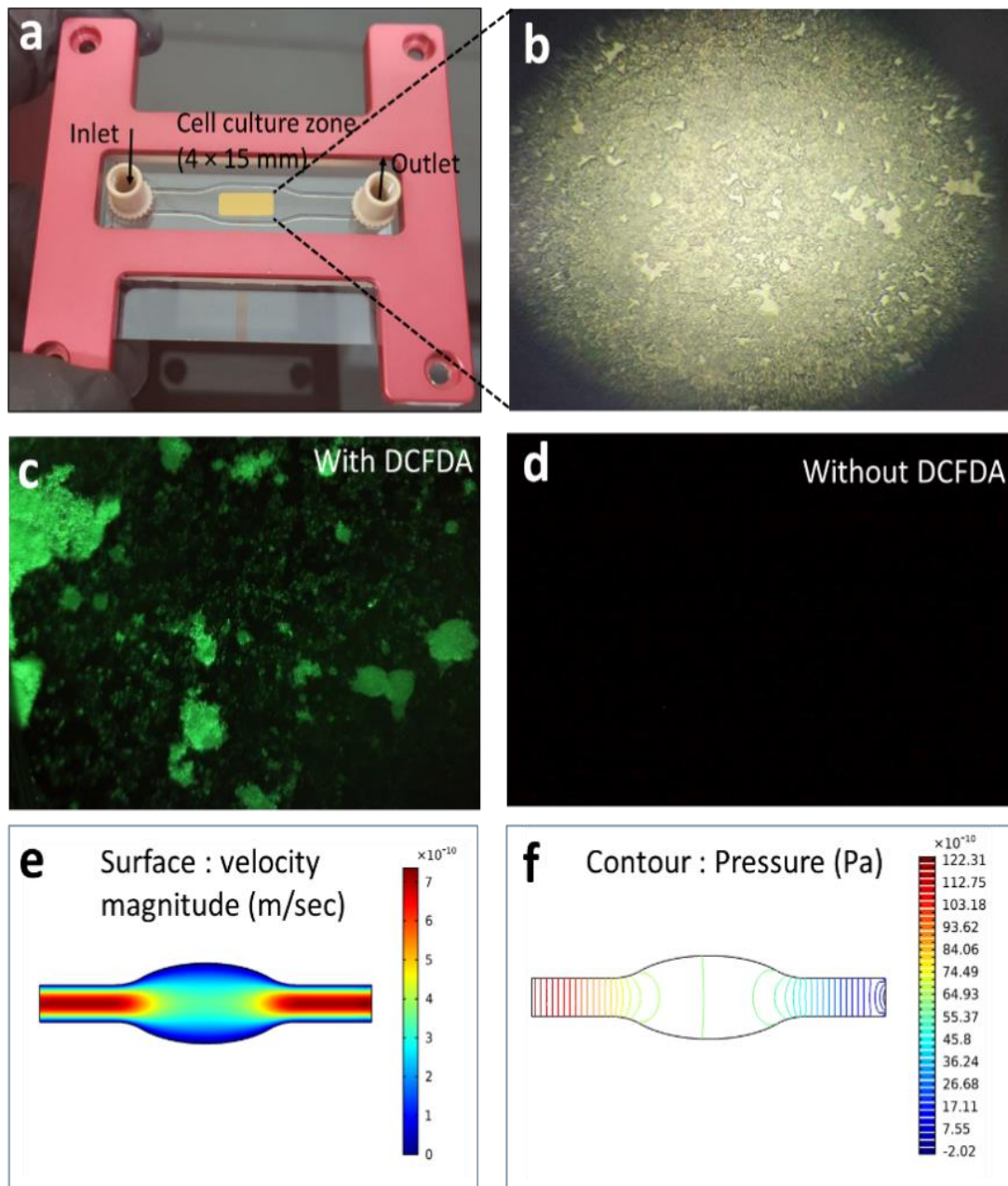


Figure 3-16: Microfluidic chip evaluation **(a)** microfluidic chip showing the cell-cultured area through the custom-built seeding kit, image was taken by inverted microscope **(b)** showing the cell culture area on ECM coated bottom glass through the inverted microscope, scale bar is 100 μm mold **(c, d)** under the fluorescence microscope incubated with and without DCFDA, Scale bar is 100 μm **(e)** Velocity profile and **(f)** Pressure contour of the fluid passing through the microfluidic channel under the flow rate of 60 $\mu\text{l}/\text{min}$

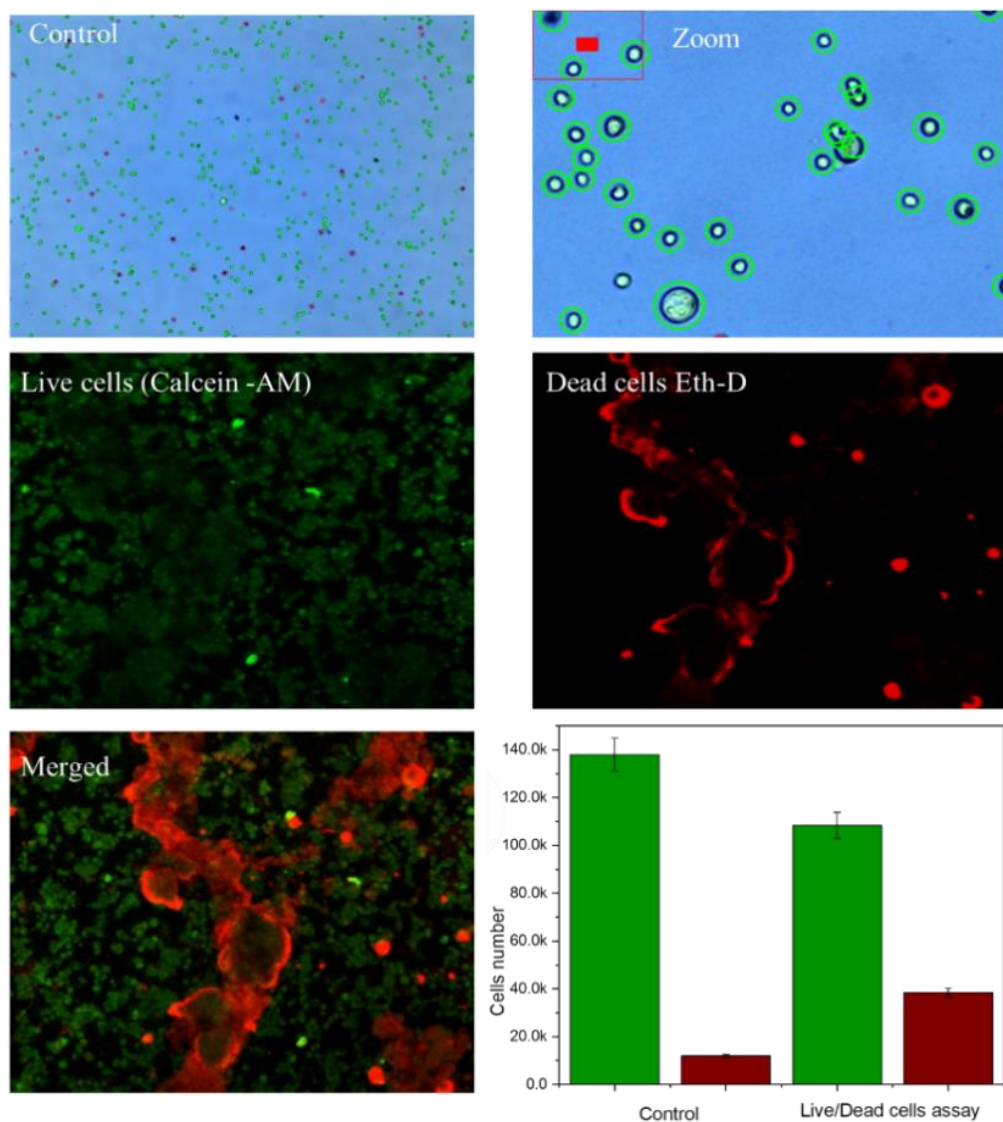


Figure 3-17: MCF-7 Cells viability assay. Cells were exposed to 50 μM DCFDA and then remove after 45 min and followed by the circulation of RPMI for 24 h. Live/Dead assay was performed on the same MCF-7 cells and compared with the control obtained from the Luna cell counter as shown above. Data were subjected to ImageJ software showing the viability of the cells up to 75% after completion of the experiment on a microfluidic chip. Scale bar is 200 μm

3D printed fluorescence microscope

Though, the implementation of a fluorescence microscope is not simple to detect ROS in a microfluidic chip. A 3D printed microscope setup has been developed which was mounted on the top of the chip with a minimum working distance of 5.82 mm. The basic fluorescence microscopy working principle is shown in Fig. 3-18(a) while the 3D CAD model images of our designed portable digital fluorescence microscope have been shown in Fig. 3-18(b) and the exploded view

are shown in Fig. 3-18(c). Both the exploded and assemble views have been detailed for relatability with the original working fluorescence microscopy setup. The distances of the optical filter were selected after consulting the optical filter cube assemblies for commercial microscopes while the lens was infinity-corrected so a certain vertical distance was selected for sCMOS image acquisition digital microscopic camera. Different parts of the whole CAD design were printed in-house with black PLA filament. Creality CR-20 3D Printer was used to fabricate the setup according to design as reported in our previous work also for the fabrication of portable setup. The 3D printed microscope was not only able for fluorescence imaging but also simple microscopic imaging using near lens mounted light source.

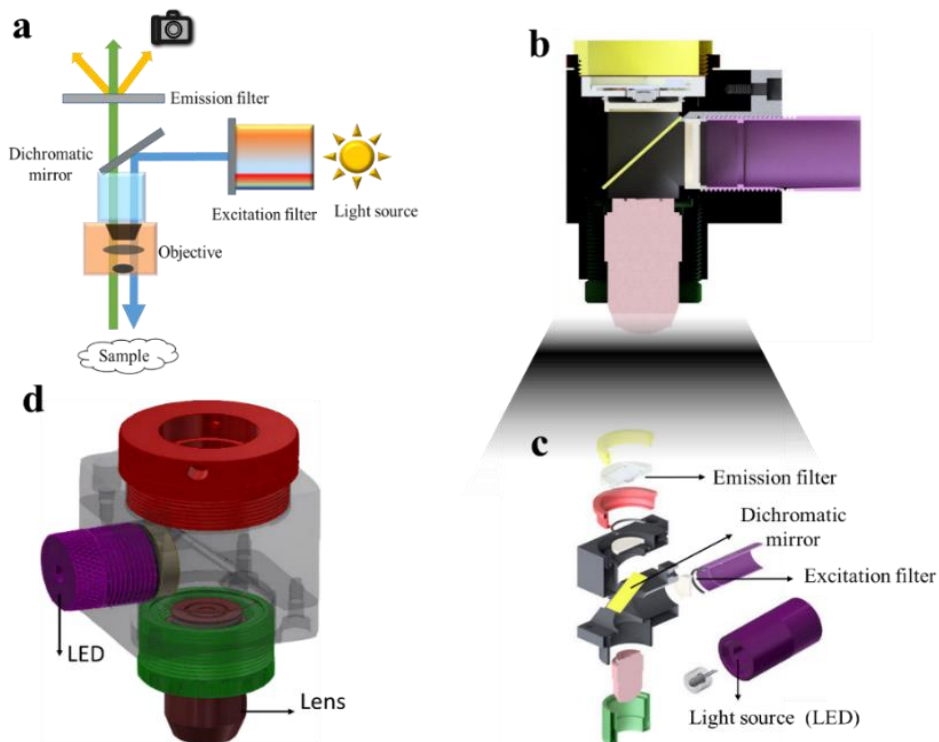


Figure 3-18: Fluorescence microscope (a) Basic Fluorescence Microscopy working Setup employed in commercial microscopes (b) 3D CAD design model of our portable digital fluorescence type microscope (c) exploded view has been shown (d) schematic of the 3D printed microscope mold

Microfluidic platform

The microfluidic chip consists of two saline glass layers with a thickness of 1 mm, top and bottom glass. Top glass has a 3D printed customized pattern, which consists of a 3.4 mm wide channel

leading to the cell culture chamber zone, which is 6.5 mm in width with a height of 350 μm . Channel was printed by inkjet printing technique using a biocompatible 3D printed silicone elastomer acquired from Nusil medical grade silicone (MD, 6003). The details of the printer along with the microscope is available in Fig. 3-20. Inertness and biocompatibility was the priority that gives itself to wide-ranging application conditions and is chosen elastomer in the biomedical application. To accurately control flow in the chip, a peristaltic pump was used. Peristaltic Pump is providing a constant flow rate of 60 $\mu\text{l}/\text{min}$, which comes in the laminar flow regime. Air bubbles are a recurring issue in microfluidics. To avoid any bubble formation inside the microfluidic chip, right after the pump, a bubble remover (obtained from Elve Flow) is installed at the inlet of the microfluidic chip to trap the air bubbles generated especially in long-term experiments. Cell culture, measurement, and analysis of cells have been taken place in the chamber area. The cell culture protocol on the bottom chip can be found in the experimental section. It is familiar that the concentration of ROS in cancer cells is producing at an elevated concentration by cause of oncogenic alteration including alteration in genetic, metabolic, and tumor microenvironment [37]. Breast cancer cells were chosen as they are usually submitted to the production of reactive oxygen species (ROS) and are ideally suited for ROS monitoring using the diacetate DCFDA fluorescence probe. An original of the platform has been shown in Fig. 3-19, showing a closed lid incubator and maintained the same culture conditions whose CO_2 and temperature were regulated at 5% and 37 $^\circ\text{C}$ respectively, by a feedback controller. The microscope focus can be adjusted by the microscope control probe by moving left and right while the stage control probe is providing movement to the chip in the upward and downward direction. It is a compact, user-friendly device, the user only needs to turn on, run the software on the computer, position the sample, and adjust the focus. The focus of the microscope was adjusted and images were taken by the microscope, the captured images will be available that can be seen directly on the computer screen.

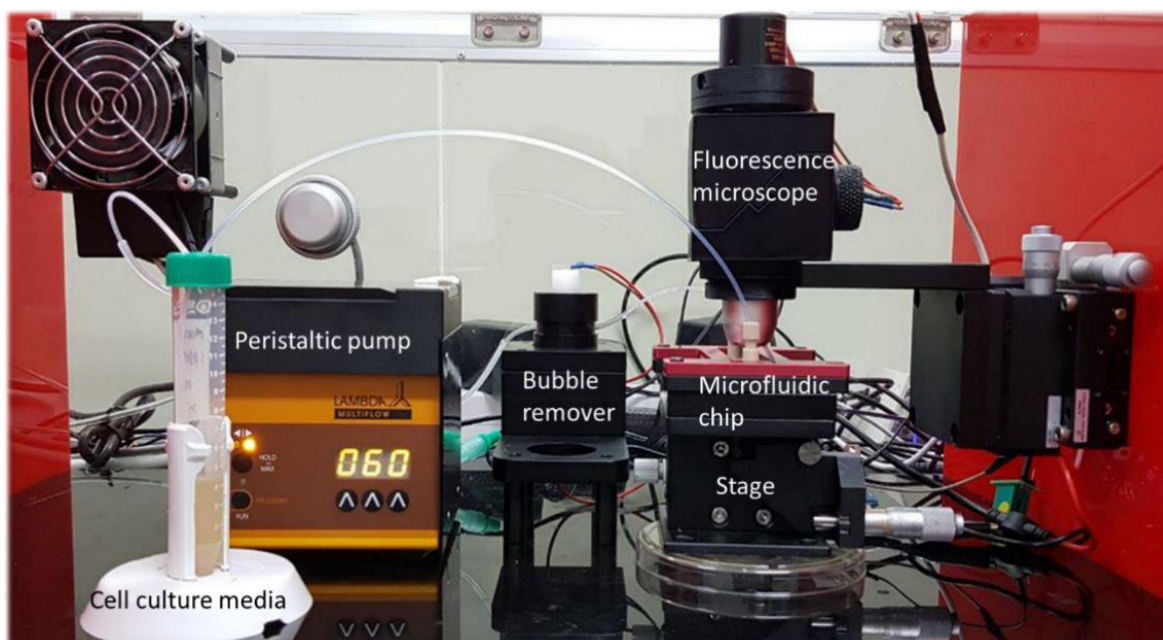


Figure 3-19: Actual platform image of the experimental setup for the online monitoring of ROS in breast cancer cell line MCF-7

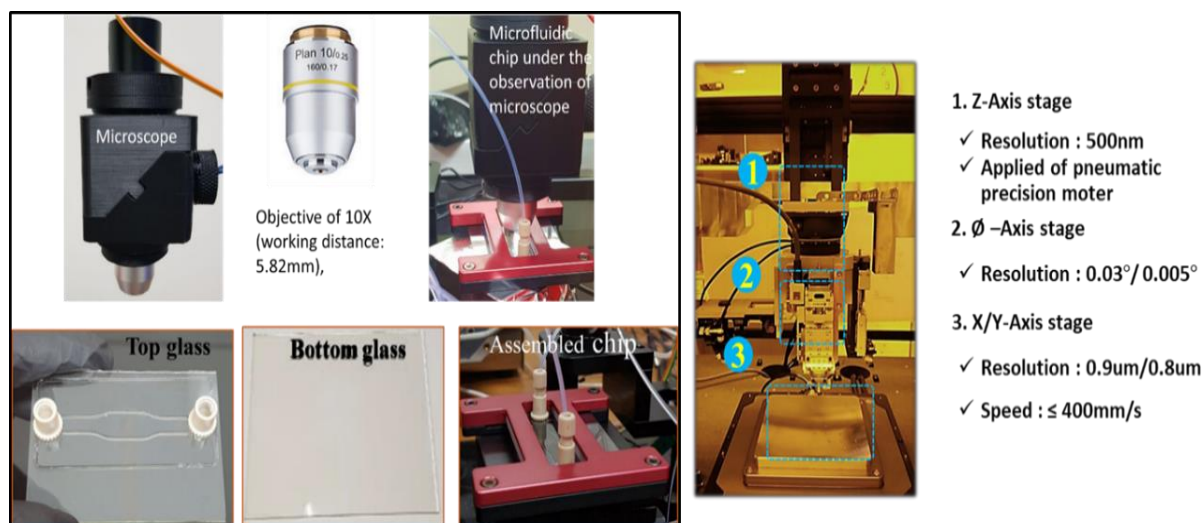


Figure 3-20: Platform images and Multi-head 3D printing specifications

3.2.8. Application: Real-time monitoring and evaluation of ROS in breast cancer cells line (MCF-7)

Fluorescence was recorded according to the following time schedules: every 3 hours and once after 24 h. A significant increase in the fluorescence was detected up to 24 h and after that, there was no significant increase in fluorescence. Real-time images of the MCF-7 cells were taken

through the microscope as shown in Fig. 3-21 and evaluated. A user-interactive Graphical User Interface based application as shown in supplementary data Fig. 3-22(a) was designed. In our case, we only displayed the histogram of green content present in the stills, which can be seen in Fig 3-22(c) along with waveform graph and green intensity graph respectively, and time vs fluorescence has been shown in Fig. 3-22(c). It can be seen in the figure that the color histogram has shown an increase due to the high green fluorescence content as per the image sequence taken. The green color waveform is displayed after the acquired image was converted into an individual array of three colors red, blue, and green; later green intensity array was separately plotted which infers the overall pattern of green fluorescence of the image. Apart from the qualitative data presented, the quantitative data was also acquired using LabVIEW. The intensity graph that extracts all color planes available in the image and converts into a 2D array of U8 intensity values and in the end produces the intensity graph; the intensity graphs are given in Fig. 3-22(c). In each image, the numeric value was two-dimensionally mapped on the scale of 0 to 255 for each color, and as a result, the magnitude of green color was determined in each image. It shows the concentration of intracellular ROS measured by fluorescence is being increased, as it can be seen enhanced fluorescence signals with increasing ROS concentration. Overall, the fluorescence microscope was useful for optical imaging of ROS produced in the glass-based microfluidic chip for online monitoring.

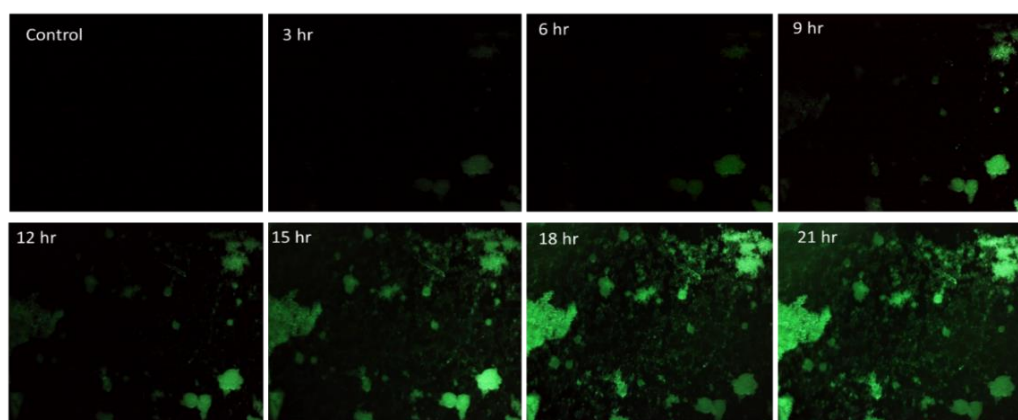


Figure 3-21: Real-time fluorescence images of the MCF-7 cells treated with 2',7'-dichlorofluorescein diacetate (DCFDA) taken through the fluorescence microscope using Toup

view software according to the following schedule: control, 3, 6, 9, 12, 15, 18, and 21 h. Scale bar is 100 μm .

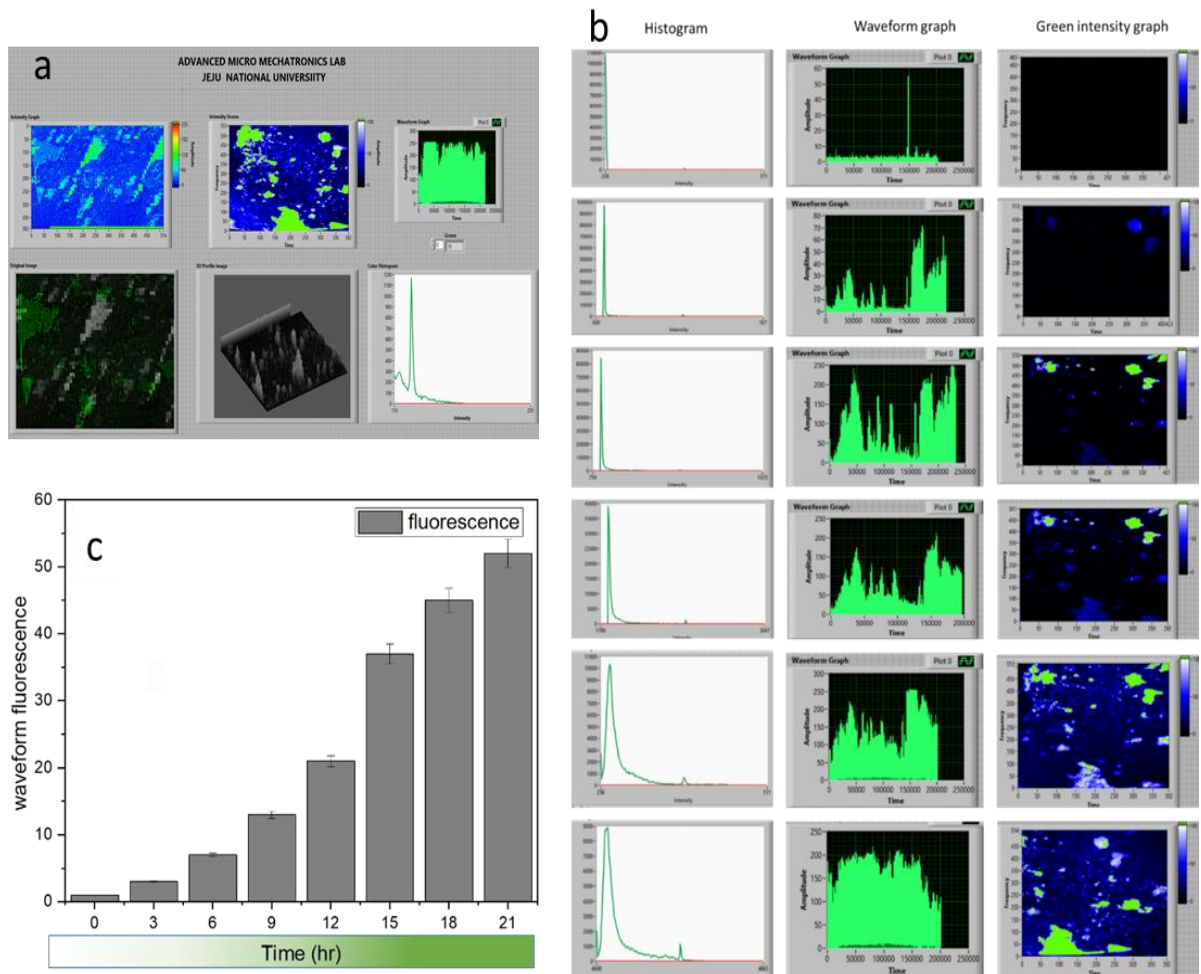


Figure 3-22 (a) A user-interactive Graphical User Interface based application (b) Histogram of green content present in the stills along with the waveform graph and green intensity of each image (c) time vs. green fluorescence obtained from the green wave through LABVIEW (data presented as mean \pm standard deviation (SD), $n=3$)

ROS depletion

A control experiment was performed which shows the reduction of ROS level with respect to time. ROS control experiment was performed under the same protocol for ROS depletion in MCF-7 cells in 96 wells plate to show the effect of AA on MCF-7 cells and in the microfluidic chip also. Thus, ROS scavenger ascorbic acid (AA) is used to deplete the intracellular ROS level to investigate ROS dependence. AA (100 μM) was introduced to act as an antioxidant and it has been reported in the literature that AA is a potent antioxidant and quenches ROS in cells under oxidative stress

¹⁴⁴. As shown in Fig. 3-23(a), ROS level in terms of DCF fluorescent intensity was quantified (control, H₂O₂, and Ascorbic acid introduction) by the SpectraMax i3 Multi-Mode Platform at an excitation of 530~560 nm and emission of 590~620 nm. The fluorescence intensity in normal cells in terms of DCF fluorescence is low as compared to cells induced with H₂O₂ (10 μM) and cells treated with AA (100 μM), which has shown depletion in fluorescence. The fluorescence was further confirmed by confocal Images as shown in Fig. 3-23(b). Furthermore, the effect of AA on ROS in MCF-7 cells was observed in a microfluidic chip for 24 hr, to reduce the effect of AA on cell proliferation and metabolism. Two different concentrations of AA (100 μM and 50 μM) were investigated by adding them into the RPMI media reservoir. Images at 0, 12, and 24 hr were captured as shown in Fig. 3-23(d,e) and quantified the ROS in terms of DCF fluorescence as shown in Fig. 3-23(c). In terms of 100 μM of AA, ROS depleted higher than 50 μM. It concludes that the ROS depleted gradually with respect to time.

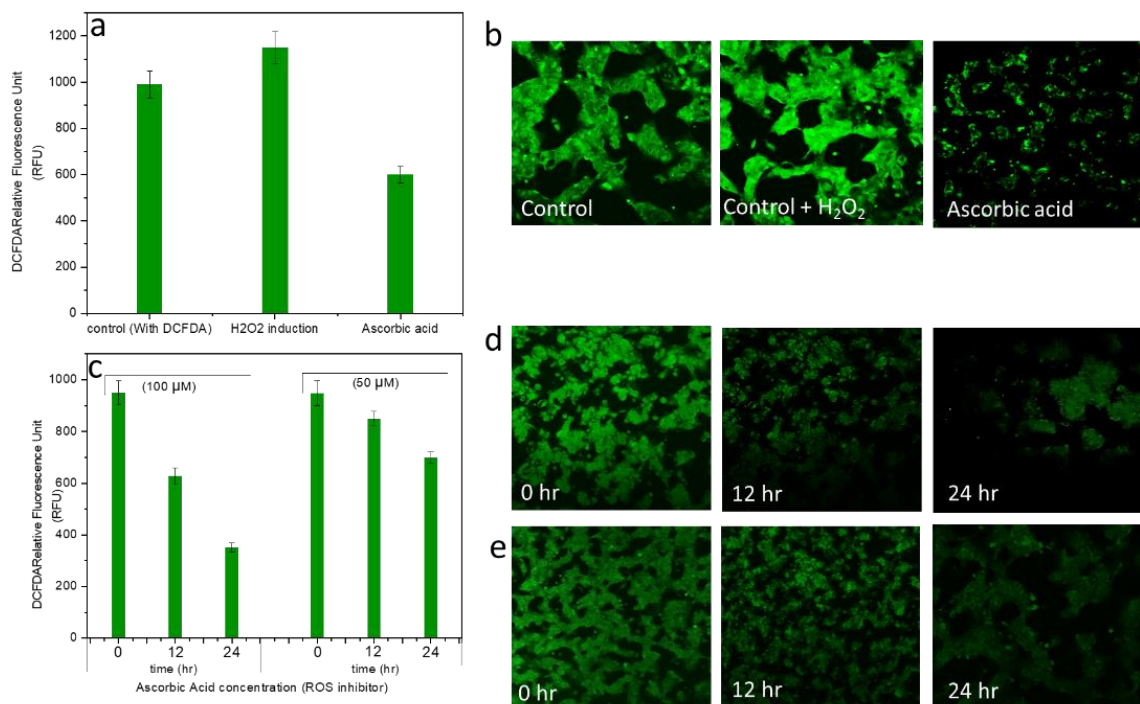


Figure 3-23: AA transfection in MCF-7 cells. **(a)** ROS level in terms of DCF fluorescent intensity (control, 10 μM H₂O₂ introduction and 100 μM Ascorbic acid introduction) after 24 hr **(b)** Intracellular DCFDA fluorescent intensity was visualized by confocal microscopy **(c, d)** Intracellular DCFDA fluorescent intensity after cells treated with 100 μM and 50 μM ascorbic acid over time (0, 12, 24) hr and were visualized by confocal microscope

Chapter 4. Colorimetric based biosensor

4.1. Colorimetric based Uric acid detection (non-enzymatic)

UA is a redox analyte and there are numerous sensors have been developed for its detection, mostly electrochemical based detection has been reported. The redox reaction produces hydrogen peroxide, which is eventually oxidized to generate a significant oxidation signal or show characteristic amperometric response at transducer surfaces. Enzyme based electrochemical sensors based on nanomaterials modified electrode including, uricase immobilized on ZnO nanowires⁴³, Nanorods⁵¹ Quantum dots¹², Chi-CNTsNF/AgNPs/Au⁵², Nafion/Uricase/ZnOmicro/NWs/Au⁵⁴, while non-enzymatic include Pt nanoparticles supported on reduced graphene oxide⁵⁶, Hierarchical nanoporous PtTi alloy¹⁴⁵, Nitrogen-doped zinc oxide thin films⁵⁸ have been developed to detect UA. Nanomaterials based enzymatic and non-enzymatic based sensors have shown excellent electrocatalytic activity to the redox behavior of UA. In literature there are some optical-based approaches have also been developed for sensing UA included CdTe nanoparticles as fluorescence probes¹⁴⁶, uricase/HRP-CdS QDs¹⁴⁷ with specific and high response. The shortcomings of the native enzymes used are limited natural sources, difficult and costly purification processes, and inherent instability¹⁴⁸. As a result, detection of redox-based biomarkers has now shifted to a non-enzymatic approach and in the case of antigens; MIP has introduced a paradigm shift in durable and stable detection procedures of various biomarkers¹⁴⁹. The colorimetric analysis is also a very good approach for determining the concentration of any chemical reagent (element or compound) in a solution with the aid of a color substance. For qualitative analysis, it can be observed with the help of naked eye while for quantitative analysis it needs a detection setup. Research on portable detection setup is rapidly advancing targeting an affordable POCT device¹⁵⁰. This strategy can be applied for both organic and inorganic compounds and it could be avail without enzyme substrate. Colorimetric sensors (qualitative based) have also the following advantages of low cost, uninterrupted measurement, minimized working steps, low

background signal, naked eye observable, and no need of any advanced instrumentations, the challenge exists of developing a quantitative device that satisfy with the ASSURED. UV-vis spectrophotometer can be used to make sure the difference in absorbance of color changes. TMB (3,3',5,5'-Tetramethylbenzidine) is used as a chromogenic substrate in colorimetric reactions, it reacts with H_2O_2 and form a transition complex in the presence of enzyme mimetics. TMB based bioassays included Prostate cancer cells (PSA)¹⁵¹, Cholesterol¹⁵², and Xanthine¹⁵³ in the presence of enzyme mimetics. Naturally, some nanoparticles are having peroxidase-like activity such as MoS_2 nanoparticles have been used for the detection of H_2O_2 ¹⁵⁴, Silica encapsulated gold (Au) nanoparticles set an example as a glucose oxidase and peroxidase-like artificial enzyme¹⁵⁵, Graphene oxide for the detection of glucose¹⁵⁶, Carbon nanodots as peroxidase mimetics¹⁵⁷, polymer-coated cerium oxide nanoparticles¹⁵⁸, and Single-wall carbon nanotubes (SWCNT)¹⁵⁹, have been extensively used as nanozyme for sensitive bioassay due to their excellence bioanalysis capabilities over the past decade. Presently, colorimetric based sensing for UA includes MIL-53(Fe)¹⁶⁰, Ultrathin Graphitic carbon nitride nanosheets ($g-C_3N_4$)¹⁶¹, were used as peroxidase (nanozyme). However, interference in biological samples such as biothiols is the most likely hindrance, upsetting the catalytic activity of nanosheets; the methods need dangerous reagents and time consumable. An another colorimetric sensing platform for the detection of UA has established based on Cu^{+2} catalyzed TMB, but the limitations to this method is the involvement of uricase enzyme and coverage of low detection range¹⁶². Platinum nanoparticles (Pt Nps) were used as nanozyme for the detection of glucose¹⁶³, and as a smart probe for the ultrasensitive detection of mercury¹⁶⁴ due to its outstanding properties. Consequently, PtNps can be chosen as a prevailing nanozyme to catalyze the oxidation of TMB to generate signal amplification in colorimetric recognition due to its premium catalytic activity, biocompatibility, good stability and easy synthesis. It has also been identified that PtNPs have used for catalyzing the oxidation of organic substrates in the presence of O_2 , H_2O_2 respectively¹⁶⁵. To the best of our knowledge, the

quantitative detection of UA using a portable color sensor as POCT device through interaction with PtNps as a peroxidase enzyme mimetics has not been reported till date.

In the light of the above need to detect UA at the patient site, we decided to develop a point-of-care, colorimetric detection using PtNPs as a nanozyme. In this report, citrate capped PtNps (biocompatible) have been synthesized by reduction method and characterized by SEM and UV-vis spectroscopy. A facile, portable, and sensitive colorimetric sensor for the quantitative detection of UA has been developed on the peroxidase-mimetic activity of PtNps. A portable, low-cost, and easy to fabricate, and user-friendly color POCT setup was fabricated that incorporated color change upon the introduction of a paper strip. A quantitative analysis of UA can be done at the user site. Here we have used the colorimetric redox reaction of 3,3',5,5'-tetramethylbenzidine for UA analysis, and the parameters affecting UA measurement were all investigated. Our basic approach of this portable device is depending upon the particular interaction of Pt Nps with UA. The oxidation of TMB in the presence of PtNps, which yields a dark blue color on paper strip as it comes into contact with UA, dramatically change of color from blue to yellow take place due to the reduction of oxidized TMB. This color shift could be observed by the naked eye which provides qualitative information but the developed colorimetric detection approach made it facilitate quantitative information. The simplicity of the device provides an alternative to the most frequently used conventional device. To the best of our knowledge, such quantitative detection of UA through Pt NPs treated cellulose strip using a wireless POCT setup has not been reported yet.

4.2. Citrate capped Pt nanoparticles (PtNPs) synthesis

The synthesis of PtNps includes a four step procedure: (a) A precursor solution of Chloroplatinic acid hexahydrate $\text{H}_2\text{PtCl}_6 \cdot (\text{H}_2\text{O})_6$ was prepared by dissolving 7 mg of $\text{H}_2\text{PtCl}_6 \cdot (\text{H}_2\text{O})_6$ in deionized water (40ml), upon which the pH of the solution was adjusted by the addition of 1 N NaOH solution under dynamic stirring. (b) Trisodium citrate dihydrate ($\text{C}_6\text{H}_5\text{Na}_3\text{O}_7 \cdot 2\text{H}_2\text{O}$) solution (100 mM) was

prepared by dissolving 0.148 g in 5 ml DI water, it has been used as a capping agent to preclude the particles from growing beyond the nanometric size of interest. (c) Afterward, a portion of 400 μl was vigorously mixed with TCD and kept on a magnetic stirrer to make it properly mixed with it. The mixture was maintained at room temperature (25°C) for 30 min. (d) eventually, a few drops of a freshly prepared solution (0.2 ml, 50 mM) of Sodium borohydride (NaBH_4) has been added and stirred it until a uniform color change was observed. The colorless reactant mixture immediately turned light brown. A colloidal solution of Pt nanoparticles was prepared, stored at 4°C, and out of reach of light until further use.

4.3. Non-enzymatic based UA detection

A protocol has been followed for the detection of Uric acid as shown in Fig. 4-1. First, cellulose substrate was cut in the form of a circular-shaped strip of 8 mm diameter, which could be handled easily. A circular area of the strip was treated with polyvinyl alcohol (PVA) and let dry at room temperature. A mixture of TMB and H_2O_2 (5:1 v/v) was prepared, 80 μl was added to the strip using a micropipette. Subsequently, followed by adding 40 μl solution of citrate capped Pt Nps, where a colorless solution of TMB is oxidized in the presence of H_2O_2 and the bluish-green color was observed on the strip. TMB act as a hydrogen donor for the reduction of hydrogen peroxide in the presence of Pt NPs (peroxidase-like activity), producing diimine ($\text{RCH}=\text{NR}'$) causes the substrate to take on a blue color as shown in Fig.4-1(a), and this color can be read on a spectrophotometer at the wavelength of 650nm. Now, this bluish-green color strip can be used for the detection of the target analyte (UA). By the introduction of UA on the surface of the strip causes the substrate to turn yellow. This change is due to the reduction of oxidized TMB. Depends upon the concentration of UA the bluish-green color gradually declined to yellow as shown in Fig. 4-1(b), and this color variety has been observed by a portable colorimetric detection setup which has facilitated wirelessly and gives quantitative information of the target analyte.

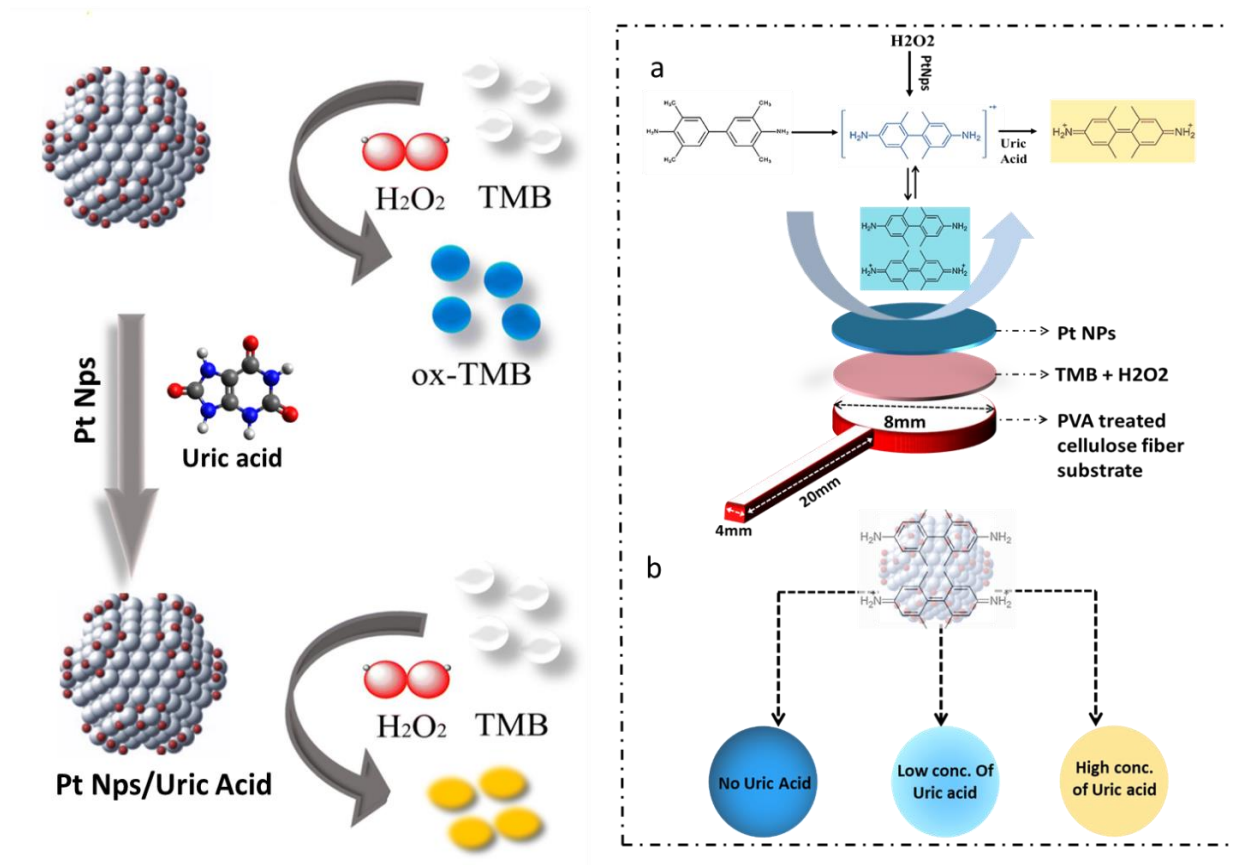


Figure 4-1: Illustration of the detection of UA using Pt NPs **(a)** Cellulose strip treatment protocol and mechanism of the response to UA introduction. **(b)** Color variation upon the introduction of different UA concentration.

4.4. Design of POCT device

Some off the shelf electronics components along with an Arduino nano microcontroller and Bluetooth (HC-06) slave module have been used for the measurement setup were used and placed inside a 3D printed assembly (designed in Creo 3.0 and printed using CreaLity CR-20 3D Printer) to complete the portable POCT unit. The device works on the principle of colorimetric quantification. For this purpose, a white LED and a photodiode was used in the measurement setup. A cellulose strip treated with PVA, TMB + H_2O_2 , and PtNPs loaded with sample and dried as described previously is inserted inside the portable setup opening and is illuminated using a white LED. From the other side, a photodiode measures the light intensity after absorption through the sample.

This colorimetric quantification approach allows better estimation in programming the controller for measurement as the light intensity changes with the change in color of the strip (full thickness) due to a change in analyte concentration. For transmission of light, the LED and Photodiode (PD) have been placed in close proximity (3mm) to the Absorbance strip area for maximum response and minimum loss. This approach has been graphically illustrated in Fig.4-2 (a and b) along with POCT device images.

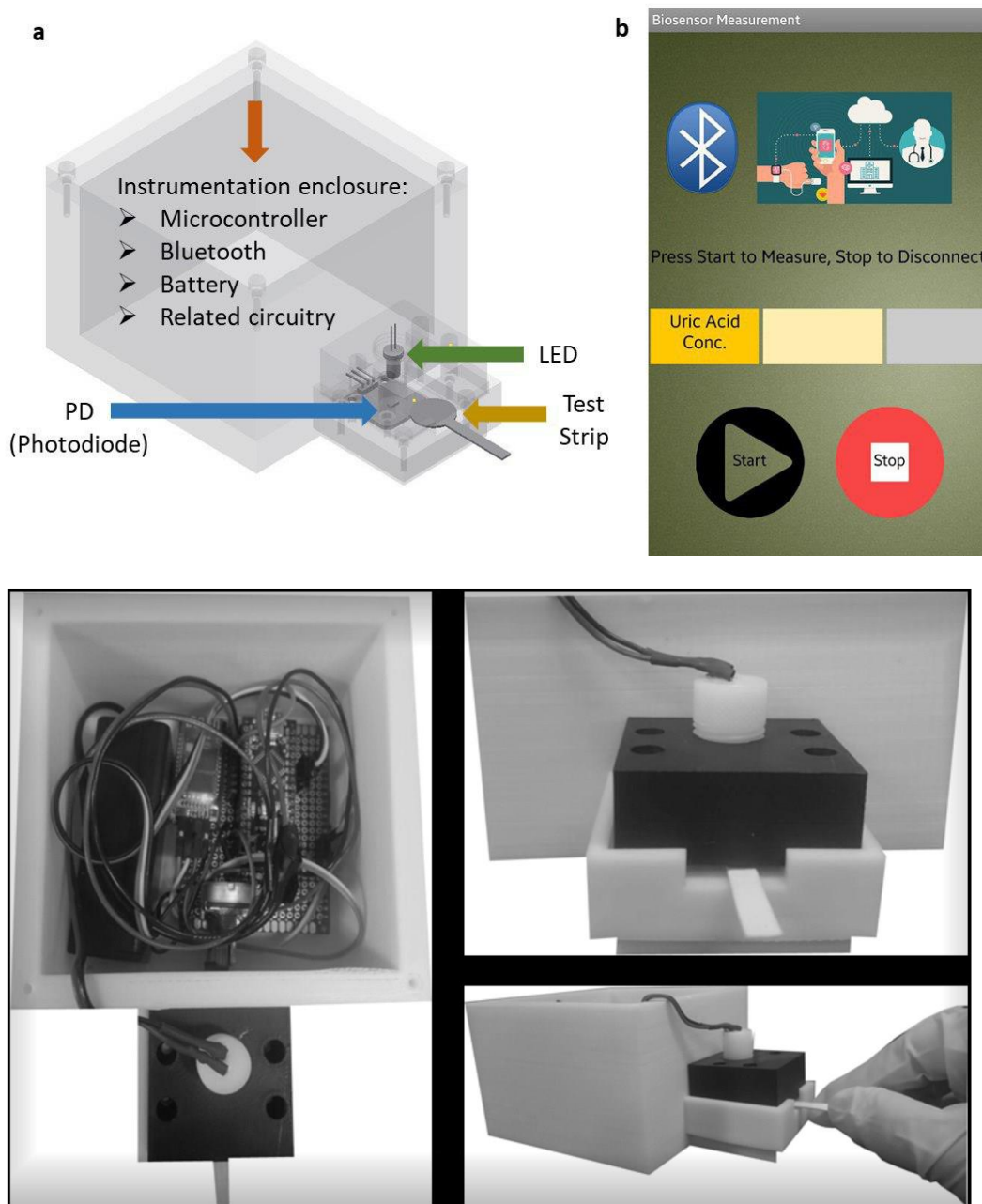


Figure 4-2: (a) Schematics of the portable POCT unit (b) Android-based application for POCT test and POCT device images (front, side, and top view)

4.5. Characterizations of PtNPs

PtNps were synthesized by reduction method with a proper stabilizer (citrate); a light yellow color colloidal solution of the nanoparticles was obtained. Initial evaluation attempted to distinctly identify the Particle size which was carried out through UV-vis spectroscopy. The Ultraviolet-visible (UV-vis) spectroscopy was used to measure the specific wavelength of the light absorbed by PtNPs colloidal solution. The specific wavelength (nm) of any colloidal particle solution made it specify their size¹⁶⁶. An aqueous dispersion of the nanoparticles has been observed in the range of 200-800 nm, but no distinct absorption peak has been perceived. The absorption spectrum of the synthesized nanoparticles has shown in Fig. 4-3(a), which corresponds to a fully reduced solution and has shown the particle average size in the range 8-10 nm. Further details of the microscopic structure to show the morphology of the PtNPs were provided by Transmission electron microscopy (TEM). As shown in Fig. 4-3(b) the structure of the nanoparticles, notably the Pt nanoparticles have diameters in the range of 8-10 nm. The histogram of the nanoparticles has shown in the inset image to show the respective average diameter size of the nanoparticles. Besides PtNPs characterization, the morphology of the cellulose membrane used as a substrate (strip) for the detection of UA has been analyzed FESEM as shown in Fig. 4-3(c) at a resolution of 10 μm . It can be observed from the image as shown here that it has consisted of cellulose fiber. In addition, modified with PtNPs' SEM images have been given in Fig. 4-3(e). It was difficult to locate nanoparticles on the surface of the substrate because of its tiny particle diameter. In addition, these nanoparticles were individually characterized by TEM. After dispensing of the PtNPs using a micropipette, the dispersibility of the nanoparticles has also been perceived by taking the EDS elemental image as depicted in Fig. 4-3(d). PtNps were also confirmed by XRD studies as shown in Fig. 4-4.

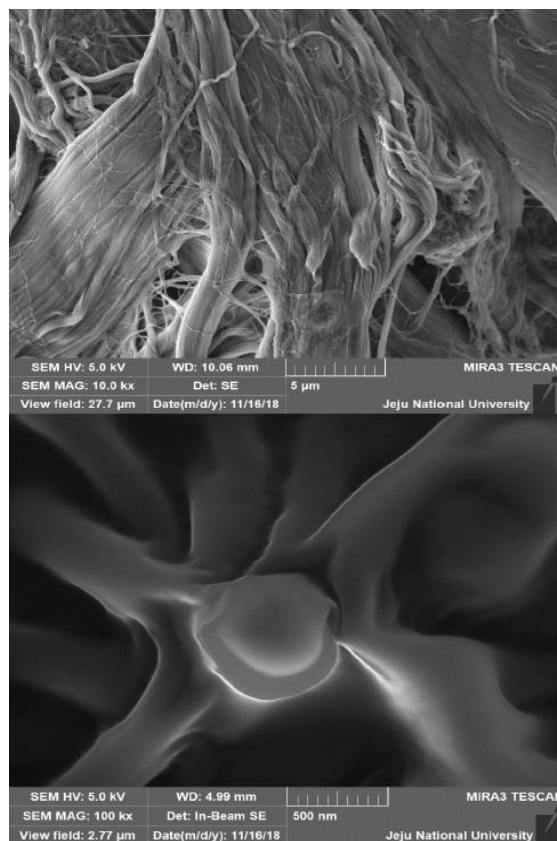
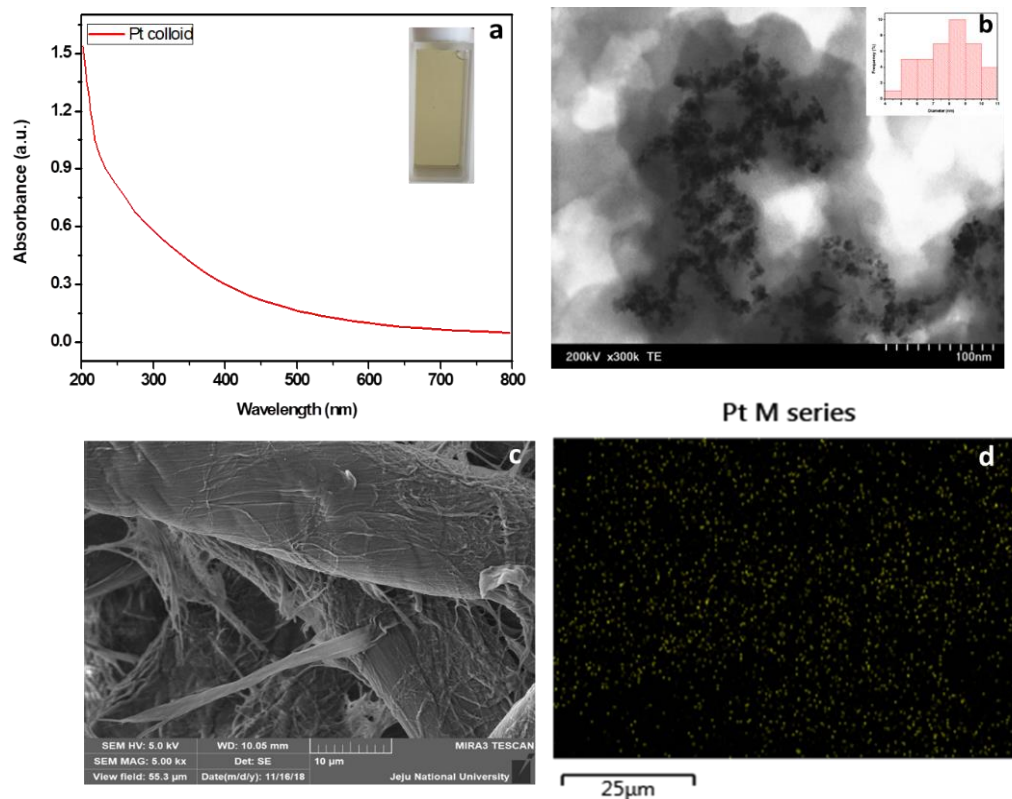


Figure 4-3: (a) UV-vis spectra of PtNPs colloid solution (b) TEM images of as-prepared citrate capped PtNPs with the inset image of the histogram of synthesized PtNPs (c) FESEM image of

cellulose substrate (d) EDS elemental image of PtNPs dispersed on the substra

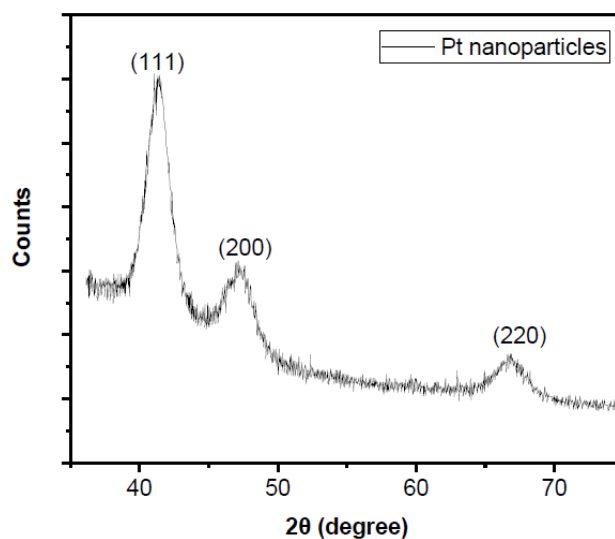


Figure 4-4: XRD pattern of as-synthesized Pt nanoparticles by the reduction method

4.6. Colorimetric sensing mechanism

To evaluate the catalytic oxidation of TMB under the synthesized PtNPs, UV-vis spectroscopy was carried out of different test solutions as shown in Fig.4-5. A much stronger absorbance peak at 650 nm was observed in the case of TMB + PtNPs + H₂O₂ (curve a), in the case of TMB + PtNPs + H₂O₂ + UA, peak was observed (curve b) of low intensity due to the addition of UA, while in the absence of PtNPs in the same solution a lower intensity peak can be located (curve c) due to the reduction in the color range of solution. The UV-vis spectra of the resulting solution decrease with an increase in the concentration of UA, as portrayed in cure a, b, and c respectively. Interestingly, no absorbance peaks have been observed for TMB + H₂O₂ and TMB + UA respectively (curve d, e) and in the case of TMB + PtNPs + H₂O₂ + UA (curve f) has been obtained due to high concentration of uric acid (7 mM). The control reactions carried out with TMB in the absence of PtNPs unable to produce a blue color. These results illustrate that the Pt NPs play the role of nanozyme to detect UA by the reduction of TMB. Moreover, the color change is in good accordance with the different test solutions with the resultant absorbance. Thus, the following phenomenon is confirming the peroxidase activity of the PtNPs and such a typical color reaction is exhibited by the enzymes and

many other nanoparticles¹⁶⁷. It has been concluded that PtNPs catalyzed TMB-H₂O₂ approach can be applied to UA sensing. A colorimetric based sensor was developed for the detection of UA using PtNPs as nanozyme by the combination of two reactions, which can be expressed by the following reactions:

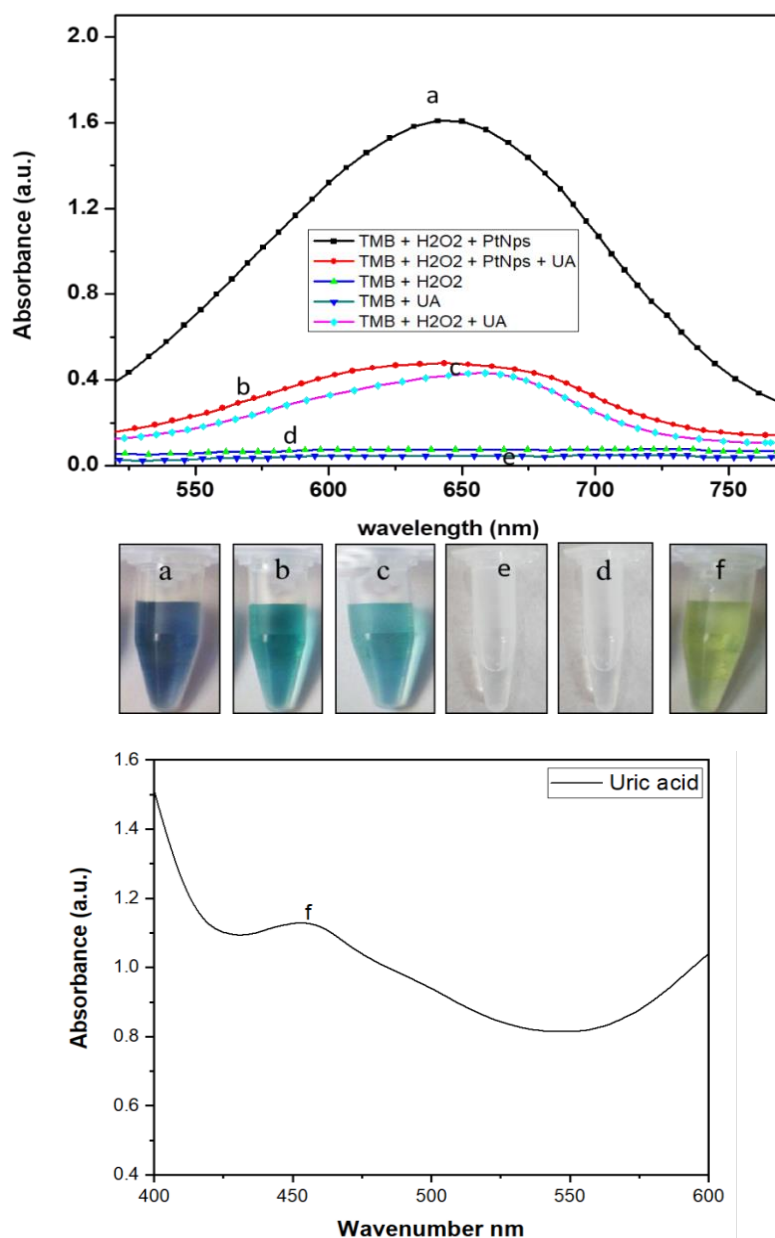
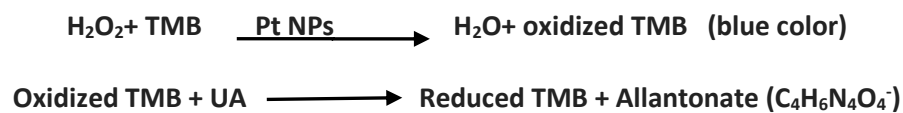


Figure 4-5: UV-Vis absorption of (a) TMB + PtNPs + H₂O₂ (b) TMB + PtNPs + H₂O₂ + UA (c) TMB + H₂O₂ + UA (d) TMB + H₂O₂ and (e) TMB + UA, and (f) TMB + PtNPs + H₂O₂ + UA along with the corresponding photographs

To seek the best performance of the UA sensor, several strongly dependent experimental parameters including the concentration of Pt nanoparticles, TMB concentration, H₂O₂ concentration, and pH were evaluated. To observe the effects on the absorbance of oxidized TMB and detection of UA, they should be systematically examined. These parameters have considered a significant effect on the detection of UA, and nanozyme concentration, H₂O₂, and pH should be optimized. The relative activity was used as a norm to optimize the sensing conditions of UA and described as relative activity $(A-A_0/A)$, here A and A₀ are the absorbances of the sensing mechanism in the presence and absence of the target analyte (UA). As shown in Fig. 4-44(a) the relative activity of UA detection was carried out by varying the concentration of nanozyme (PtNps) from 1–6 mM and the optimized concentration was chosen as 3.3 mM. In the same manner, the other factors were also examined to optimize the experimental parameters for the detection of UA, such as TMB from 4–24 mM, the H₂O₂ from 6–10 mM, and the pH from 2–5. The optimum concentrations for TMB, H₂O₂, and pH of the solution were chosen as 20 mM, 8.8 mM, and 4.2 respectively. The peroxidase-like activity of PtNPs was first chosen to set the other parameters. As shown in Fig. 4-6(a) the relative activity of Pt NPs concentration increased up to 3.3 mM, above which it was declined. The reason is due to the oxidation of TMB by dissolved oxygen through the catalysis of Pt NPs. The effect of TMB concentration was studied in the range of 4–24 mM as shown in Fig. 4-6(b) investigated that too low concentration was not suitable for the reaction system. The effect of H₂O₂ concentration was evaluated and found that too low concentration was not suitable for the effective reaction condition, after 9 mM there is a drastic change in the conditions of analyte detection as shown in Fig. 4-6(c). The effect of pH on the catalytic activity of Pt NPs was studied in the range of 2.0–5.0 as shown in Fig. 4-6(d) the relative activity of the sensing system increases effectively in the range 3.5–4.0, and then shifted to decline with further increase in the pH which may be recognized to the reducing affinity of Pt NPs for aqueous phase. It was acquired that relative activities have increased gradually while

increasing the concentration of each parameter

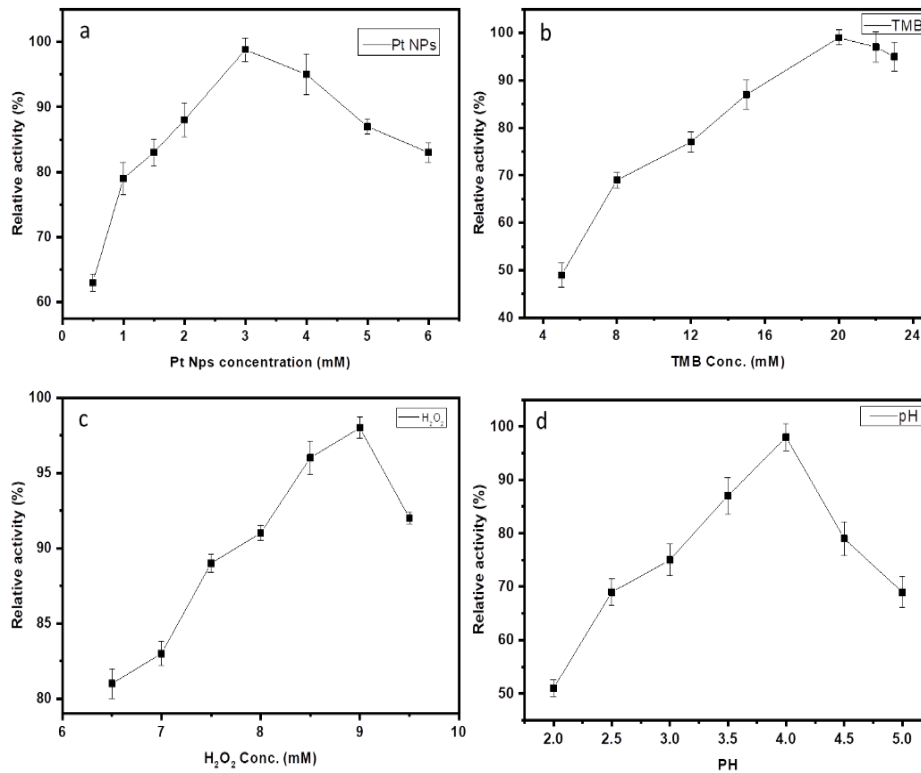


Figure 4-6: Optimization of different parameters for reaction conditions (a) effect of Pt NPs concentration (b) TMB concentration (c) H₂O₂ concentration (d) pH

4.7. Theoretical calculations

To show the fluid diffusivity (velocity contour) on the surface of cellulose fiber strip and color variation upon the introduction of various concentration of uric acid, simulations were carried out at different concentration from 1 to 8 mM by COMSOL 5.3. The round head shape of the strip was 8 mm and thickness of 0.83 mm was utilized in theoretical calculations. The free porous media flow and transport of diluted species Modules were utilized for this purpose. The velocity and concentration profiles in the case of 8 mM are respectively as shown in Figure 4-7(a) and (b). It has been observed from simulation results that the concentration profile changes its color intensity as observed in the experimental with the increase in the concentration of uric acid, ranging from 1 to 8 mM. The concentration vs. color simulation results has been obtained

individually for each concentration value as shown in Fig. 4-7(b) which shows that by keeping on increasing the concentration value, the color of the strip changes.

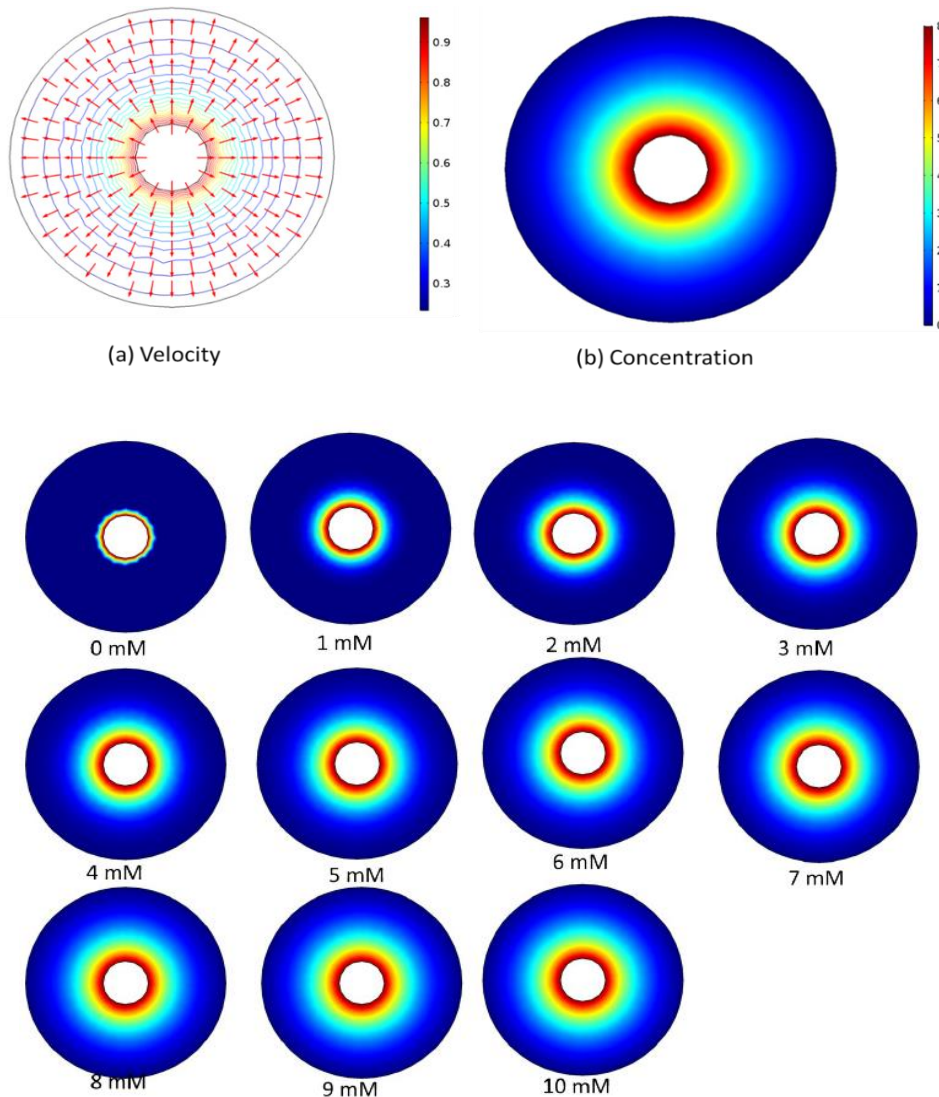


Figure 4-7: (a) Velocity contour along with the arrow surface (b) Strip color range under the observation of various concentrations of uric acid solution ranging from 1 to 8 mM

4.8. Detection of Uric Acid on cellulose strip

A series concentration of UA ranging from 0 mM to 8 mM have been analyzed on the optimized paper strips, an assay was evaluated to determine the effect of varying concentration of UA, the developed absorbance based Bluetooth POC setup could recognize its quantitative information.

The color variation of different UA solutions from dark blue to yellow can be directly observed by the naked eye as shown in Fig. 4-46(b). To make the detection method more users friendly and sensitive, we have implemented this concept for the quantitative detection of uric acid at the patient's site. The circular head of the strips was treated with 0.1% PVA to avoid the unbalanced spreading of the liquid on the hydrophilic surface of cellulose paper, and it also helps biomolecules to preserve their functional characteristics as present in the literature [32]. 80 μ l of TMB + H₂O₂ has been observed to fully cover the 8 mm diameter circular area, followed by the introduction of 40 μ l PtNPs. An instant color change from colorless to dark bluish-green has been observed which is claiming the oxidation of TMB by H₂O₂ in the presence of PTNPs. Strips were remained uncovered to let it dry at room temperature (25°C) for 20 min. To take on initial readings, this blue color area has been observed by inserting the strip in the POCT device, which shows a reading, equals to 0.3 ± 0.02 V. Strip insertion area has been designed in such a way, which avoids the effects of environmental factors on strip absorption. This value has been taken the initiative for all the samples prepared for UA analysis (variable concentration). Nine strip samples were prepared, which were having the same bluish-green color at the circular head has faded to different extents depending on the concentration of UA. Based on the concentration of UA present in the sample the reduction of TMB used to have initiated. After a few minutes, all the strips have been observed under the colorimetric based sensor for quantitative analysis, and the respective cases are presented. One can observe a gradual color change with increasing UA concentrations. This figure at the most left shows a dark bluish-green color without UA and the last one shows the response of TMB reduction with the high concentration of UA. Based on the intensities obtained from the developed sensor, a calibration curve was plotted and presented as shown in Fig. 4-8(a). It states the absorbance variations of variable concentrations of UA along with the respective standard deviations. A best linear curve has been obtained along with its mathematical expression. The PtNPs based detection of UA on cellulose substrate and its quantitative analysis could be seen to respond in a linear behavior from 0 mM to 8 mM. It

has been observed that a linear range was observed up to 7 mM and then it started to decline the color differentiation and the images are shown in Fig. 4-8(b). The sensitivity of the sensor was acquired from the slope of the calibration curve, which equals to 0.12 abs/mM.mm². It has shown that the developed method for the quantitative detection of UA through PtNPs responded productively with a calculated LOD $4.2 \pm 5 \mu\text{M}$. The contribution of this approach in the field of POCT device is the detection within the physiological range of UA present in the urine samples (1.5–4.4 mmol/day). A comparison table is given of this approach to previously developed methods for colorimetric detection of UA in Table 8.

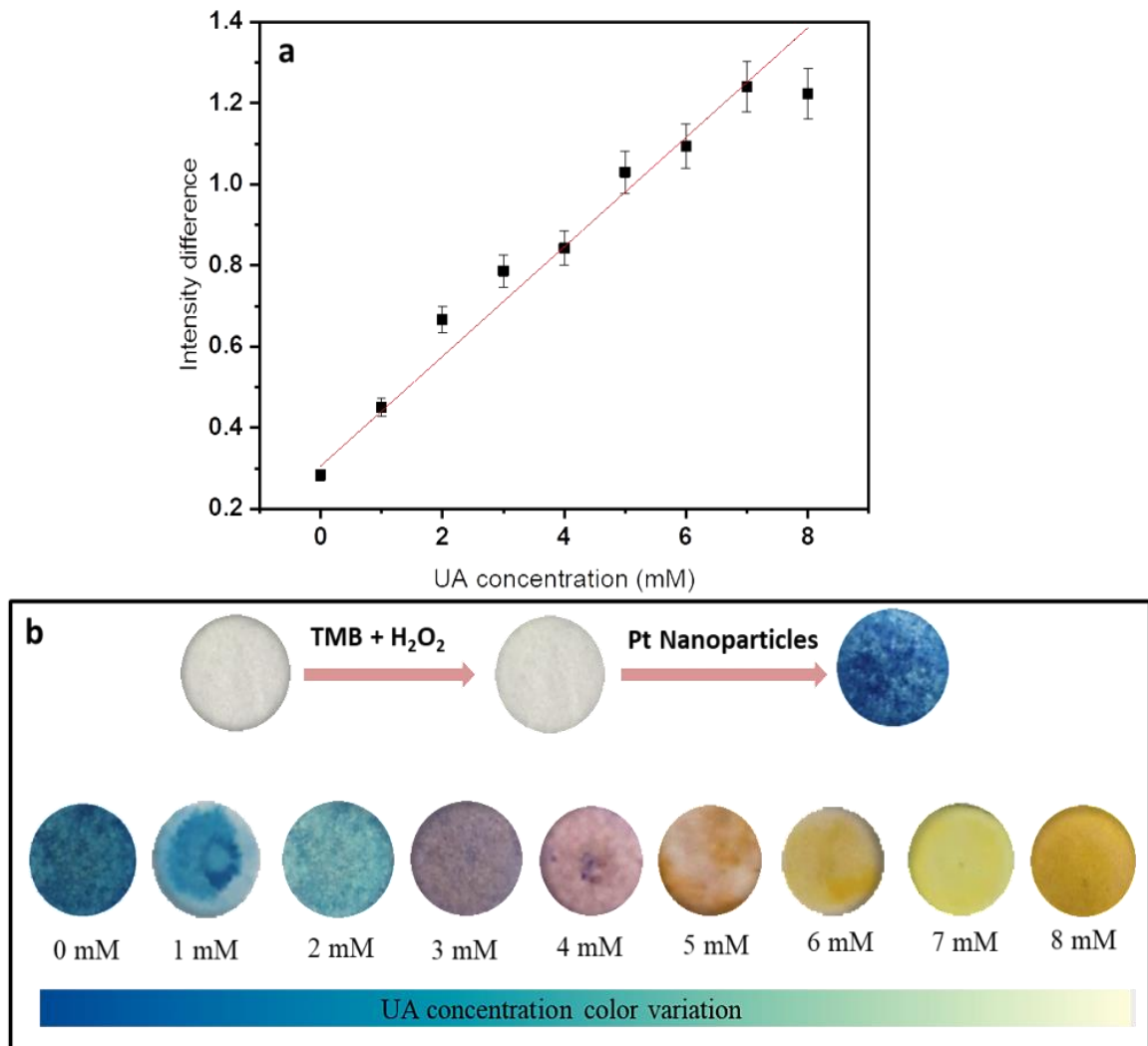


Figure 4-8: (a) Response curve for UA detection (cellulose strips) vs intensity difference in the range from 0 to 8 mM (n = 4) (b) Images of varying concentration of UA on paper from 0 mM to 8 mM, respectively.

Table 8. Comparison of the developed PtNPs based detection (colorimetric stimulated) with the other reported uric acid analysis

Biosensor composition	Real sample	Sensor type	Linear Range	LOD	Ref.
OD	urine	colorimetric	1.0 - 5.0 mM	0.15 mM	¹⁶⁸
4-AAP/DHBS	urine	colorimetric	1.0 – 5.0 mM	0.3 mM	¹⁶⁹
2-thiouracil (2-TU) tailored Au nanoparticles	serum	colorimetric	–	0.5 μ M	¹⁷⁰
Uricase/MIL-53(Fe)	urine	colorimetric	4.5 – 60 μ M	1.3 μ M	¹⁶⁰
Uricase/HRP-CdS quantum dots	urine	colorimetric	125 – 1000 μ M	125 μ M	¹⁷¹
TMB–Cu ²⁺ uricase	urine	colorimetric	1 – 1000 μ M	0.64 μ M	¹⁶²
Ag nanoprism/uricase	serum	colorimetric	1 – 40 μ M	0.7 μ M	¹⁷²
TMB/g-C3N4 /uricase	Not reported	colorimetric	1 – 100 μ M	8.9 μ M	¹⁶¹
TCPO/H ₂ O ₂ /rubrene	serum	chemiluminescence	10 – 1000 μ M	5.0 μ M	¹⁷³
CdTe nanoparticles	serum	Fluorometric	0.22 – 6 μ M	0.1 μ M	¹⁴⁶
TMB+H ₂ O ₂ and PtNPs	urine	colorimetric	0 – 8 mM	4.2±5 μ M	This work

4.9. Application: Detection of UA in urine samples

The reproducibility of UA detection using PtNPs as a nanozyme (peroxidase-like catalytic activity) on cellulose strip was evaluated as shown in Fig. 4-9(a). To estimate the reproducibility parameter of the proposed sensor and detection measurement, four strips were prepared

followed by the same protocol as stated above and a 3 mM concentrated solution of UA (pH 6.5) was investigated under the same conditions. At the same time, a drop of 50 μ l of UA solution was introduced on the prepared strips and left it to dry at room temperature. The same color was acquired on the four strips and has been analyzed by the developed colorimetric sensor to obtain quantitative information based on its color absorption mechanism. As depicted in the figure below each strip is having the same color, and an acceptable standard deviation (RSD) of less than 5% was obtained. The stability of the response of reduced TMB in the presence of the same concentration of UA has shown good reproducibility. In addition, the sensor response has exhibited acceptable consistency. Human urine included other inorganic substances (K^+ , Na^+ , Mg^{2+} , and Zn^{2+}) and organic constituents such as several amino acids and other small biological molecules like glucose, ascorbic acid, oxalic acid, and urea. To investigate the selectivity/specificity of this developed assay was tested in the presence of 5 mM of the following interferences such as oxalic acid, sodium chloride, potassium, amino acid, and uric acid respectively. The result has shown in Fig. 4-9(b) which is describing that the effect of interferences molecules is little on the reduction of TMB. One can obtain remarkable selectivity as shown in inset images. As a result, it has been concluded that PtNPs based UA detection has an outstanding selectivity. For real-time analysis, the protocol has been followed reported in our previous work [10] and has been taken that as a standard for validation of this developed approach. As shown in Table 9 the recovery falls in the range between 97% and 103%.

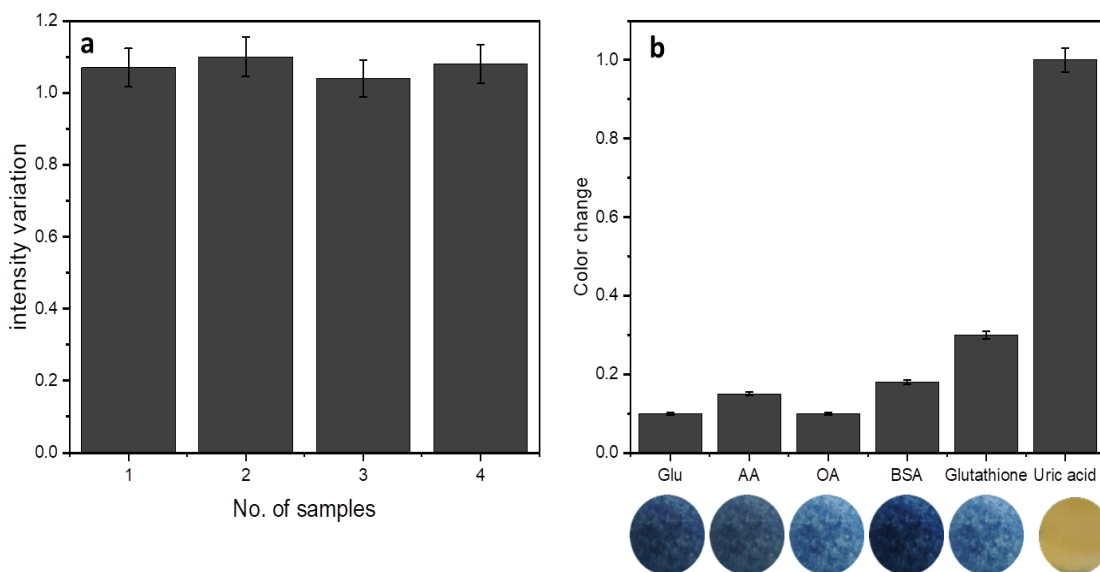


Figure 4-9: (a) Reproducibility measurement (n=4) sensor response to uric acid and detection by the developed colorimetric setup (b) Selectivity response of the developed assay to various interferences and UA

Table 9. Determination of uric acid in urine samples using the PtNPs based colorimetric sensor (n=3)

Sample	UA concentration founded by electrochemical sensor (mM)	Content	Added (mM)	Found (mM)	Recovery (%)
Urine	3.25	1.1	2.1	3.21	1.3
	3.95	1.5	2.5	3.97	99
	4.95	3.5	1.5	4.89	97

Conclusion and future work

In summary, this thesis has reported the development of high performance electrochemical and optical-based biosensors, targeting point-of-care devices. Our target was to boost up the role of the transducer surface through nanostructured materials (NSMs) which is an aid in improving the immobilization of biomolecules (enzymes) and converting the biorecognition events into the quantifiable signal. The aim was to improve the immobilization process easily, which has facilitated the response of the sensor in terms of sensitivity, high range of detection, low limit of detection, stability, miniaturization, and response time. In this regard, this work focused on the complete study of the synthesis, functionalization, bioconjugation, and characterizations of NSMs and nanostructured composite for biosensor development. The targeted nanostructured materials include zero-dimensional (0D) ZnO QDs, PtNPs and UCNPS, one-dimensional (1D) MWCNTs, and two-dimensional (2D) MWCNTs/PEDOT:PSS nanostructured composite and other than this bioconjugation of the upconverting nanoparticles (NayF₄: Yb, Er) with aptamers. The applications include the objective detection of important biomarkers (biological molecules) such as Uric Acid, Lactate, Vaspin, and Reactive oxygen species (ROS) for the targeted disease intervention. Various important parameters were optimized to attain the best performance of the sensors. The summary and key conclusion of this research are as follows:

- ZnO QDs (4–6 nm) were synthesized by precipitation method and deployed successfully for the detection of Uric Acid on the screen-printed carbon electrode. Uricase enzyme was successfully immobilized on the nanostructured guiding layer of the quantum dots due to the high isoelectric point (IEP). The sensor exhibited linear behavior in the concentration range of 1–10 mM UA with a high sensitivity of 4.0 $\mu\text{A}/\text{mMcm}^{-2}$. Screen-printed sensors are highly commendable for ease of fabrication, so it can be fabricated in mass quantity with low prices.

- A composite of multi-walled carbon nanotubes (MWCNTs) and poly (3,4-ethylene dioxythiophene)-poly(styrene sulfonate) (PEDOT:PSS) was synthesized for the quantitative detection of lactate. LOX was successfully immobilized on this biocompatible nanostructured composite. The developed sensor provided a wide linear range response ($R^2 = 0.97$) from 1 mM to 10 mM for buffer samples with 35.224 $\mu\text{A}/\text{mM}$ sensitivity. The proposed sensor was applied to detect lactate in cancer (MCF-7) cells media.
- PtNPs (8-10 nm) were synthesized using a chemical reduction method for the non-enzymatic detection of Uric Acid. A colorimetric portable setup has been developed for remote UA measurements using a smartphone-based application to demonstrate its use in point of care testing. The developed method provided a wide linear response from 1 to 8 mM for UA samples and the results indicated the down-regulating activity of PtNPs. The calculated LOD of $4.2 \pm 5 \mu\text{M}$ was achieved and showed a linear response to 7 mM in color observation. This sensor is potentially applicable to the quantitative detection of UA.
- UCNPs were first used as a fluorescent tag to develop a lateral flow biosensor for ultrasensitive and quantitative detection of Vaspin (pre-diagnosis biomarker for type-2 diabetes). Under the optimum conditions, this LFSA was capable of detecting Vaspin a minimum of 39 pgml^{-1} and has been shown a wide liner range in both buffers ($0.2 - 0.55 \text{ ng ml}^{-1}$) and serum ($0.2, 5, \text{ and } 7 \text{ ngml}^{-1}$) samples.
- A fluorescence-based novel lab-on-chip device is designed, developed, and fabricated for the online monitoring of ROS in breast cancer cells (MCF-7). A fluorescent dye 2',7'-dichlorofluorescein diacetate (DCFDA, 50 μM) was used and obtain a profile of ROS generation for 1 day. This microfluidic chip provides an in-vitro platform for the assessment of cell cycle progression and evaluation of the variety of drugs.
- The future target is to develop highly sensitive, cost-effective, and miniaturized biosensors based devices for point-of-care applications, which required minimum pretreatment steps for sample analysis. Additionally, organ on a chip is an advanced

technology, which requires high through investigation for biomarkers detection, so the integration of electrochemical sensors (immunosensors and enzymatic) would be integrated for the detection of various biomarkers analysis and quantification. To consider the intense fluorescence of UCNPs, further work will aim to develop a multiplex sensor for multiple analytes in the same sample using different colored UCNPs.

Declaration

I (Muhsin Ali), hereby is declaring that this thesis entitled “**Synthesis, Characterizations, and Implementation of Functional Nanostructured Materials and Composites for Point-Of-Care Testing Devices**”, is submitted to Jeju National University in the partial fulfillment of the requirements for the award of the **Degree of Doctor of Philosophy** in the department **of Mechatronics Engineering** is a record of original and independent research work done and published by during the period March 2017 to February 2021 under the supervision of the **Professor Kyung Hyung Choi**. This thesis work is based on the publications in reputed journals and it has not been formed for the award of any other Degree/Diploma/Associateship/Fellowship to any individual of any university.

Muhsin Ali

References

1. S. Hulka, *Biological markers in epidemiology*, 3-15 (1990).
2. S. Naylor. Taylor & Francis, 2003.
3. B. S. Hulka and T. Wilcosky, *Archives of Environmental Health: An International Journal*, **43** (2), 83-89 (1988).
4. O. Golubnitschaja and J. Flammer, *Survey of ophthalmology*, **52** (6), S155-S161 (2007).
5. J. Jeevanandam, A. Barhoum, Y. S. Chan, A. Dufresne, and M. K. Danquah, *Beilstein journal of nanotechnology*, **9** (1), 1050-1074 (2018).
6. C. Jianrong, M. Yuqing, H. Nongyue, W. Xiaohua, and L. Sijiao, *Biotechnology advances*, **22** (7), 505-518 (2004).
7. V. Pokropivny and V. Skorokhod, *Materials Science and Engineering: C*, **27** (5-8), 990-993 (2007).
8. A. P. Turner, *Chemical Society Reviews*, **42** (8), 3184-3196 (2013).
9. M. Holzinger, A. Le Goff, and S. Cosnier, *Frontiers in chemistry*, **2** 63 (2014).
10. A. Valizadeh, H. Mikaeili, M. Samiei, S. M. Farkhani, N. Zarghami, A. Akbarzadeh, and S. Davaran, *Nanoscale research letters*, **7** (1), 480 (2012).
11. M. Bruchez, M. Moronne, P. Gin, S. Weiss, and A. P. Alivisatos, *science*, **281** (5385), 2013-2016 (1998).
12. M. Ali, I. Shah, S. W. Kim, M. Sajid, J. H. Lim, and K. H. Choi, *Sensors and Actuators A: Physical*, **283** 282-290 (2018).
13. F. Ma, C.-c. Li, and C.-y. Zhang, *Journal of Materials Chemistry B*, **6** (39), 6173-6190 (2018).
14. Y. Li, F. Qian, J. Xiang, and C. M. Lieber, *Materials today*, **9** (10), 18-27 (2006).
15. Y.-Z. Long, M. Yu, B. Sun, C.-Z. Gu, and Z. Fan, *Chemical Society Reviews*, **41** (12), 4560-4580 (2012).
16. M. Sireesha, V. Jagadeesh Babu, A. S. Kranthi Kiran, and S. Ramakrishna, *Nanocomposites*, **4** (2), 36-57 (2018).
17. P. Ajayan, T. Ebbesen, T. Ichihashi, S. Iijima, K. Tanigaki, and H. Hiura, *Nature*, **362** (6420), 522-525 (1993).
18. J. Haccoun, B. Piro, V. Noel, and M. Pham, *Bioelectrochemistry*, **68** (2), 218-226 (2006).
19. L. Yu, C. Shearer, and J. Shapter, *Chemical reviews*, **116** (22), 13413-13453 (2016).
20. R. J. Chen, H. C. Choi, S. Bangsaruntip, E. Yenilmez, X. Tang, Q. Wang, Y.-L. Chang, and H. Dai, *Journal of the American Chemical Society*, **126** (5), 1563-1568 (2004).
21. P. Mehrotra, *Journal of oral biology and craniofacial research*, **6** (2), 153-159 (2016).
22. S. B. Nimse, M. D. Sonawane, K.-S. Song, and T. Kim, *Analyst*, **141** (3), 740-755 (2016).
23. D. R. Thevenot, K. Toth, R. A. Durst, and G. S. Wilson, *Pure and applied chemistry*, **71** (12), 2333-2348 (1999).
24. D. R. Thévenot, K. Toth, R. A. Durst, and G. S. Wilson, *Biosensors and bioelectronics*, **16** (1-2), 121-131 (2001).
25. L. C. Clark Jr and C. Lyons, *Annals of the New York Academy of sciences*, **102** (1), 29-45 (1962).
26. P. T. Kissinger, *Biosensors and Bioelectronics*, **20** (12), 2512-2516 (2005).
27. B. H. Huynh, B. A. Fogarty, R. S. Martin, and S. M. Lunte, *Analytical chemistry*, **76** (21), 6440-6447 (2004).
28. A. N. Sekretaryova, M. Eriksson, and A. P. Turner, *Biotechnology Advances*, **34** (3), 177-197 (2016).
29. D. Grieshaber, R. MacKenzie, J. Vörös, and E. Reimhult, *Sensors*, **8** (3), 1400-1458 (2008).
30. B. Srinivasan and S. Tung, *Journal of laboratory automation*, **20** (4), 365-389 (2015).
31. A. Dhiman, P. Kalra, V. Bansal, J. G. Bruno, and T. K. Sharma, *Sensors and Actuators B: Chemical*, **246** 535-553 (2017).

32. J. Sun, Y. Li, F. Pi, J. Ji, Y. Zhang, and X. Sun, *Analytical and bioanalytical chemistry*, **409** (8), 2213-2220 (2017).
33. D. Liu, J. Wang, L. Wu, Y. Huang, Y. Zhang, M. Zhu, Y. Wang, Z. Zhu, and C. Yang, *TrAC Trends in Analytical Chemistry*, **122** 115701 (2020).
34. D. Xu, X. Huang, J. Guo, and X. Ma, *Biosensors and Bioelectronics*, **110** 78-88 (2018).
35. M. Ali, M. A. U. Khalid, I. Shah, S. W. Kim, Y. S. Kim, J. H. Lim, and K. H. Choi, *New Journal of Chemistry*, **43** (20), 7636-7645 (2019).
36. N. Xia and L. Zhang, *Materials*, **7** (7), 5366-5384 (2014).
37. R. Ahmad, N. Tripathy, M.-S. Ahn, K. S. Bhat, T. Mahmoudi, Y. Wang, J.-Y. Yoo, D.-W. Kwon, H.-Y. Yang, and Y.-B. Hahn, *Scientific reports*, **7** (1), 1-10 (2017).
38. T. Hou, W. Li, X. Liu, and F. Li, *Analytical chemistry*, **87** (22), 11368-11374 (2015).
39. P. Miao, B. Wang, Z. Yu, J. Zhao, and Y. Tang, *Biosensors and Bioelectronics*, **63** 365-370 (2015).
40. W. Li, T. Hou, M. Wu, and F. Li, *Talanta*, **148** 116-121 (2016).
41. S. Ameen, M. S. Akhtar, and H. S. Shin, *Chemical engineering journal*, **195** 307-313 (2012).
42. A. Sivapunniam, N. Wiromrat, M. T. Z. Myint, and J. Dutta, *Sensors and Actuators B: Chemical*, **157** (1), 232-239 (2011).
43. S. M. U. Ali, N. Alvi, Z. Ibupoto, O. Nur, M. Willander, and B. Danielsson, *Sensors and Actuators B: Chemical*, **152** (2), 241-247 (2011).
44. R. Ahmad, N. Tripathy, N. K. Jang, G. Khang, and Y.-B. Hahn, *Sensors and Actuators B: Chemical*, **206** 146-151 (2015).
45. S. Ameen, M. S. Akhtar, H.-K. Seo, and H. S. Shin, *Materials Letters*, **136** 379-383 (2014).
46. S. M. U. Ali, O. Nur, M. Willander, and B. Danielsson, *Sensors and Actuators B: Chemical*, **145** (2), 869-874 (2010).
47. A. Sharma, G. Sumana, S. Sapra, and B. D. Malhotra, *Langmuir*, **29** (27), 8753-8762 (2013).
48. A. Roshini, S. Jagadeesan, Y.-J. Cho, J.-H. Lim, and K. H. Choi, *Materials Science and Engineering: C*, **81** 551-560 (2017).
49. M. Guo, P. Diao, X. Wang, and S. Cai, *Journal of Solid State Chemistry*, **178** (10), 3210-3215 (2005).
50. E. S. Forzani, H. Zhang, L. A. Nagahara, I. Amlani, R. Tsui, and N. Tao, *Nano Letters*, **4** (9), 1785-1788 (2004).
51. F. Zhang, X. Wang, S. Ai, Z. Sun, Q. Wan, Z. Zhu, Y. Xian, L. Jin, and K. Yamamoto, *Analytica Chimica Acta*, **519** (2), 155-160 (2004).
52. A. Numnuam, P. Thavarungkul, and P. Kanatharana, *Analytical and bioanalytical chemistry*, **406** (15), 3763-3772 (2014).
53. S. M. U. Ali, Z. H. Ibupoto, M. Kashif, U. Hashim, and M. Willander, *Sensors*, **12** (3), 2787-2797 (2012).
54. Y. Zhao, X. Yan, Z. Kang, P. Lin, X. Fang, Y. Lei, S. Ma, and Y. Zhang, *Microchimica Acta*, **180** (9-10), 759-766 (2013).
55. K. Jindal, M. Tomar, and V. Gupta, *Analyst*, **138** (15), 4353-4362 (2013).
56. T.-Q. Xu, Q.-L. Zhang, J.-N. Zheng, Z.-Y. Lv, J. Wei, A.-J. Wang, and J.-J. Feng, *Electrochimica Acta*, **115** 109-115 (2014).
57. V. M. A. Mohanan, A. K. Kunnummal, and V. M. N. Biju, *Journal of Materials Science*, 1-13.
58. W. Zheng, M. Zhao, W. Liu, S. Yu, L. Niu, G. Li, H. Li, and W. Liu, *Journal of Electroanalytical Chemistry*, **813** 75-82 (2018).
59. Z. Yang, Y. Cao, J. Li, Z. Jian, Y. Zhang, and X. Hu, *Analytica chimica acta*, **871** 35-42 (2015).
60. G. J. Kost and M. McQueen, *Critical reviews in clinical laboratory sciences*, **30** (2), 153-202 (1993).
61. O. A. Loaiza, P. J. Lamas-Ardisana, L. Añorga, E. Jubete, V. Ruiz, M. Borghei, G. Cabañero, and H. J. Grande, *Bioelectrochemistry*, **101** 58-65 (2015).
62. T.-H. Han, Y. Lee, M.-R. Choi, S.-H. Woo, S.-H. Bae, B. H. Hong, J.-H. Ahn, and T.-W. Lee, *Nature Photonics*, **6** (2), 105-110 (2012).

63. Z. Wang and Z. Dai, *Nanoscale*, **7** (15), 6420-6431 (2015).
64. B. Thirumalraj, S. Kubendhiran, S.-M. Chen, and K.-Y. Lin, *Journal of colloid and interface science*, **498** 144-152 (2017).
65. B.-Y. Wu, S.-H. Hou, F. Yin, Z.-X. Zhao, Y.-Y. Wang, X.-S. Wang, and Q. Chen, *Biosensors and Bioelectronics*, **22** (12), 2854-2860 (2007).
66. Z. Li, Z. Wu, and K. Li, *Analytical biochemistry*, **387** (2), 267-270 (2009).
67. Q. Mu, W. Liu, Y. Xing, H. Zhou, Z. Li, Y. Zhang, L. Ji, F. Wang, Z. Si, and B. Zhang, *The journal of physical chemistry C*, **112** (9), 3300-3307 (2008).
68. I. Cruz-Cruz, M. Reyes-Reyes, M. A. Aguilar-Frutis, A. Rodriguez, and R. López-Sandoval, *Synthetic Metals*, **160** (13-14), 1501-1506 (2010).
69. C. Sriprachubwong, C. Karuwan, A. Wisitsorrat, D. Phokharatkul, T. Lomas, P. Sritongkham, and A. Tuantranont, *Journal of Materials Chemistry*, **22** (12), 5478-5485 (2012).
70. G. Dijk, A. L. Rutz, and G. G. Malliaras, *Advanced Materials Technologies*, **5** (3), 1900662 (2020).
71. J. Ouyang, *ACTA PHYSICOCHEMICA SINICA*, **34** (11), 1211-1220 (2018).
72. M. N. Gueye, A. Carella, J. Faure-Vincent, R. Demadrille, and J.-P. Simonato, *Progress in Materials Science*, **108** 100616 (2020).
73. J. Liu, M. Agarwal, and K. Varahramyan, *Sensors and Actuators B: Chemical*, **135** (1), 195-199 (2008).
74. I. Cesarino, F. C. Moraes, M. R. Lanza, and S. A. Machado, *Food Chemistry*, **135** (3), 873-879 (2012).
75. M. Lin, H. Huang, Y. Liu, C. Liang, S. Fei, X. Chen, and C. Ni, *Nanotechnology*, **24** (6), 065501 (2013).
76. L. Malard, M. A. Pimenta, G. Dresselhaus, and M. Dresselhaus, *Physics reports*, **473** (5-6), 51-87 (2009).
77. S. Garreau, G. Louarn, J. Buisson, G. Froyer, and S. Lefrant, *Macromolecules*, **32** (20), 6807-6812 (1999).
78. H. Cunha-Silva and M. J. Arcos-Martinez, *Talanta*, **188** 779-787 (2018).
79. S. Pérez and E. Fàbregas, *Analyst*, **137** (16), 3854-3861 (2012).
80. J. Kim, G. Valdés-Ramírez, A. J. Bandonkar, W. Jia, A. G. Martinez, J. Ramírez, P. Mercier, and J. Wang, *Analyst*, **139** (7), 1632-1636 (2014).
81. B. Haghighi and S. Bozorgzadeh, *Talanta*, **85** (4), 2189-2193 (2011).
82. R. Garjonyte, Y. Yigzaw, R. Meskys, A. Malinauskas, and L. Gorton, *Sensors and Actuators B: Chemical*, **79** (1), 33-38 (2001).
83. W. Shi, X. Luo, and Y. Cui, *Sensors*, **18** (5), 1620 (2018).
84. A. M. Parra-Alfambra, E. Casero, L. Vázquez, C. Quintana, M. del Pozo, and M. D. Petit-Domínguez, *Sensors and Actuators B: Chemical*, **274** 310-317 (2018).
85. M. R. Romero, D. Peralta, C. I. A. Igarzabal, A. M. Baruzzi, M. C. Strumia, and F. Garay, *Sensors and Actuators B: Chemical*, **244** 577-584 (2017).
86. P. J. Lamas-Ardisana, O. A. Loaiza, L. Añorga, E. Jubete, M. Borghei, V. Ruiz, E. Ochoteco, G. Cabañero, and H. J. Grande, *Biosensors and Bioelectronics*, **56** 345-351 (2014).
87. A. Salek-Maghsoudi, F. Vakhshiteh, R. Torabi, S. Hassani, M. R. Ganjali, P. Norouzi, M. Hosseini, and M. Abdollahi, *Biosensors and Bioelectronics*, **99** 122-135 (2018).
88. K. Kempf, B. Rose, T. Illig, W. Rathmann, K. Strassburger, B. Thorand, C. Meisinger, H.-E. Wichmann, C. Herder, and C. Vollmert, *Experimental and clinical endocrinology & diabetes*, **118** (03), 184-189 (2010).
89. H. O. El-Mesallamy, D. H. Kassem, E. El-Demerdash, and A. I. Amin, *Metabolism*, **60** (1), 63-70 (2011).
90. F. Hao, H. Zhang, J. Zhu, H. Kuang, Q. Yu, M. Bai, and J. Mu, *Diabetes Research and Clinical Practice*, **113** 26-32 (2016).
91. R. Feng, Y. Li, C. Wang, C. Luo, L. Liu, F. Chuo, Q. Li, and C. Sun, *Diabetes research and clinical practice*, **106** (1), 88-94 (2014).

92. Y. Na, W. Sheng, M. Yuan, L. Li, B. Liu, Y. Zhang, and S. Wang, *Microchimica Acta*, **177** (1-2), 177-184 (2012).
93. X. Wang, K. Li, D. Shi, N. Xiong, X. Jin, J. Yi, and D. Bi, *Journal of agricultural and food chemistry*, **55** (6), 2072-2078 (2007).
94. C. I. Justino, A. C. Freitas, R. Pereira, A. C. Duarte, and T. A. R. Santos, *TrAC Trends in Analytical Chemistry*, **68** 2-17 (2015).
95. B. Gorovits, S. C. Alley, S. Bilic, B. Booth, S. Kaur, P. Oldfield, S. Purushothama, C. Rao, S. Shord, and P. Siguenza, *Bioanalysis*, **5** (9), 997-1006 (2013).
96. L. Mao, Y. Liu, S. Yang, Y. Li, X. Zhang, and Y. Wei, *Dyes and Pigments*, **162** 611-623 (2019).
97. X. Zhang, K. Wang, M. Liu, X. Zhang, L. Tao, Y. Chen, and Y. Wei, *Nanoscale*, **7** (27), 11486-11508 (2015).
98. Q.-y. Cao, R. Jiang, M. Liu, Q. Wan, D. Xu, J. Tian, H. Huang, Y. Wen, X. Zhang, and Y. Wei, *Materials Science and Engineering: C*, **80** 578-583 (2017).
99. R. Jiang, H. Liu, M. Liu, J. Tian, Q. Huang, H. Huang, Y. Wen, Q.-y. Cao, X. Zhang, and Y. Wei, *Materials Science and Engineering: C*, **81** 416-421 (2017).
100. J. Chen, M. Liu, Q. Huang, L. Huang, H. Huang, F. Deng, Y. Wen, J. Tian, X. Zhang, and Y. Wei, *Chemical Engineering Journal*, **337** 82-90 (2018).
101. U. D. Kamaci, M. Kamaci, and A. Peksel, *Spectrochimica Acta Part A: Molecular and Biomolecular Spectroscopy*, **212** 232-239 (2019).
102. Y. Lan, G. Qin, Y. Wei, C. Dong, and L. Wang, *Spectrochimica Acta Part A: Molecular and Biomolecular Spectroscopy*, **219** 411-418 (2019).
103. X. Song, B. Fu, Y. Lan, Y. Chen, Y. Wei, and C. Dong, *Spectrochimica Acta Part A: Molecular and Biomolecular Spectroscopy*, **204** 301-307 (2018).
104. A. L. Ouellette, J. J. Li, D. E. Cooper, A. J. Ricco, and G. T. Kovacs. ACS Publications, 2009.
105. H. Zhu, F. Lu, X.-C. Wu, and J.-J. Zhu, *Analyst*, **140** (22), 7622-7628 (2015).
106. Y. Zhao, H. Wang, P. Zhang, C. Sun, X. Wang, X. Wang, R. Yang, C. Wang, and L. Zhou, *Scientific reports*, **6** (1), 1-8 (2016).
107. A. Sedlmeier, A. Hlaváček, L. Birner, M. J. Mickert, V. Muhr, T. Hirsch, P. L. Corstjens, H. J. Tanke, T. Soukka, and H. H. Gorris, *Analytical chemistry*, **88** (3), 1835-1841 (2016).
108. J. Lv, S. Zhao, S. Wu, and Z. Wang, *Biosensors and Bioelectronics*, **90** 203-209 (2017).
109. J. Zhou, Z. Liu, and F. Li, *Chemical Society Reviews*, **41** (3), 1323-1349 (2012).
110. H. S. Mader, P. Kele, S. M. Saleh, and O. S. Wolfbeis, *Current opinion in chemical biology*, **14** (5), 582-596 (2010).
111. D. E. Achatz, R. Ali, and O. S. Wolfbeis, in *Luminescence applied in sensor science*, p. 29-50, Springer, (2010).
112. Y. S. Bae, H. Oh, S. G. Rhee, and Y. Do Yoo, *Molecules and cells*, **32** (6), 491-509 (2011).
113. G. Poli, G. Leonarduzzi, F. Biasi, and E. Chiarpotto, *Current medicinal chemistry*, **11** (9), 1163-1182 (2004).
114. L. M. Fan and J.-M. Li, *Journal of pharmacological and toxicological methods*, **70** (1), 40-47 (2014).
115. D. Hernández-García, C. D. Wood, S. Castro-Obregón, and L. Covarrubias, *Free Radical Biology and Medicine*, **49** (2), 130-143 (2010).
116. W. Droge, *Physiological reviews*, **82** (1), 47-95 (2002).
117. P. D. Ray, B.-W. Huang, and Y. Tsuji, *Cellular signalling*, **24** (5), 981-990 (2012).
118. P. Held, *BioTek Instruments Inc., Application Guide*, 1-2 (2012).
119. E. Cadenas and H. Sies, *Free radical research*, **28** (6), 601-609 (1998).
120. M. Valko, C. Rhodes, J. Moncol, M. Izakovic, and M. Mazur, *Chemico-biological interactions*, **160** (1), 1-40 (2006).
121. W. Fiers, R. Beyaert, W. Declercq, and P. Vandenabeele, *Oncogene*, **18** (54), 7719-7730 (1999).
122. N. Pastor, H. Weinstein, E. Jamison, and M. Brenowitz, *Journal of molecular biology*, **304** (1), 55-68 (2000).

123. M. S. Cooke, M. D. Evans, M. Dizdaroglu, and J. Lunec, *The FASEB Journal*, **17** (10), 1195-1214 (2003).
124. M. Valko, D. Leibfritz, J. Moncol, M. T. Cronin, M. Mazur, and J. Telser, *The international journal of biochemistry & cell biology*, **39** (1), 44-84 (2007).
125. M. Klagsbrun and P. A. D'Amore, *Cytokine & growth factor reviews*, **7** (3), 259-270 (1996).
126. G. Neufeld, T. Cohen, S. Gengrinovitch, and Z. Poltorak, *The FASEB journal*, **13** (1), 9-22 (1999).
127. Y. S. Tor, L. S. Yazan, J. B. Foo, N. Armania, Y. K. Cheah, R. Abdullah, M. U. Imam, N. Ismail, and M. Ismail, *BMC complementary and alternative medicine*, **14** (1), 55 (2014).
128. G. Saravanakumar, J. Kim, and W. J. Kim, *Advanced Science*, **4** (1), 1600124 (2017).
129. E. H. Verbon, J. A. Post, and J. Boonstra, *Gene*, **511** (1), 1-6 (2012).
130. C. Nathan and A. Cunningham-Bussel, *Nature Reviews Immunology*, **13** (5), 349-361 (2013).
131. K. K. Griendling, R. M. Touyz, J. L. Zweier, S. Dikalov, W. Chilian, Y.-R. Chen, D. G. Harrison, and A. Bhatnagar, *Circulation research*, **119** (5), e39-e75 (2016).
132. C. Mehanna, C. Baudouin, and F. Brignole-Baudouin, *Toxicology in Vitro*, **25** (5), 1089-1096 (2011).
133. M. Oparka, J. Walczak, D. Malinska, L. M. van Oppen, J. Szczepanowska, W. J. Koopman, and M. R. Wieckowski, *Methods*, **109** 3-11 (2016).
134. Y. Andoh, A. Mizutani, T. Ohashi, S. Kojo, T. Ishii, Y. Adachi, S. Ikehara, and S. Taketani, *Journal of biochemistry*, **140** (4), 483-489 (2006).
135. Y. Gong, B. Yu, W. Yang, and X. Zhang, *Biosensors and Bioelectronics*, **79** 822-828 (2016).
136. X. Chen, Z. Zhong, Z. Xu, L. Chen, and Y. Wang, *Free radical research*, **44** (6), 587-604 (2010).
137. G. Peng, Y. Chen, R. Deng, Q. He, D. Liu, Y. Lu, and J.-M. Lin, *Spectrochimica Acta Part A: Molecular and Biomolecular Spectroscopy*, **204** 1-6 (2018).
138. M. Hao, R. Liu, H. Zhang, Y. Li, and M. Jing, *Spectrochimica Acta Part A: Molecular and Biomolecular Spectroscopy*, **125** 7-11 (2014).
139. Q. Wu, J. Liu, X. Wang, L. Feng, J. Wu, X. Zhu, W. Wen, and X. Gong, *BioMedical Engineering OnLine*, **19** (1), 9 (2020).
140. L. J. Y. Ong, A. Islam, R. DasGupta, N. G. Iyer, H. L. Leo, and Y.-C. Toh, *Biofabrication*, **9** (4), 045005 (2017).
141. J. Y. Park, J. Jang, and H.-W. Kang, *Microelectronic Engineering*, **200** 1-11 (2018).
142. S. N. Bhatia and D. E. Ingber, *Nature biotechnology*, **32** (8), 760-772 (2014).
143. K. Rennert, S. Steinborn, M. Gröger, B. Ungerböck, A.-M. Jank, J. Ehgartner, S. Nietzsche, J. Dinger, M. Kiehntopf, and H. Funke, *Biomaterials*, **71** 119-131 (2015).
144. W. W. Wells and D. P. Xu, *Journal of bioenergetics and biomembranes*, **26** (4), 369-377 (1994).
145. V. M. A. Mohanan, A. K. Kunnummal, and V. M. N. Biju, *Journal of Materials Science*, **53** (15), 10627-10639 (2018).
146. D. Jin, M.-H. Seo, B. T. Huy, Q.-T. Pham, M. L. Conte, D. Thangadurai, and Y.-I. Lee, *Biosensors and Bioelectronics*, **77** 359-365 (2016).
147. N. E. Azmi, N. I. Ramli, J. Abdullah, M. A. A. Hamid, H. Sidek, S. A. Rahman, N. Ariffin, and N. A. Yusof, *Biosensors and Bioelectronics*, **67** 129-133 (2015).
148. M. Hamid, *Food chemistry*, **115** (4), 1177-1186 (2009).
149. R. Gui, H. Jin, H. Guo, and Z. Wang, *Biosensors and Bioelectronics*, **100** 56-70 (2018).
150. A. St John and C. P. Price, *The Clinical Biochemist Reviews*, **35** (3), 155 (2014).
151. W. Zhou, W. Liang, X. Li, Y. Chai, R. Yuan, and Y. Xiang, *Nanoscale*, **7** (19), 9055-9061 (2015).
152. N. R. Nirala, S. Abraham, V. Kumar, A. Bansal, A. Srivastava, and P. S. Saxena, *Sensors and Actuators B: Chemical*, **218** 42-50 (2015).
153. F. Qiao, J. Wang, S. Ai, and L. Li, *Sensors and Actuators B: Chemical*, **216** 418-427 (2015).
154. T. Wang, H. Zhu, J. Zhuo, Z. Zhu, P. Papakonstantinou, G. Lubarsky, J. Lin, and M. Li, *Analytical chemistry*, **85** (21), 10289-10295 (2013).
155. Y. Lin, Z. Li, Z. Chen, J. Ren, and X. Qu, *Biomaterials*, **34** (11), 2600-2610 (2013).
156. Y. Song, K. Qu, C. Zhao, J. Ren, and X. Qu, *Advanced Materials*, **22** (19), 2206-2210 (2010).

157. W. Shi, Q. Wang, Y. Long, Z. Cheng, S. Chen, H. Zheng, and Y. Huang, *Chemical Communications*, **47** (23), 6695-6697 (2011).
158. A. Asati, S. Santra, C. Kaittanis, S. Nath, and J. M. Perez, *Angewandte Chemie*, **121** (13), 2344-2348 (2009).
159. M. Magyar, L. Rinyu, R. Janovics, P. Berki, K. Hernádi, K. Hajdu, T. Szabó, and L. Nagy, *Journal of Nanomaterials*, **2016** (2016).
160. J. Lu, Y. Xiong, C. Liao, and F. Ye, *Analytical Methods*, **7** (23), 9894-9899 (2015).
161. Q. Lu, J. Deng, Y. Hou, H. Wang, H. Li, and Y. Zhang, *Chemical Communications*, **51** (61), 12251-12253 (2015).
162. H.-F. Lu, J.-Y. Li, M.-M. Zhang, D. Wu, and Q.-L. Zhang, *Sensors and Actuators B: Chemical*, **244** 77-83 (2017).
163. D. Zhai, B. Liu, Y. Shi, L. Pan, Y. Wang, W. Li, R. Zhang, and G. Yu, *ACS nano*, **7** (4), 3540-3546 (2013).
164. G.-W. Wu, S.-B. He, H.-P. Peng, H.-H. Deng, A.-L. Liu, X.-H. Lin, X.-H. Xia, and W. Chen, *Analytical chemistry*, **86** (21), 10955-10960 (2014).
165. J.-G. You, Y.-W. Liu, C.-Y. Lu, W.-L. Tseng, and C.-J. Yu, *Biosensors and Bioelectronics*, **92** 442-448 (2017).
166. N. Zhang, C. Han, Y.-J. Xu, J. J. Foley IV, D. Zhang, J. Codrington, S. K. Gray, and Y. Sun, *Nature Photonics*, **10** (7), 473-482 (2016).
167. Q. Liu, Y. Jiang, L. Zhang, X. Zhou, X. Lv, Y. Ding, L. Sun, P. Chen, and H. Yin, *Materials Science and Engineering: C*, **65** 109-115 (2016).
168. E. F. Gabriel, P. T. Garcia, T. M. Cardoso, F. M. Lopes, F. T. Martins, and W. K. Coltro, *Analyst*, **141** (15), 4749-4756 (2016).
169. P. de Tarso Garcia, T. M. G. Cardoso, C. D. Garcia, E. Carrilho, and W. K. T. Coltro, *Rsc Advances*, **4** (71), 37637-37644 (2014).
170. R. K. Bera, A. Anoop, and C. R. Raj, *Chemical Communications*, **47** (41), 11498-11500 (2011).
171. N. E. Azmi, N. I. Ramli, J. Abdullah, M. A. A. Hamid, H. Sidek, S. Abd Rahman, N. Ariffin, and N. A. Yusof, *Biosensors and Bioelectronics*, **67** 129-133 (2015).
172. D. Wu, H.-F. Lu, H. Xie, J. Wu, C.-M. Wang, and Q.-L. Zhang, *Sensors and Actuators B: Chemical*, **221** 1433-1440 (2015).
173. D. Yao, A. G. Vlessidis, and N. P. Evmiridis, *Analytica Chimica Acta*, **478** (1), 23-30 (2003).